# AN ABSTRACT OF THE DISSERTATION OF

Stephanie J. Harrington for the degree of Doctor of Philosophy in Chemical Engineering presented on June 3, 2010.

Title: Experimental and Numerical Analysis of Transport in Saturated Heterogeneous Media

Abstract approved: _____

Brian D. Wood

The conventional advection-dispersion equation cannot adequately describe all processes driving solute transport in heterogeneous systems. This dissertation focuses on the individual influences of both chemical (Chapter 2) and physical processes (Chapters 3 and 4) which affect solute transport. In Chapter 2 we analyzed uranium transport in natural sediment using the chemical multirate mass transfer model available within the STAMMT-L software. This model was used due to many uncertainties of the overall mass transfer influences, which were generalized into a distribution of first-order rate coefficients. Results indicated that the multirate model was adequate for the available experimental data, but the results were not definitive due to incomplete mass recovery information. A second experimental system was constructed in order to provide a well-characterized system for analysis. It consisted of 203 low conductivity ($K_{im}$ = 0.011 cm/min) spherical inclusions within a high conductivity ($K_m$ = 4.66 cm/min) matrix material, creating a highly heterogeneous binary system with a conductivity ratio of 1/424. Three flow rates were used to provide complete mass recovery curves. Results were initially analyzed using a multirate spherical diffusion model available within the STAMMT-L software (Chapter 3). This worked well for the fast and medium flow rate experiments, while its representation of the slow flow rate experiment proved inadequate. An analysis of the time scales for mass transport indicated that the diffusive time through the inclusions was competing with advection through the matrix as the dominant mass transport mechanism. Subsequent modeling was performed by direct numerical simulation using the commercially available STAR-CCM+ software (Chapter 4). Results showed inconsistencies with its ability to adequately describe the system when compared with the multirate model results. This dissertation provides insight into the importance of gathering complete mass recovery data, obtaining detailed measurements to describe the system, as well as analysis of results from multirate solute transport processes in order to obtain an improved understanding of their influences on overall mass transport behavior.

# Experimental and Numerical Analysis of Transport in Saturated Heterogeneous Media

by

Stephanie J. Harrington

A DISSERTATION

submitted to

Oregon State University

in partial fulfillment of
the requirements for the
degree of

Doctor of Philosophy

Presented June 3, 2010
Commencement June 2010

Doctor of Philosophy dissertation of Stephanie J. Harrington presented on June 3, 2010.

APPROVED:

---

Major Professor, representing Chemical Engineering

---

Head of the School of Chemical, Biological & Environmental Engineering

---

Dean of the Graduate School

I understand that my dissertation will become part of the permanent collection of Oregon State University libraries. My signature below authorizes release of my dissertation to any reader upon request.

---

Stephanie J. Harrington, Author

# ACKNOWLEDGEMENTS

I would like to thank Dr. Francisco Jose Valdes Parada (Paco) for assisting me with the technical writing involved with this publication. Dr. Roy Haggerty for his assistance with the interpretation of my experimental results and subsequent analyses using his model, STAMMT-L. I would like to thank my advisor, Dr. Brian Wood, for his technical guidance and allowing me the opportunity to perform and interpret these highly complicated yet interesting transport studies. Dr. Mark Porter's contribution to Chapter 4, with his construction and subsequent simulations run using the CFD software was extremely appreciated. I would also like to thank Charlie Davis for his emotional support and a special thank you to Manfred Dittrich for constructing and troubleshooting key pieces of the laboratory equipment used throughout this research.

# CONTRIBUTION OF AUTHORS

Stephanie Harrington was responsible for all experimental construction and data collection, as well as the majority of the writing for this dissertation. Dr. Brian Wood provided insight for data collection and interpretation, as well as the direct model construction for use with Chapter 4. Dr. Roy Haggerty provided the multirate mass transfer code STAMMT-L, as well as guidance and assistance with the interpretation of subsequent theoretical results in Chapters 2 and 3. Dr. Mark Porter was responsible for the construction and refinement of the direct model simulation results for comparison with the experimental data in Chapter 4.

# TABLE OF CONTENTS

# TABLE OF CONTENTS (Continued)

Page

# LIST OF FIGURES

# LIST OF TABLES

# LIST OF APPENDIX FIGURES

Figure Page

# LIST OF APPENDIX TABLES

# Chapter 1 – Introduction

Experimental and theoretical analyses of solute transport within subsurface environments are important for applications such as irrigation, drinking water supply, contaminant transport, and remediation efforts among others [59, 36, 28, 2, 48]. Solute transport for these applications usually takes place over many characteristic length and time scales. Transport phenomena observed at larger scales are highly related to the structure of smaller-scale transport mechanisms [65]. Therefore both experimental and theoretical representations of solute transport ultimately rely upon averages of the micro-scale processes involved.

Solute transport through porous media is typically described using the basic Advection Dispersion Equation (ADE). This equation, shown in generic form below as Eq.1.1, states that the accumulation of the concentration of a solute is equal to the movement through the pore space in three dimensions due to dispersion ($D$), advection (e.g. velocity, $\vec{v}$), and any gains or losses due to reactions ($R$). The mobile porosity of the system, defined as the volume of pore space divided by the total volume, is described in Eq.1.1 by $\theta_m$, while $\nabla$ represents the grad operator, defined in Eq.1.2 for Cartesian coordinates.

$$\theta_m \frac{\partial c}{\partial t} = \nabla(\theta_m D \nabla c) - \nabla(\theta_m \vec{v} c) + R \tag{1.1}$$

$$\nabla = \frac{\partial}{\partial x} + \frac{\partial}{\partial y} + \frac{\partial}{\partial z} \tag{1.2}$$

Although this equation is general in many ways, it already assumes the dispersion is Fickian in nature. Fickian flux is described by $\vec{J} = -\theta_m D \nabla c$. This implies that the variance, or mean square displacement of molecules, is a linear function of time. This assumption is valid for simple systems, where the dispersion coefficient and flow are constant. As the number of physical and/or chemical processes occurring within the system being studied increase, the assumption of one value for dispersion, pore velocity, and reaction rate, as well as others becomes inadequate for the overall system. This occurs in many environments, including those where there are non-equilibrium solute adsorption-desorption reactions, multiple physical processes occurring due to sediment heterogeneity, as well as others. These types of systems have multiple rates of reaction and/or transport which commonly show up as long tails in solute recovery curves, and are referred to as 'non-Fickian.'

Modeling of multirate solute reaction and transport phenomena has been studied extensively in previous investigations and are of interest due to their non-Fickian late-time behavior [2, 41, 48, 60, 69, 22, 26, 27, 29, 39, 6, 1, 33, 23, 4, 10]. Due to the specialization and time

consuming nature involved with performing detailed experimental studies and/or theoretical developments, the two processes are typically performed independently. When this is done, the assumptions made could lead to an inaccurate interpretation of the results.

Typically, theoretical models are created with necessary assumptions ingrained into their development. This is done to provide a unique solution for a specific type of situation. Similarly, data are collected from experimental studies in order to characterize a specific phenomenon. When a disconnect occurs between experiment and theory, the use of available data or models can lead to inaccurate assumptions and interpreted results. With the wide variety of computer simulation software available, one must choose and/or develop the correct theoretical description of the system being studied. Similarly, the amount of detailed information gathered from experimental research must provide a thorough description of the system and dominant processes occurring throughout the whole study.

This dissertation focuses on two types of multirate experimental systems, chemical and physical. Both systems result in non-Fickian solute transport, which is evident through visual analysis of the late time transport phenomena (i.e. asymmetrical breakthrough curves), as well as the inability of the basic ADE to adequately represent the late-time experimental results. Analysis of these systems are performed using two particular multirate modeling approaches, namely a direct numerical simulation (STAR-CCM+ [©CD-Adapco]) and a multirate model (STAMMT-L [30]).

Direct numerical simulations (DNS) describe processes occurring at the 'Darcy' scale, where the characteristic length is measured in millimeters to tens of centimeters. The basic conservation equations (i.e. conservation of mass, energy, and momentum) can therefore be solved throughout the 'small-scale' physical domain in order to achieve a solution to the 'full-scale' system. For this study, the DNS was performed using the commercially available computational fluid dynamics software STAR-CCM+.

The multirate model, STAMMT-L, is an upscaled version of the 'small-scale' model; it modifies the ADE by incorporating a source/sink term and additional assumptions. This accounts for a variety transport processes involved at the Darcy scale, including chemical, physical, and/or biological processes which may result in an asymmetrical breakthrough curve. This model was used to analyze both experimental systems to determine its applicability to the overall solute transport processes.

The objective of this dissertation was to combine experimental and theoretical analyses of solute transport in sediment. This allowed us to gain a more in-depth understanding of what information was important when conducting this experimental research, as well as what assumptions were appropriate for the construction and/or use of theoretical models. Ultimately, measurements made in natural systems and/or laboratory studies are used to determine long-term reaction and transport characteristics. We therefore investigated the important aspects of

both experimental and theoretical processes.

The first experimental system, described in Chapter 2, analyzed how the transport of uranium was affected by adjustments of the pH and inorganic carbon concentration of a natural sediment. Due to the complex nature of the processes impacting transport and the lack of thorough detailed experimental data, a multirate reaction model was used to investigate the system's transport parameters. In this way, the results of the model were generalized and only provided an indication of how adjustments affected the overall solute transport.

The second experimental system was a synthetic highly heterogeneous environment, consisting of 203 low conductivity (e.g. $K_{im}$ = 0.011 cm/min) sintered sand inclusions within a high conductivity (e.g. $K_m$ = 4.66 cm/min) sand matrix. This provided a convenient system to evaluate the performance of both the DNS and multirate modeling approaches. Detailed information concerning the physical properties and solute transport parameters were measured and calculated during the construction of this system.

The multirate spherical diffusion model (Chapter 3) initially provided insight into the applicability of the more upscaled modeling approach using STAMMT-L. This model was less computationally demanding, requiring assumptions concerning the relevant transport processes within the system. These assumptions were analyzed and found to be inaccurate at the slower flow rates where the diffusive transport time through the inclusions was faster than the advective time through the surrounding matrix. The advective mass transport time through the matrix became smaller than the diffusive flux through the inclusions as the flow rate through the system was increased, leading to the typical diffusive mass transport model becoming an adequate representation for the fast flow rate experiment.

A second numerical method was employed in order to more thoroughly analyze the processes affecting mass transport in this system. The DNS (Chapter 4) was therefore constructed to provide an indication of how well the measured hydrologic parameters reproduced the experimental data. This simulation's only assumption was that the dispersivity and diffusion coefficient should be the same for all three flow rates. Initial results showed poor reproduction for the three flow rates. Adjustments were made to the diffusion coefficient for the inclusions and the dispersivity of the matrix, which improved all model representations. Unfortunately when compared to the model representation from STAMMT-L, the two models did not provide the same results. Therefore, the DNS could not be relied upon to gain any details into what was affecting mass transport for this system.

Due to the changes in dominant mass transport, we conclude that the values for the dispersivity of the matrix and possibly the diffusion coefficient for the inclusions may vary between the three experiments. Further refinements will need to be performed with this representation to determine if improved results can be obtained. Overall conclusions from this research are detailed in Chapter 5.

# Chapter 2 – Effects of Equilibrium pH and Inorganic Carbon on Uranium Transport in Hanford Sediment

S. J. Harrington[a], B. D. Wood[*,a], and R. Haggerty[b]

[a]School of Chemical, Biological, and Environmental Engineering, Oregon State University, 103 Gleeson Hall, Corvallis, Oregon, USA 97331-2702

[b]Department of Geosciences, Oregon State University, 104 Wilkinson Hall, Corvallis, Oregon, USA 97331-5506

Journal of Contaminant Hydrology
11830 Westline Industrial Drive
St. Louis, MO 63146 USA
In Review

## 2.1 Abstract

In this study, we investigate uranium (U) transport in Hanford sediments. Changes in adsorption and residence time were examined as functions of pH and inorganic carbon (IC) concentration. Four experiments were performed in a large column (50 cm long by 5 cm internal diameter) filled with Hanford sediment with a particle size < 4.75 mm. Each of the four experiments had different equilibrium values for the pH and IC pair as follows: #1) pH 8.8 and 11 mM IC; #2) pH 9.1 and 2 mM IC; #3) pH 6.5 and 13 mM IC; and #4) pH 3.3 and 11.5 mM IC. A multirate mass transfer model was used to describe the transport and reaction processes. This paper explores the use of multirate models to adequately represent the experimental data. Both power-law and lognormal distributions for the reaction rate parameters were examined. Overall, both experimental and theoretical results indicated an increased adsorptive capacity for the sediment with decreasing pH and IC concentration.

## 2.2 Introduction

Uranium has been detected in a number of groundwater systems at various Department of Energy facilities, including the Hanford site near the Columbia River in Richland, WA [68]. Uranium subsurface contamination [primarily in the form of U(VI)] has occurred at the Hanford site due to leakage from radioactive storage tanks [61, 62] and inappropriate storage practices. This is a concern due to the site's proximity to the Columbia River and drinking water sources. U(VI) is highly mobile and can result in toxic health effects if consumed [9].

U(VI) has been found to form a variety of aqueous complexes, including uranyl hydroxyl, carbonate, and hydroxy-carbonates, among others [24]. Some chemical species, such as calcium, form complexes (e.g. calcium uranyl carbonate; [37, 24]) that have been shown to increase U solubility. Previous experimental work has suggested that there are at least two categories of surface sites (referred to as *strong* and *weak*) which are major contributors to the adsorption of aqueous U species [46, 7, 19, 58]. Minerals that have been found to react with U species include iron oxy-hydroxides, silicates [54, 58, 63], calcite [38, 58, 64], aluminates [54], and others [54, 31]. These findings indicate that multiple sediment-mediated reactions contribute to U subsurface transport, and total adsorption may depend upon the chemistry of both aqueous and solid phases.

A number of chemical kinetic and transport models have been proposed for describing the U(VI) sorption process which occur during subsurface transport [35, 60, 2, 48, 69, 41, 67]. Where multiple sediment reactions occur, approaches have included a fractional-order kinetic model [2]; a two-site model [60]; a distributed-rate-coefficient model [48, 41]; and a deterministic geochemical model, which included a mechanistic description of both equilibrium and kinetic sorption reactions [69]. Few studies have examined the effects of changes to the natural

chemical properties of a sediment on U transport. This may be particularly important near source zones, where sediments are exposed to long-term geochemical perturbations [61, 62].

The objectives of this research are to enhance the understanding of U transport by (1) detailing experimental results showing how adjustments in equilibrium pH and IC affect transport; and (2) modeling these results by incorporating multiple surface-site reactions which may occur from a variety of adsorbing aqueous complexes. Following the terminology of Haggerty et al. (1995) [26], we lump mass transfer and sorption in the immobile phase into a single process, defined throughout this paper simply as mass transfer. The primary purpose of this work is to examine the ability of multirate mass transfer models (lognormal and power-law) to fit experimentally-measured breakthrough curve data. The model fits are compared by assessing how well each model represented the four sets of breakthrough curve data.

This paper is organized as follows: in Section 2.3 we describe how U transport experiments were constructed, run, and analyzed. Section 2.4 outlines the mathematical theory used for modeling. Both experimental and theoretical results are discussed in Section 2.5. Lastly, conclusions are made in Section 2.6 concerning the experimental data, theoretical analyses, and how both may be useful in the field where zones of equilibrium my develop due to significant differences between a U contaminant source and natural subsurface conditions.

## 2.3 Uranium Transport Experiments

### 2.3.1 Sediment Preparation and Column Packing

Hanford sediment was obtained from a quarry containing the Hanford Formation near Pasco, WA. The material consisted of sands and gravels of mixed basaltic and granitic origin. The sediment was classified as having approximately 30% fine gravels, 65% sand, and less than 5% silt and clay (Dr. Jack Istok, Oregon State University, personal communication). Sediments were sieved using a No. 4 USA standard testing sieve (Fisher Scientific Company) to ensure all particles greater than 4.75 mm were removed prior to column packing. Further sediment analyses were not performed for this research.

The stainless steel column used in all studies was 50 cm long with a 5 cm internal diameter (Fig. 2.1). The column was wet packed with the sieved sediment and flushed with Hanford synthetic groundwater (SGW) (Table 2.1; Dr. Jim Szecsody, PNNL, Richland, WA, personal communication) for at least 4 days prior to running experiments to ensure complete saturation and geochemical equilibration of the system. Wet packing consisted of first adding SGW at pH 8.8 with 11 mM IC through the bottom of the column, then slowly adding sediment from the top to just below the fluid level in approximately 2 cm increments. The side of the column was tapped with a rubber mallet after each sediment addition to ensure it was packed tightly

below liquid level and all trapped air was removed. Added volumes of SGW and sediment were measured prior to addition in order to calculate the column's final porosity ($\theta = 0.38$) and bulk density ($\rho_b = 1845$ mg/cm$^3$).

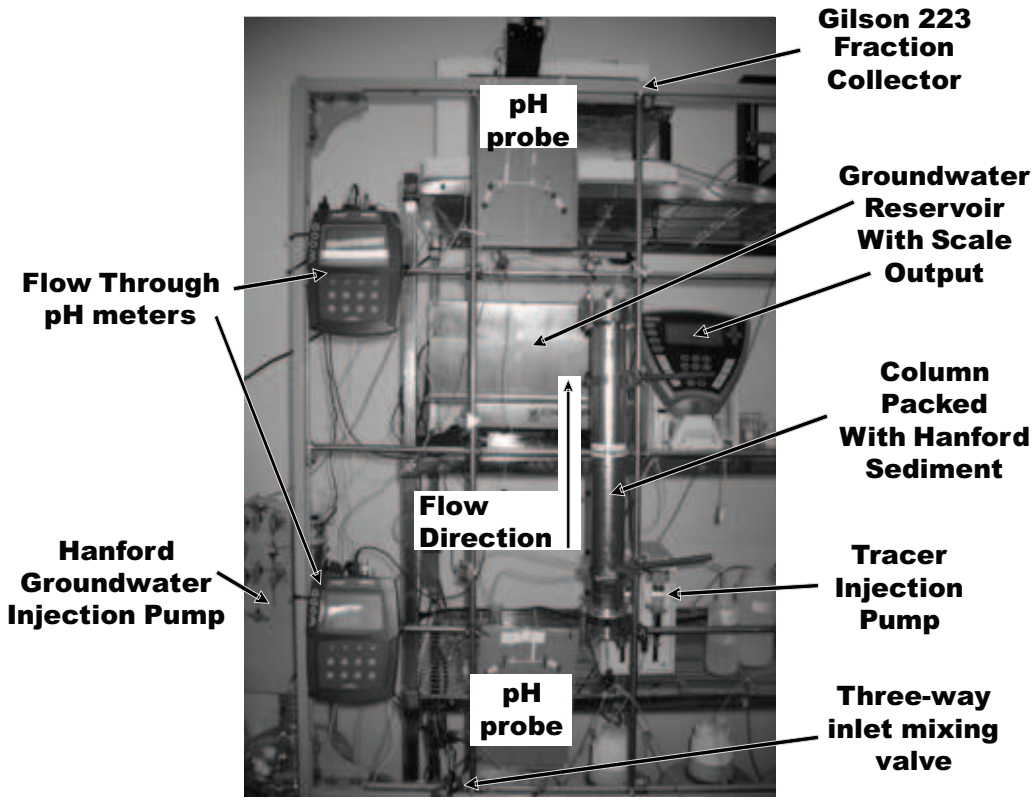


Figure 2.1: Photograph of column used for U transport experiments. Column is 50 cm long with a 5 cm internal diameter.

Table 2.1: Synthetic Hanford groundwater recipe with 1 and 10 mM IC.

| Chemical | mg/L for 1 mM IC | mg/L for 10 mM IC |
|---|---|---|
| NaCl | 15.0 | 15.0 |
| KCl | 8.2 | 8.2 |
| $Na_2SO_4$ | 71.0 | 71.0 |
| $NaHCO_3$ | 84.0 | 841.0 |

### 2.3.2 Transport Experiments

Hanford sediment was equilibrated in the column to the appropriate pH and IC concentration prior to injection of the tracer. This was accomplished by flowing SGW, adjusted to the exper-

imental conditions, through the column until inlet and outlet measurements of pH and IC were nearly identical for at least one pore volume (PV). Adjustments of SGW to appropriate experimental conditions were accomplished using either 1 M $HNO_3$ to decrease or 0.1 M NaOH to increase pH, while IC was adjusted by adding $NaHCO_3$ or sparging with $N_2$ gas. Equilibration was done sequentially; beginning with Experiment #1 (operating conditions are detailed in Table 2.2). Equilibration times for the sediment column took from 4 days (Experiment #1) to 2 months (Experiment #4). To ensure stable IC concentration within the SGW, all SGW solutions were kept in gas-tight tedlar bags (Cole-Parmer, Vernon Hills, IL).

Table 2.2: Measured injection concentrations and average pH and IC for each experiment and ADMT equation fits of $v_x$ and $D$ from $Br^-$ BTC data.

| Experiment # | 1 | 2 | 3 | 4 |
|---|---|---|---|---|
| $c_{0,U}$ (mg/L) | 0.903 | 0.960 | 1.064 | 9.291 |
| total PV for U BTC | 4.4 | 25.2 | 28.6 | 124.6 |
| % recovery U | 100% | 86% | 62% | 93% |
| $c_{0,Br}$ (mg/L) | 23.9 | 23.9 | 22.2 | 305.4 |
| total PV for Br BTC | 3.3 | 3.2 | 2.5 | 4.0 |
| % recovery $Br^-$ | 95% | 100% | 100% | 110% |
| pH | 8.8 | 9.1 | 6.5 | 3.3 |
| IC (mM) | 11.0 | 2.0 | 13.0 | 11.5 |
| fit $v$ (cm/min) | 0.31 | 0.31 | 0.33 | 0.27 |
| fit $D$ ($cm^2$/min) | 0.32 | 0.22 | 0.42 | 0.38 |

Bromide ($Br^-$) was used as an inert tracer for all experiments to ensure ion-exchange was not occurring, as well as for later fitting to determine the system pore water velocity ($v_x$) and dispersion coefficient [$D$; described as $\alpha_{L,m}v_x$ in Eq (2.1)]. The U/$Br^-$ tracer solution was prepared at 10x concentration, and diluted with SGW during injection using a mixing valve. Injection flow rates for the U/$Br^-$ tracer and SGW solutions were 0.25 mL/min and 2.25 mL/min, respectively. At this total flow rate, the travel time for one pore volume (PV) within the column corresponded to 150 minutes. The U/$Br^-$ tracer was injected for a time equal to one PV, after which the U/$Br^-$ tracer pump (402 Syringe Pump, Gilson Inc., Middleton, WI) was stopped and the SGW flow was increased to account for the loss. Outlet samples were collected throughout each experiment in gas-tight sample vials (Kimble Chromatography) using a fraction collector (Gilson Inc., Middleton, WI).

### 2.3.3 Analytical Methods

Total aqueous U species were analyzed using a Kinetic Phosphorescence Analyzer (Chemcheck KPA-11), whereas $Br^-$ was analyzed via Ion Chromatography (Dionex DX-120). In-

organic carbon was analyzed using a high temperature Total Organic Carbon (TOC) Analyzer (Rosemount Analytical Inc., DC-109). This equipment can measure inorganic and/or organic carbon concentrations independently, with the sum of the two measurements resulting in the total carbon within the system. Two Microelectrodes 16-705 Flow-Thru pH electrodes were placed in-line at both the inlet and outlet of the column. These were attached to VWR sympHony SR60IC benchtop pH meters which provided continuous readings throughout each transport experiment. Trace anions were determined periodically in the column effluent using the Ion Chromatograph. Trace cations were measured following experiment #4 using a Varian Liberty 150 Inductively Coupled Plasma-Atomic Emission Spectrometer (ICP).

## 2.4 Mathematical Theory

### 2.4.1 Transport Models

The observed breakthrough curve (BTC) data were analyzed by inverse-fitting the advection-dispersion equation (ADE) and the advection-dispersion-mass-transfer (ADMT) equation using the codes CXTFIT (for $Br^-$ data; [57]) and STAMMT-L (for U data; [30]), respectively. These equations are equivalent when the mass transfer term of the ADMT equation is set to zero. The STAMMT-L code was adopted particularly due to its capability to provide semi-analytic solutions to the ADMT equation(s) as described by Haggerty et al. [26, 27, 29]. This code involves the following assumptions: (1) one-dimensional transport in physically and chemically homogeneous media; (2) steady-state flow conditions; (3) isothermal temperature conditions; (4) rate-limited mass transfer between a single mobile and multiple immobile domains; and (5) linear sorption isotherms. These assumptions were deemed appropriate for our system, with results of batch studies [32] suggesting linear sorption isotherms were appropriate for U transport under our experimental conditions.

Two multirate equations were chosen to represent the U data for comparison; one having a lognormal and the other with a power-law distribution. The lognormal distribution was considered in agreement with previous works [27, 25, 44, 41]. The power-law distribution was considered as an alternative to the lognormal distribution [29]. Both approaches allow for multiple reversible reactive surface sites which follow their respective distribution. This is important since multiple reactive surface site types have been discovered for U, and mineralogical analyses were not performed on our sediment in order to determine which and how many reactive surface site types were potentially available.

### 2.4.2 Mathematical Formulation

The general form of the multirate model employed in STAMMT-L is:

$$\text{ADMT} \qquad \frac{\partial c_m}{\partial t} + \Gamma = \frac{\alpha_{L,m} v_x}{R_m} \frac{\partial^2 c_m}{\partial x^2} - \frac{v_x}{R_m} \frac{\partial c_m}{\partial x} \qquad (2.1)$$

$$\text{for } 0 < x < L$$

$$\text{Source/Sink} \qquad \Gamma = \int_0^\infty \beta_{tot} \frac{\partial c_m(t-\tau)}{\partial t} g^*(\tau) d\tau \qquad (2.2)$$

$$\text{Initial conditions} \qquad c_m|_{t=0} = c_{im}|_{t=0} = 0 \qquad (2.3)$$

$$\text{Upstream B.C.} \qquad c_m|_{x=0} = c_{inj}(t) \qquad (2.4)$$

$$\text{Downstream B.C.} \qquad \left.\frac{\partial c_m}{\partial x}\right|_{x=L} = 0 \qquad (2.5)$$

Eq (2.1) is the basic form of the ADMT equation with a source/sink term ($\Gamma$) for the multirate distribution given in Eq (2.2). In the ADMT, $c_m$ [mass/length$^3$] is the cross sectional area averaged concentration in the aqueous phase; $\alpha_{L,m}$ [length] is the longitudinal dispersivity; $v_x$ [length/time] is the average axial pore water velocity; $t$ [time] is time; $x$ [length] is the space coordinate; and $R_m$ [] is the mobile retardation coefficient. For Eq (2.2), $\beta_{tot}$ [] is the capacity coefficient, defined as:

$$\beta_{tot} = \frac{R_{im}\theta_{im}}{R_m\theta_m} \qquad (2.6)$$

and $g^*(\tau)$ [time$^{-1}$] is the memory function (defined below). The concentration in the immobile phase is denoted by $c_{im}$, as seen in Eq (2.3), and the injected concentration is shown as $c_{inj}$ in Eq (2.4). In Eq (2.6), $\theta_{im}$ [] is the immobile (matrix) porosity, $\theta_m$ [] is the mobile porosity, and $R_{im}$ is the immobile retardation coefficient. The retardation coefficients are defined by the following equations:

$$R_m = 1 + \frac{f\rho_b K_d}{\theta_m} \qquad (2.7)$$

$$R_{im} = 1 + \frac{(1-f)\rho_b K_d}{\theta_{im}} \qquad (2.8)$$

where $f$ [] is the fraction of sorption sites within the mobile domain, $\rho_b$ [mass/lenght$^3$] is the bulk density, and $K_d$ [length$^3$/mass] is the distribution coefficient. $R_m$ is equal to 1 in the absence of sorption or an immobile fraction.

The functional form of the memory function, $g^*(t)$, depends upon the particular mass transfer model being used. This function can be thought of as the probability density of a molecule, having entered the immobile zone at $t = 0$, to remain in the immobile zone at time $t$. The

memory function is related to the distribution of mass transfer rate coefficients by

$$g^*(t) = \int_0^\infty \alpha p(\alpha) \exp[-\alpha t] d\alpha \tag{2.9}$$

where $p(\alpha)$ is the probability density function (pdf) of rate coefficients ($\alpha$ [time$^{-1}$]). Note that $\alpha$ is a function of $t$, and thus all parameters dependent upon $\alpha$ are also functions of $t$. As described by Haggerty et al. (2004) [28], the STAMMT-L multirate model becomes a general formulation of the ADMT equations and encompasses all forms of linear mass transfer through the specification of $g^*(t)$.

Equation (2.1) can be simplified to the conventional advection-dispersion equation (ADE) when there is no source or sink (i.e. $\Gamma = 0$). All experimental $Br^-$ data was fit to the ADE using inverse modeling. The values of $v_x$ were validated by comparison to measured values.

For the U BTC data, both power-law and lognormal distributions of first-order mass transfer rates were compared. The power-law pdf has the form:

$$p(\alpha) = \begin{cases} \frac{(k-2)}{\alpha_{max}^{k-2} - \alpha_{min}^{k-2}} \alpha^{k-3} & \text{for } k > 0, k \neq 2, \alpha_{min} \leq \alpha \leq \alpha_{max} \\ \frac{1}{\ln\left(\frac{\alpha_{max}}{\alpha_{min}}\right)} \alpha^{-1} & \text{for } k = 2 \end{cases} \tag{2.10}$$

where $k$ is the scaling exponent [-], $\alpha_{min}$ is the minimum rate coefficient [time$^{-1}$], and $\alpha_{max}$ is the maximum rate coefficient [time$^{-1}$]. The coefficients $\alpha_{min}$ and $\alpha_{max}$ can be interpreted as representing the reciprocal of the maximum and minimum timescales for mass transfer, respectively. As described by Haggerty et al. (2000) [29], the slope of the late-time BTC is $k$ for $\alpha_{min}^{-1} \ll t \ll \alpha_{max}^{-1}$. The lognormal pdf has the form:

$$p(\alpha) = \frac{1}{\alpha\sigma\sqrt{2\pi}} \exp\left[-\frac{[\ln(\alpha) - \mu]^2}{2\sigma^2}\right] \tag{2.11}$$

For this distribution, $\mu$ and $\sigma$ are the mean and standard deviation of $\ln(\alpha)$, respectively.

To compare the two pdfs, we use the mean residence time in the immobile phase, $t_m$ [time], which is the inverse of the harmonic mean of the pdf [29]. For the lognormal distribution, $t_m = \exp\left(-\mu + \frac{\sigma^2}{2}\right)$, whereas $t_m$ for the power-law pdf depends upon the value of $k$ determined [29]. The most important property of $t_m$ for the power-law distribution is that $t_m \approx \frac{1}{\alpha_{min}}$ for $k < 2$. The corollary to this is that $t_m$ cannot be estimated accurately if $k < 2$ and the BTC data exhibit power-law behavior through the end of the experiment.

## 2.5 Results and Discussion

### 2.5.1 Experimental breakthrough curves

Transport experiments were performed beginning with the highest pH and IC values and sequentially working down to Experiment #4 (Table 2.2). The shape of U BTCs changed significantly as either the pH or IC was adjusted within the system, whereas the $Br^-$ BTCs were nearly identical in all cases. Table 2.2 shows measured injection concentrations and percent recoveries for U and $Br^-$, as well as average pH and IC measurements. Initial concentrations were taken after the injection mixing valve and prior to column inlet. Percent recoveries were determined by dividing the total mass recovered by the total mass injected. The total mass injected was calculated by multiplying the injection concentration by the flow rate and injection time of one pore volume. The total mass recovered was calculated through summation of masses determined through sample measurements over the course of the experiment.

As can be seen in Table 2.2, the injection concentrations for both U and $Br^-$ were an order of magnitude greater for Experiment #4 as compared to the other three experiments. This was due to the lack of any measurable U concentration recovered for this pH and IC pair using U/$Br^-$ concentrations on the same order of magnitude as the other three experiments. Under 10x concentrated conditions, adequate BTC data was obtained and thus used for further analyses.

The $Br^-$ curves were well-fit ($R^2 > 0.95$) using the conventional ADE (Fig. 2.2); the inverse parameterization for $v_x$ and $D$ are shown in Table 2.2. Values of $v_x$ were compared to measured values to ensure accurate model fits, resulting in less than an 8% difference in all cases. These parameters were subsequently used for fitting U BTC data.

The results shown in Table 2.2 indicate that the pore water velocity predicted from the $Br^-$ BTC for Experiment #4 is slightly smaller compared to the other column studies. This is due to an experimental error in which the SGW flow was not increased immediately following the end of the tracer injection. The flow discrepancy was corrected nearly 7.5 hours (3 PV) into the experiment, which occurred after complete recovery of $Br^-$, but before U was measured at the outlet of the column. The calculations for PV were adjusted accordingly due to the reduced flow, providing the most accurate representation of the experimental data for inverse fitting.

The U BTC data for Experiment #1 (Figs. 2.3 and 2.4) did not exhibit obvious tailing. However, when the IC of the system was adjusted from 11 mM (Experiment #1) to 2 mM (Experiment #2), there was substantially more retardation and prominent tailing in the U breakthrough curve. For Experiment #2, complete recovery for U took over six times longer than for Experiment #1. This is consistent with results from other studies [35, 60], which showed that U complexation in the presence dissolved carbonate dramatically affects the surface site reactivity for U.

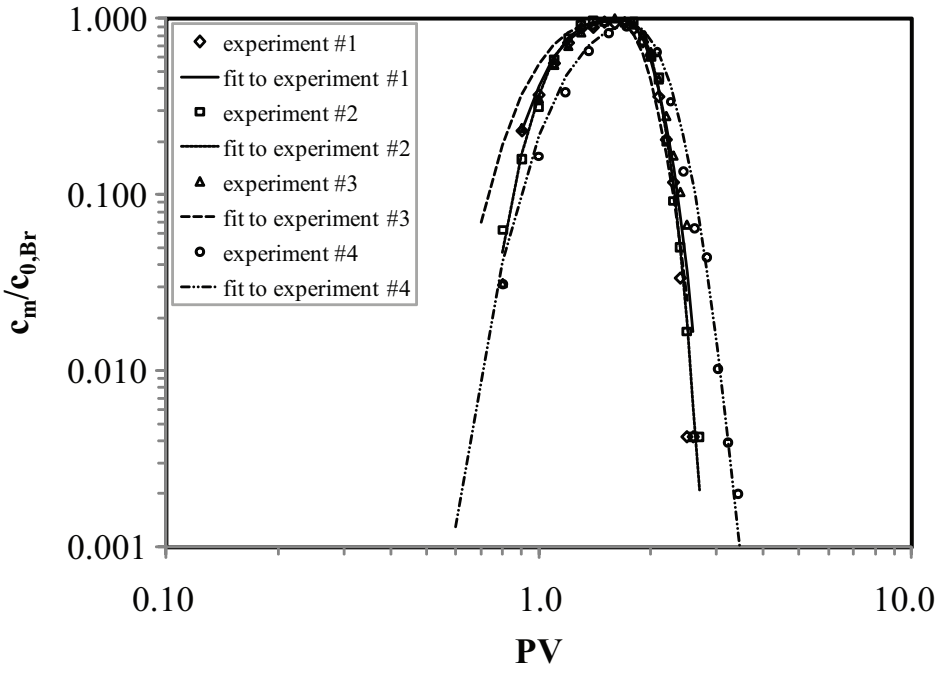


Figure 2.2: $Br^-$ BTC experimental results with fits using the equilibrium ADE.

Experiments #3 and #4 were performed to determine how pH adjustments affected U transport. These were compared to the results from Experiment #1, which was performed with the same IC but higher pH. Breakthrough curve results showed increased retardation and tailing with subsequent reduction in pH as compared to Experiment #1. Mass recovery times increased by nearly an order of magnitude with each subsequent reduction in pH. These results are interesting in that most prior studies [35, 60, 2, 56, 18, 31, 24] have indicated decreased adsorption as the pH is adjusted from neutral to either acidic or alkaline conditions.

Effluent analysis of the column after Experiment #4 showed significant changes in the aqueous geochemical composition as compared to the injected SGW solution (Table 2.3). Metal ions of iron, silica, magnesium, calcium, and aluminum were all measured in notable concentrations in the effluent; these ions were not present at measurable concentrations in the inlet SGW. Similar phenomena were noted by Wan et al. [61, 62], who observed the dissolution of various minerals and cation exchange of sodium with calcium and magnesium in sediment in the highly alkaline (pH $\approx$ 14) and saline tank waste plumes at the Hanford site. These observations suggest that large variations in the pH of our sediment from natural conditions may have resulted in changes to the sediment mineralogical composition. We also see an increased adsorptive capacity of the sediment with decreasing equilibrium pH, which may be due in part to a change in available surface sites through the removal of less-reactive solid mineral phases.

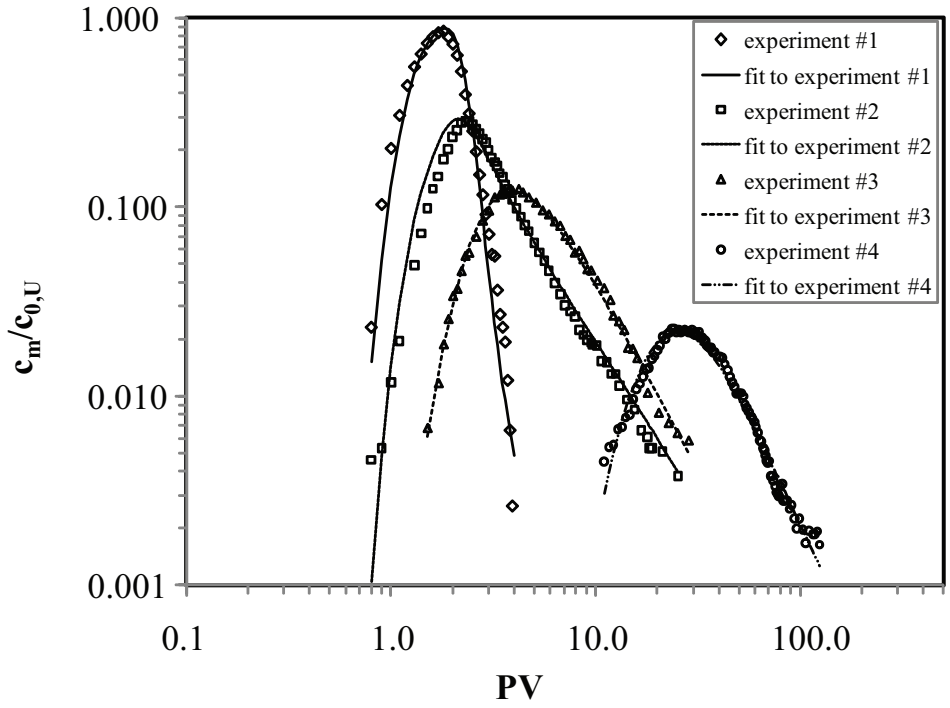


Figure 2.3: U BTC data with fits using the power-law distributed rate ADMT equation.

Further mineralogical analyses are necessary to make any definitive conclusions concerning this hypothesis, but were not performed for this study.

The tailing observed for Experiments #2 through #4 could not be adequately fit using a conventional two-site nonequilibrium equation (Fig. 2.5). The effluent ion analyses suggested that multiple minerals were removed from the system as pH was adjusted, and this would influence the solid-phase reactivity with the variety of U species. Mineralogical analyses were not performed on the sediment used in this study due to a lack of equipment readily available to perform these analyses. Considering the potentially numerous chemical species, complexes, and surface sites within our system, it was not possible to generate a strictly mechanistic model. We therefore adopted a multirate mass transfer model. The advantage of this approach is that it is capable of representing a large number of surface site types interacting with multiple chemical species, and can be of substantial aid in interpreting the bulk behavior of U transport phenomena with changing pH and IC concentration. The disadvantage is that the results are no longer strictly deterministic; rather, they must be viewed as an equation that consolidates the reactions of the various surface sites and aqueous U ions and complexes into a distribution of kinetic rate parameters.

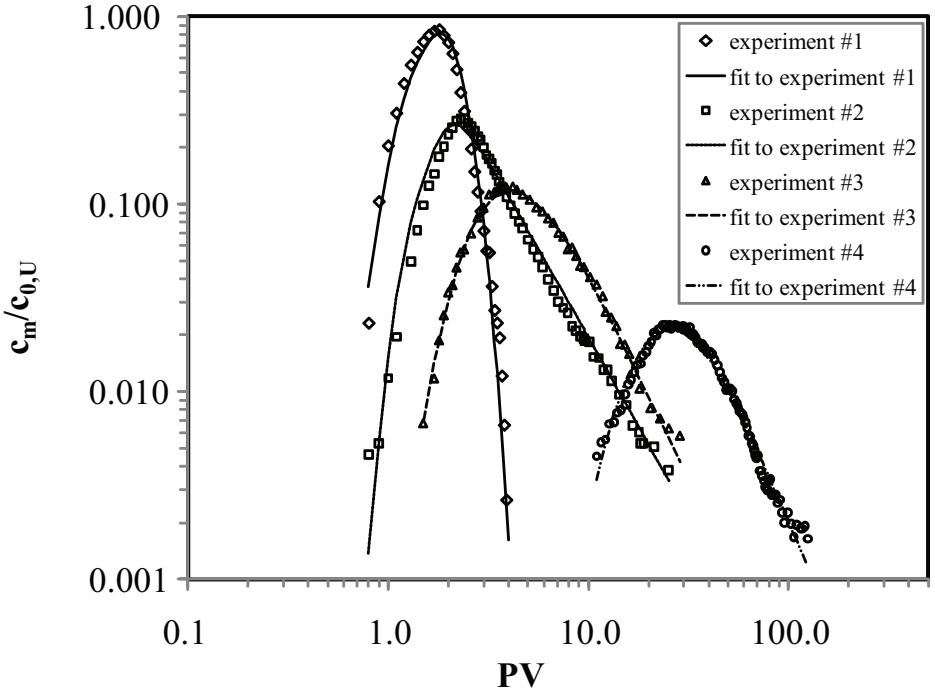


Figure 2.4: U BTC data with fits using the lognormal distributed rate ADMT equation.

### 2.5.2 Theoretical Analyses

Two distributions were used to analyze the mass transfer for the four experiments. Described below are the results from the power-law distribution and the lognormal distribution analyses. These are followed by a comparison between the two distribution results.

#### 2.5.2.1 Power-law distribution

When the power-law pdf was adopted and a best-fit was conducted, the resultant parameterizations exhibited large standard errors. To reduce this error, we included additional information about the system to help constrain parameters. Thus, the values for $\alpha_{min}$ and $\alpha_{max}$ were estimated from experimental BTCs and specified as known values during the fitting process. The maximum timescale for mass transfer ($1/\alpha_{min}$) was set as a range where complete mass recovery would be achieved. These values were estimated from mass recovery (Table 2.2), using the final points of the late-time slope of the corresponding BTC (assuming a linear trend) to estimate complete mass recovery times. The minimum timescale for mass transfer ($1/\alpha_{max}$) was set to a relatively small number of pore volumes (0.001 PV or 0.15 minutes). This left the power-law pdf with only two degrees of freedom; $\beta_{tot}$ and $k$ (as opposed to four when

Table 2.3: Major cation and anion concentrations (mM) from inlet and outlet following experiment #4, measured via ICP and ion chromatography, respectively.

| Major ion | inlet (mM) | outlet (mM) |
|---|---|---|
| $Al^{3+}$ | 0 | 0.13 |
| $Ca^{2+}$ | 0 | 0.11 |
| $Fe^{3+}$ | 0 | 0.14 |
| $K^{+}$ | 0.49 | 0.08 |
| $Mg^{2+}$ | 0 | 0.25 |
| $Mn^{2+}$ | 0 | 0.01 |
| $Na^{+}$ | 11.27 | 4.63 |
| $Si^{4+}$ | 0 | 0.33 |
| $NO_3^-$ | 2.06 | 2.23 |
| $SO_4^{2-}$ | 0.58 | 0.65 |
| $Cl^-$ | 0.20 | 0.22 |

unconstrained).

Fit results (Table 2.4) showed an increasing trend in the immobile capacity coefficient ($\beta_{tot}$) and mean immobile residence time ($t_m$) as either IC or pH was decreased. The maximum timescale for mass transfer in Experiment #1 was small (3.75 h or 1.5 PV), indicating that recovery was fast and that U species spent little time in the immobile zones for this combination of pH and IC. Experiments #2 through #4 showed an increasing trend in immobile capacity and mean immobile residence time, which was consistent with experimental results (Fig. 2.3). The fit values for $k$ showed an initial sharp decrease with decreasing IC or pH; they increased again when the pH was adjusted to 4. This seemingly inconsistent result was most likely due to insufficient tailing data which caused the power-law late time fit to be inaccurate for this simulation.

Table 2.4: Fit parameters using the power-law distributed rate equation.

| Experiment # | 1 | 2 | 3 | 4 |
|---|---|---|---|---|
| pH | 8.8 | 9.1 | 6.5 | 3.3 |
| IC (mM) | 11.0 | 2.0 | 13.0 | 11.5 |
| RMSE | 0.727 | 0.265 | 0.079 | 0.121 |
| $\beta_{tot}$ | 0.276 | 7.057 | 11.56 | 56.89 |
| k | 2.109 | 1.470 | 1.651 | 1.802 |
| $\alpha^*_{min}$ [$h^{-1}$] | 0.267 | 0.008 | 0.008 | 0.001 |
| $\alpha^*_{max}$ [$h^{-1}$] | 400 | 400 | 400 | 400 |
| $t_m$ [h] | 0.375 | 43.4 | 33.1 | 223.2 |

$^*$ : Held Fixed

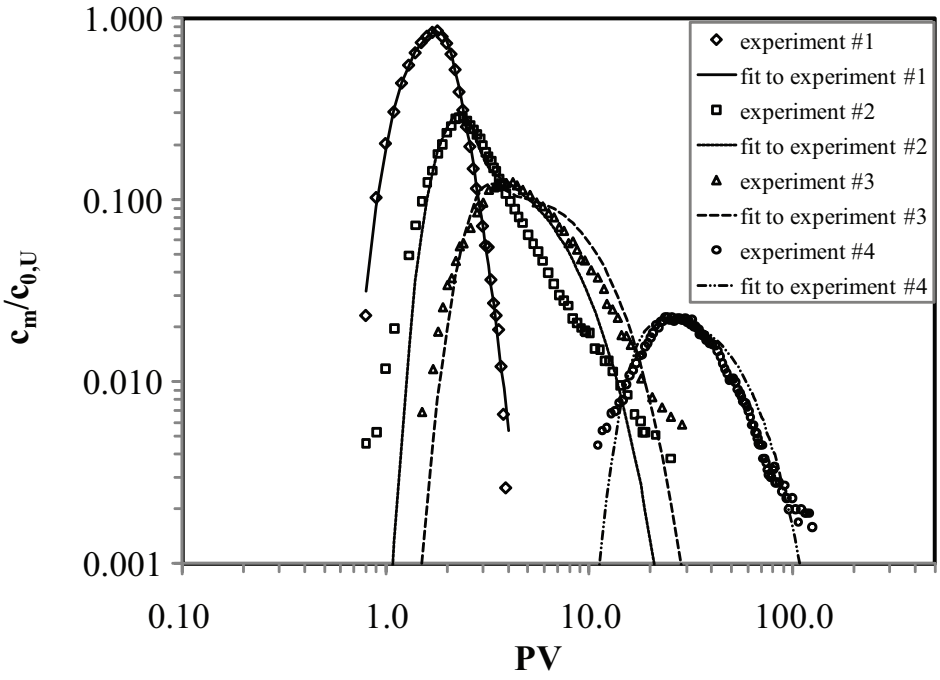


Figure 2.5: U BTC data with fits using the two-site nonequilibrium ADMT equation.

### 2.5.2.2 Lognormal distribution

For the lognormal pdf, the immobile capacity coefficient ($\beta_{tot}$) and standard deviation of the lognormal distribution ($\sigma$) showed an increasing trend as either IC or pH values were decreased (see Table 2.5). This trend was consistent with experimental BTC results. An increased immobile capacity would increase the time for U removal, as well as decrease the maximum concentration of the resulting BTC. The results of Experiment #1 indicated that there was very little sorption under these conditions, and therefore resulting parameters for the system lead to an equation similar to the conventional equilibrium ADMT equation [since $\sigma \approx 0$; [29]].

Table 2.5: Fit parameters using the lognormal distributed rate equation.

| Experiment # | 1 | 2 | 3 | 4 |
|---|---|---|---|---|
| pH | 8.8 | 9.1 | 6.5 | 3.3 |
| IC (mM) | 11.0 | 2.0 | 13.0 | 11.5 |
| RMSE | 0.528 | 0.228 | 0.082 | 0.119 |
| $\beta_{tot}$ | 0.301 | 17.04 | 20.12 | 96.45 |
| $\ln(\mu)$ | 1.33 | -6.25 | -4.88 | -6.69 |
| $\sigma$ | -0.916 | 2.44 | 2.78 | 4.25 |
| $t_m$ [h] | 0.328 | $1.45\text{x}10^5$ | $1.21\text{x}10^5$ | $4.03\text{x}10^8$ |

With the results obtained from the lognormal distribution for Experiment #2, we saw similarities between our fit parameters to those determined by [41]. They analyzed effects of stop-flow events on U desorption from contaminated Hanford sediment columns, adequately fitting their resultant BTC data with a surface complexation-lognormal distributed rate (SC-DR) expression. With a slightly different SGW solution than ours (their pH was 7.85 and total IC was 1 mM), their values for $\ln(\mu)$ and $\sigma$ were $-9.96$ and 2.68, respectively (with a corresponding RMSE of 0.12). In comparison, we saw that our mean rate and RMSE were both slightly larger but our standard deviation was nearly the same. The differences in the parameter values for these two sets of experiments were most likely due to 1) variations between our experimental study and theirs (i.e. SGW, pH, IC, U, their use of surface complexation information, $v_x$, etc.), and 2) incomplete mass recovery data which resulted in inadequate mass transfer distribution parameters.

#### 2.5.2.3 Comparison of distribution results

It can be noted that three out of the four root mean square errors (RMSEs) for the power-law distribution were larger than those for the lognormal distribution. Interestingly, power-law $t_m$ values were orders of magnitude smaller than those of the lognormal pdf. This was due to the time scales for mass transfer for the power-law pdf scaling with $1/\alpha_{min}$. Without complete mass recovery data there was substantial uncertainty about our estimates for $\alpha_{max}$. Complete mass recovery was theoretically not possible while the tail followed a power-law with $k < 2$. Consequently, the estimate of $t_m$ was dependent upon the time-scale of the experiment. One might come to the conclusion that the lognormal distribution was more robust in terms of estimating $t_m$, but this is likely incorrect. The lognormal distribution assumed a distribution shape outside of the timescales supported by the experiment. In fact, at timescales less than the first breakthrough or greater than the last breakthrough, we have little information about the shape of the mass transfer distribution. Consequently, the values of $t_m$ estimated from the lognormal distribution are suspect. It is for these reasons that Haggerty et al. [28] hypothesized that estimates of immobile domain residence time are strongly correlated to experimental timescales.

## 2.6 Conclusions

The results of this research indicate that adjustments in IC or pH made to Hanford sediment have a significant effect on U transport. We found that, as the amount of inorganic carbon within the system was increased from 2 mM (Experiment #2) to 11 mM (Experiment #1), U transport time decreased. We also determined, through comparison of multirate parameter fitting, that the immobile zone capacity ($\beta_{tot}$) decreased significantly with increasing IC con-

centration. This confirms the idea that increasing inorganic carbon concentration will strongly inhibit U adsorption through the reduction of available reactive surface sites, leading to increased U mobility within the subsurface.

Secondly, we observed that as pH was decreased, the characteristic time for U transport increases. To our knowledge, no other work has reported transport studies that have investigated how U transport characteristics change with changes in equilibrium pH. The only available data for comparison were from batch studies [2, 18], which showed decreasing sorption as pH became highly alkaline or acidic. The most important differences between the results from our research and those from batch studies were the equilibration time for pH and IC, and the solid/solution ratios (our studies had a solid/solution ratio that was more than an order of magnitude greater than those reported for batch). These differences provided an increased contact area and residence time for U reaction. Our results therefore provide a more thorough analysis of how adjustments in the equilibrium conditions of Hanford sediment could affect subsurface transport of a step impulse of U at the half-meter scale.

In comparing ion analyses for Hanford sediment with pH adjusted to either a highly alkaline [61, 62] or highly acidic condition (this study), we see that mineral dissolution occurred. This leads to potentially important changes for both ion exchange and adsorption-desorption reactions. In particular, for the apparent changes in the mineralogical composition of the sediment within our system as the pH was reduced (Table 2.3), we propose the increased adsorptive capability may be due to increasing reactive surface sites and/or site types for U.

Lastly, we found that the two multirate mass transfer models used with STAMMT-L showed more adequate fits to the experimental data from this study compared to a two-site nonequilibrium model. We also found some interesting and potentially important trends in how the changes in experimental conditions affected both models' fit parameters. It was apparent that complete mass recovery and tailing information were both important when using either the lognormal or power-law pdf to fit experimental results. If insufficient BTC data is available, the values of fit parameters will only be based upon the data given. The results available for this study may not adequately represent actual late-time occurrences in transport due to long adsorption times and a wide distribution of adsorption rates. Even though the lognormal model did not need any estimations and provided a slightly better fit, we cannot conclude the resulting fits would adequately represent what would have occurred with complete mass recovery.

Results of this study may be useful as an indicator of how the mobility of U contamination is affected in areas where there are drastic changes in subsurface chemistry, such as near tank waste plumes, spills, or mines. As zones of equilibrium are developed over time, one could reasonably predict how the variations in pH and IC within these zones would affect U transport in comparison to natural conditions. Decreases in pH from natural conditions could lead to increasing available surface sites for U adsorption and thus slow transport, whereas increased

IC could increase transport times leading to increased spreading of U contaminant plumes.

## Acknowledgements

This research was supported in part by the National Science Foundation, Collaboration in Mathematical Geosciences (CMG) Program under Grant 0724865-EAR. Data collection was supported by the U.S. Department of Energy through the Natural and Accelerated Biological Remediation (NABIR) program under Grant DE-FG03-02ER63353. Funding for R. Haggerty's contribution to this work was provided by the US Department of Energy's Integrated Field-Scale Subsurface Research Challenge (IRFC) under contract DE-AC05-76RL01830.

# Chapter 3 – Multirate Modeling of a Highly Heterogeneous Experimental System

S. J. Harrington[a] and B. D. Wood[*,a]

[a]School of Chemical, Biological, and Environmental Engineering, Oregon State University, 103 Gleeson Hall, Corvallis, Oregon, USA 97331-2702

Advances in Water Resources
11830 Westline Industrial Drive
St. Louis, MO 63146 USA
To be submitted

## 3.1 Abstract

In this work, we compare experimental observations of solute transport collected from a highly heterogeneous porous medium to predictions from a multirate spherical diffusion model. The experimental system consisted of a high-conductivity matrix with low-conductivity spherical inclusions. Three breakthrough curves were collected at varying flow rates (5.6 ml/min, 9.6 ml/min, and 45.2 ml/min). The breakthrough curve data indicated that there was an increase in the diffusive tailing as the flow rate increased. Forward fits using a spherical diffusion model provided an adequate representation of the breakthrough curve for the case with the highest flow, with a root mean square error of 0.046. For the medium and slow flow rate experiments, the time for advective transport through the matrix began to compete with the diffusive time through the inclusions. This had a large impact on the mass recovery curve and led to a regime where the diffusion model was not adequate. This was validated through inverse fitting of the diffusion coefficient and dispersivity within the model. Further analysis of the time scales for mass transport through the two media showed a strong competition between the mass transfer mechanisms (e.g. advective time within the inclusions, diffusive residence time in the inclusions, and advective time through the matrix). As the advective time through the matrix became longer than the diffusive time through the inclusions, the assumptions made by the spherical diffusion model began to break down resulting in inadequate parameter estimation.

## 3.2 Introduction

Variability in the spatial distribution of hydraulic conductivities within natural sediments has been shown to greatly affect solute transport through porous media. When there is a large (normalized) variance in the log-based hydraulic conductivity, typical Fickian solute transport models have proven to be inadequate for describing the late-time behavior of the resultant experimental data [29, 73, 42]. A number of theories have been developed to describe transport through porous media where there is a high variance in the log-conductivities. These include continuous time random walks [43, 5, 16, 21], fractional derivative formulations [4, 5, 14], and volume averaging [49, 22, 12, 10] to name a few.

The simplest case of a highly heterogeneous environment is a binary spatial conductivity field which consists of two distinct regions; this is a relevant heterogeneity that has been found in natural systems [8, 47, 55]. Previous research has been conducted on 2D conductivity fields [73, 15, 39], where low-conductivity inclusions were placed within a high-conductivity matrix material. Zinn et al. [73] provided results for three studies with varying transport behaviors. These phenomena were related to the contrast in hydraulic conductivities of the system used. With small contrast between the high- and low-conductivity materials ($K_{high}/K_{low} = \kappa = 6$), the transport behavior was adequately fit using the classical advection-dispersion equation (ADE).

As the parameter $\kappa$ was increased to 300, the system showed more advection-dominated tailing properties. Finally, as $\kappa$ was increased to 1800, diffusion became the dominant transport phenomena responsible for the observed tailing behavior.

In this study, we investigate the results of three mass recovery experiments obtained with varying flow rates in a 3-dimensional physically heterogeneous environment. The experimental system had dimensions of 100 cm x 50 cm x 20 cm, and consisted of a high-conductivity matrix material ($K_m$ = 4.66 cm/min) with low-conductivity spherical inclusions ($K_{im}$ = 0.011 cm/min). To construct the medium, 203 low-conductivity spherical inclusions were prepared by sintering 0.07 mm solid glass spheres into a larger spherical shape with a diameter of 5 cm. These were randomly placed within the high-conductivity matrix material (average particle size of 2.4 mm). The inclusions provided 13.3% of the total porous medium volume, with the matrix material providing the remaining 86.7%. The three experiments were performed using average flow rates of 5.6, 9.6, and 45.2 ml/min.

Mass recovery curves were analyzed using a multirate spherical diffusion model available in STAMMT-L [30]. This code assumes one-dimensional transport of a conservative species and that mass transport within the inclusions is purely diffuse, whereas there is advective-dispersive transport within the surrounding matrix. The goal of this study is to provide insight into the applicability of the multirate spherical diffusion model for this experimental system. We accomplish this through (1) comparison between forward and inverse fit parameter estimates with experimental data and measured parameters, and (2) analysis of the dominant solute transport behavior for the three experimental runs.

## 3.3 Material and Methods

Two sizes of Spheriglass solid glass spheres (Potters Industries Inc., Valley Forge, PA) were used to construct the heterogeneous environment within the flowcell (see Figure 3.1). The matrix was a larger A-240 material, whereas a finer 2530 material was used to construct the spherical inclusions through sintering.

### 3.3.1 Matrix material properties

The A-240 Spheriglass solid glass spheres had a particle size range between 2 and 2.8 mm. The bulk density of the material was calculated through water displacement measurements to be 2.5 ±0.1 g/cm$^3$. Hydraulic conductivity was determined through the use of a constant head permeameter as 4.66 ±0.96 cm/min. Calculation of porosity within the flowcell was determined during the wet packing process as the volume of fluid added divided by the volume taken up by the matrix, leading to a value of 0.40 ±0.03. The matrix took up approximately 86.7% of

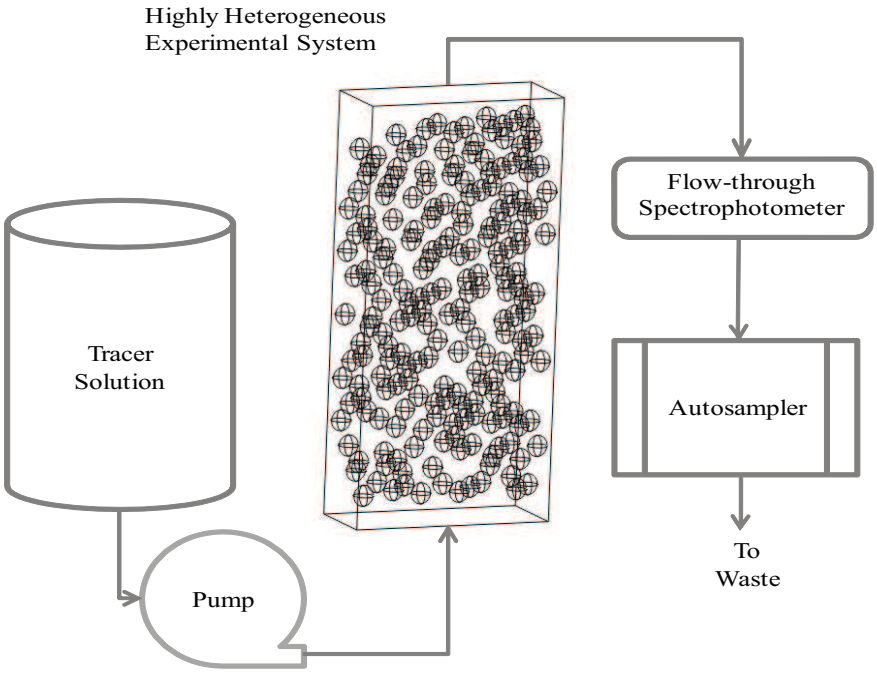


Figure 3.1: Experimental set-up for Highly Heterogeneous System

the total volume within the flowcell.

### 3.3.2 Inclusion construction and hydraulic properties

Spherical inclusions were constructed by sintering the 2530 Spheriglass solid glass spheres using graphite molds of a sphere with an internal diameter of 5 cm. Initially, the 2530 material had an average particle size of 0.07 mm and hydraulic conductivity of 0.0032 cm/min, determined using a falling head permeameter. The graphite molds were filled with the loose material and heated two at a time for 2.5 hours in a muffle furnace at 725°C. The molds were allowed to cool overnight, with the final product being sanded with a fine grain sand paper to remove any loose material and insure a smooth spherical shape. Each inclusion was numbered and weighed to obtain their individual dry weights.

Carbon dioxide ($CO_2$) was used to purge the air from the pore space of the inclusions prior to saturation with a solution of 100 ppm sodium borate in DI water. The $CO_2$ was used to ensure complete saturation since it dissolves more readily in water than air, whereas sodium borate was used as a microbial growth inhibitor. Once saturated, the inclusions were again weighed to determine their individual porosities ($\theta_{im}$; see Table A.1 in the Appendix A.1) using

$$\theta_{im} = \frac{V_{fluid}}{V_{solid} + V_{fluid}} \tag{3.1}$$

Porosity is equal to the difference between the weight of the saturated inclusion and dry inclusion multiplied by the density of water, providing the volume of fluid within the inclusion, divided by the sum of the solid and fluid volumes.

The hydraulic conductivity of each inclusion was calculated using pressure drop measurements. The individual inclusions were placed within a stainless steel column and held in place using c- and 0-rings (see Figure 3.2). These kept the inclusion between two ports on the side of the column, which were used to measure pressure drop across the sphere when fluid was pumped through the horizontally placed column. A constant flow was achieved using a dual syringe pump set to a constant flow rate. The pressure drop measurement was measured in units of centimeters water. In order to calculate hydraulic conductivity, we used Darcy's Law

$$K_{im} = -\frac{Q}{A_{im}} \frac{dh_{im}}{dL} \tag{3.2}$$

In this equation, $K_{im}$ is the hydraulic conductivity of the inclusion [length/time]; $Q$ is the flow rate through the column [length$^3$/time]; $A_{im}$ is the cross-sectional area of the inclusion [length$^2$]; $dh_{im}$ is the pressure drop measured across the inclusion [length]; and $dL$ is the length between the two pressure measurement ports.

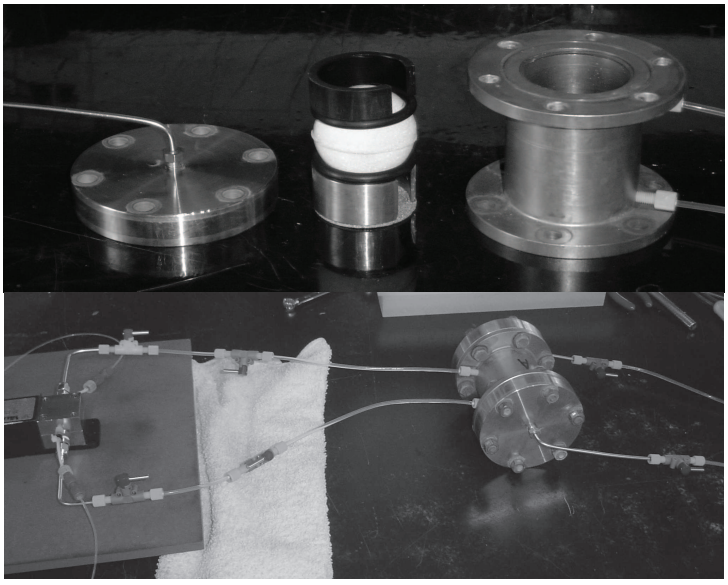

Figure 3.2: Pressure drop equipment for use with inclusion. Top: Internal configuration and stainless steel column used for measuring pressure drop across inclusions. Bottom: Column connected to pressure transducer, with ports in the side of the column being just above and just below the inclusion within.

All measurements were performed in duplicate to ensure accuracy. Once complete, the inclusions were again submerged in a tank full of the 100 ppm sodium borate solution. The

average values for the hydraulic parameters from all 203 inclusions used within the experimental system were an average bulk density of 2.43 ±0.1 g/cm$^3$, hydraulic conductivity of 0.011 ±0.007 cm/min, and porosity of 0.31 ±0.003. Through comparison between the sintered product and the loose material, we note that the sintering process resulted in an over three fold increase for the hydraulic conductivity value, going from 0.0032 cm/min for the 2530 sand to an average of 0.011 cm/min for the sintered inclusions.

### 3.3.3 Tracer solution

The tracer, consisting of 100 ppm sodium borate, 25 mg/L $Br^-$ (from LiBr), and 1.5 mg/L fluorescein at pH 9, was used to provide the three mass recovery curves for this study. The mass recovery curve was shown as the change in concentration from saturation to complete mass recovery of the tracer within the experimental system. The three average flow rates were 5.6 mL/min, 9.6 mL/min, and 45.2 mL/min for Experiments #1, #2, and #3, respectively. Resultant concentration versus time data were collected at the outlet of the system (see Appendix Tables A.2, A.3, and A.4 for Experiments #1, #2, and #3 respectively).

### 3.3.4 Analytical Tools

Fluorescein was measured using a flow-through spectrophotometer with OOIBase 32 software from Ocean Optics for the second experiment. A model 10-AU-005-CE fluorometer from Turner Designs (Sunnyvale, CA) with a flow cell sampler was used for the first and third experiments. Aqueous samples, used to measure $Br^-$ using a Dionex DX-120 ion chromatograph, were taken using a Gilson 223 sample changer.

## 3.4 Transport Model Theory/Calculation

Analyses of the three mass recovery curves were performed using the advection-dispersion-mass-transfer (ADMT) equation available within the STAMMT-L code [30]. The mass-transfer term chosen for this study was diffusion within a spherical geometry. Key assumptions for this model include: (1) one-dimensional dual porosity transport; (2) a purely diffuse immobile zone; (3) steady-state flow conditions; (4) isothermal temperature conditions; and (5) mass transfer between domains is rate limited.

### 3.4.1 Mathematical Formulation for Multirate Model

The general form of the multirate model employed by STAMMT-L is shown in Eqs (3.3) through (3.9) below.

ADMT
$$\frac{\partial c_m}{\partial t} + \Gamma = \frac{\alpha_{L,m} v_x}{R_m} \frac{\partial^2 c_m}{\partial x^2} - \frac{v_x}{R_m} \frac{\partial c_m}{\partial x} \quad \text{for } 0 < x < L \tag{3.3}$$

Sphere Source/Sink
$$\Gamma = \int_0^\infty \beta_{tot} \frac{\partial c_m(t-\tau)}{\partial t} g^*(\tau) d\tau \tag{3.4}$$

Initial Conditions
$$c_m|_{t=0} = c_{im}|_{t=0} = 1 \tag{3.5}$$

Upstream B.C.
$$c_m|_{x=0} = 0 \tag{3.6}$$

Downstream B.C.
$$\left.\frac{\partial c_m}{\partial x}\right|_{x=L} = 0 \tag{3.7}$$

Outer B.C. for Inclusions
$$c_{im}|_{r=0} = c_m \tag{3.8}$$

B.C. for Center of Inclusions
$$\left.\frac{\partial c_{im}}{\partial r}\right|_{r=a} = 0 \tag{3.9}$$

Equation (3.3) is the basic form of ADMT, with the source/sink term ($\Gamma$) for the multirate distribution given by Eq (3.4). In the ADMT equation, $c_m$ [mass/length$^3$] is the cross-sectional area averaged concentration in the matrix; $\alpha_{L,m}$ [length] is the longitudinal mobile dispersivity; $v_x$ [length/time] is the average axial pore water velocity in the mobile phase, as the inclusions are assumed to be purely diffuse; $t$ is time; $x$ [length] is the space coordinate; and $R_m$ [-] is the mobile retardation coefficient. For Eq (3.4), $\beta_{tot}$ [-] is the capacity coefficient, defined as the ratio of immobile domain pore space to mobile domain pore space, and $g^*(\tau)$ $\left[T^{-1}\right]$ is the memory function. The initial concentration in both the matrix and inclusions (e.g. mobile and immobile phase, described by $c_m$ and $c_{im}$) are 1, as seen in Eq (3.5), and the injected concentration at $t = 0$ is zero in Eq (3.6). The downstream boundary condition for the matrix is set to be zero flux [Eq (3.7)]; the outer boundary of the inclusions are assumed to be the same concentration as the surrounding matrix [Eq (3.8)]; and the center boundary of the inclusions is also set to be zero flux [Eq (3.9)].

The functional form of the memory function, $g^*(t)$, is dependent upon the particular mass transport model being used. These functions can be thought of as the probability density of a molecule, having entered the immobile zone at $t = 0$, to be remaining in the immobile zone at time $t$. The memory function is related to the spherical diffusion rate coefficient by Eq (3.10),

where $a$ is the radius of the inclusions [length].

$$g^*(t) = \sum_{j=1}^{\infty} 6\beta_{tot}\frac{D^*_{im}}{a^2}\exp\left[-j^2\pi^2\frac{D^*_{im}}{a^2}t\right] \tag{3.10}$$

As described by Haggerty et al. [28], the STAMMT-L multirate model is a general formulation of ADMT equations and encompasses all forms of linear mass transport through the specification of $g^*(t)$. Therefore, Eq (3.3) can also be simplified to the conventional advection-dispersion equation (ADE) when there is no source or sink (i.e. $\Gamma = 0$).

### 3.4.2 Calculation of Experimental Parameters

In conducting the three mass recovery experiments, a complete set of experimental parameters were determined through various measurements. These included the flow rate ($Q$), cross-sectional area of the experimental system ($A_{xc}$), volume of the matrix and inclusions ($V_m$ and $V_{im}$), size and associated hydrologic parameters for each of the inclusions (radius, $a$; hydraulic conductivity, $K_{im}$; porosity, $\theta_{im}$), and hydrologic characteristics of the matrix material (hydraulic conductivity, $K_m$; porosity, $\theta_m$). These parameters were necessary inputs for the use of the multirate spherical diffusion model.

With the above measured parameters, calculations were done in order to determine the subsequent parameters necessary for the model construction. These included the average axial pore water velocity through the matrix ($v_x$), capacity coefficient ($\beta_{tot}$), mobile and immobile retardation coefficients ($R_m$ and $R_{im}$), longitudinal dynamic dispersivity ($\alpha_{L,m}$), dilution factor (dilute), mobile and immobile decay factors ($\lambda_m$ and $\lambda_{im}$), and the multirate diffusion parameter $\left[\ln(D^*_{im}/a^2)\right]$.

The average pore water velocity within the system was calculated from Eq (3.11).

$$v_x = \frac{Q}{V_m A_{xc}\theta_m} \tag{3.11}$$

In this equation, $Q$ is the measured flow rate [length$^3$/time], $V_m$ is the volume fraction of the matrix material within the system, $A_{xc}$ is the cross-sectional area of the system [length$^2$], and $\theta_m$ is the matrix porosity.

The capacity coefficient ($\beta_{tot}$), which is defined as the ratio of mass in the immobile zone to that in the mobile zone at equilibrium, was assumed to be equivalent to the ratio of the total volume of fluid held within the inclusions to that of the matrix since the solutes used in this study were inert. The total volume of fluid within the matrix was measured to be 34,782.5 ±0.2 mL, while that within the inclusions was 3,799.0 ±0.4 mL. In order to calculate volumes, we used the density of water at 20 °C (0.998 g/mL). This lead to a value of $\beta_{tot} = 0.1092 \pm 0.0001$.

The mobile and immobile retardation coefficients ($R_m$ and $R_{im}$) were assumed to be 1 for all cases. This meant that there was no slowing of the solute relative to the flow of the water through the system.

The value for the longitudinal dispersivity ($\alpha_{L,m}$) was calculated from Eq (3.12).

$$\alpha_{L,m} = \frac{\mathcal{D}_{L,m} - D^*}{v_x} \tag{3.12}$$

Here, $\mathcal{D}_{L,m}$ is the longitudinal dispersion coefficient [length$^2$/time] and $D^*$ is the effective diffusion coefficient [length$^2$/time] which was calculated using the Maxwell's equation

$$D^* = D\left(\frac{2}{3-\theta}\right) \tag{3.13}$$

In Eq (3.13), $D$ is the molecular diffusion coefficient for fluorescein ($2.94x10^{-4}$ cm$^2$/min [51]) and $\theta$ is the porosity of the system being studied. For fluorescein, the value of $\alpha_{L,m}$ for the matrix was calculated based upon breakthrough curves obtained from homogeneous experimental runs that were fit using the basic ADE to determine the value of $\mathcal{D}_{L,m}$ (not shown). This fit provided a value for $\alpha_{L,m} = 0.5232$ cm.

The remaining parameters for the model construction included the dilution factor, mobile and immobile decay factors, and multirate diffusion parameter. The dilution factor was set equal to one, since there was no dilution of the solute or loss of mass. The mobile and immobile decay factors were set equal to zero, since there was no decay of the solute in either the mobile or immobile pore space. Finally, the multirate diffusion parameter, $\left[\ln(D^*_{im}/a^2)\right]$, was calculated to be $-6.132$ hr$^{-1}$ for the inclusions, where $D^*_{im}$ was calculated using Eq (3.13) as $1.3576*10^{-2}$ cm$^2$/hr and $a = 2.5$ cm.

## 3.5 Results and Discussion

Measurements and assumptions from the experimental system provided values for $v_x$, $\beta_{tot}$, $R_m$, $R_{im}$, the dilution factor, and the mobile and immobile decay factors ($\lambda_m$ and $\lambda_{im}$) (see Table 3.1). Homogeneous experiments were run with just the matrix (data not shown) in order to provide the dispersion coefficient [and therefore dispersivity using Eq (3.12)] for fluorescein. The study provided a longitudinal dispersion coefficient for the matrix of $\mathcal{D}_m = 0.0353$ cm$^2$/min ($v_m = 0.067$ cm/min; $\alpha_m = 0.5240$ cm). This value was used as an initial guess for the heterogeneous experiments (see Table 3.1), with the assumption that dispersion was occurring within the matrix, while only diffusion occurred within the inclusions.

Using the values from Table 3.1, forward modeling was performed for all three experiments. Comparison of the model's fit to the experimental data (see Figure 3.3 and Table 3.1)

Table 3.1: Experimental parameters calculated for multirate model

| Experiment # | 1 | 2 | 3 |
|---|---|---|---|
| $v_x$ (cm/hr) | 0.9714 | 1.6626 | 7.8183 |
| PV (hr) | 114.19 | 66.71 | 14.20 |
| $\beta_{tot}$ | 0.1092 | 0.1092 | 0.1092 |
| $R_m$ | 1.0 | 1.0 | 1.0 |
| $R_{im}$ | 1.0 | 1.0 | 1.0 |
| dilute | 1.0 | 1.0 | 1.0 |
| $\lambda_m$ | 0.0 | 0.0 | 0.0 |
| $\lambda_{im}$ | 0.0 | 0.0 | 0.0 |
| $\alpha_{L,m}$ (cm) | 0.5232 | 0.5232 | 0.5232 |
| $ln\left(D^*_{im}/a^2\right)$ ($hr^{-1}$) | −6.132 | −6.132 | −6.132 |
| Forward STAMMT-L Model Fit to Experimental Data | | | |
| RMSE | 0.0964 | 0.0807 | 0.0457 |
| Harmonic Mean | 0.0326 | 0.0326 | 0.0326 |
| Average Standard Error | 0.4955 | 0.6371 | 0.1635 |

indicated that the model representation improved as the flow rate within the system increased. In order to understand this observation, we compared the ratio of the advective to diffusive fluxes in the inclusions ($\mathrm{Pe}_{im}$) to the ratio of the advective flux in the matrix to the diffusive flux in the inclusions ($\mathrm{Pe}_{m/im}$). These are denoted as Péclet numbers, $\mathrm{Pe}_{\omega\omega}$ and $\mathrm{Pe}_{\eta\omega}$ in Golfier et al. [22], or as a Péclet number and a Damköhler number in Zinn et al. [73].

With previously calculated parameters, the Péclet number for the inclusions ($\mathrm{Pe}_{im}$) could be calculated using the following formula:

$$\mathrm{Pe}_{im} = \frac{v_x \kappa}{a} \frac{a^2}{15 D^*_{im}} \tag{3.14}$$

The first term ($v_x\kappa/a$) is the reciprocal of the advective time through an inclusion (i.e. $1/t_{ad,im}$) while the second term ($a^2/15D^*_{im}$) is the diffusive time through an inclusion, $t_\alpha$. The inclusion's average pore water velocity was based upon that within the matrix ($v_x$) multiplied by the ratio of the average hydraulic conductivities of the inclusions to that of the matrix (i.e. $\kappa = K_{im}/K_m = 0.00236$). The diffusive time within the inclusions is equivalent to the inverse of the harmonic mean of the density function for the spherical diffusion model [29, 22, 10].

The second Péclet number, comparing the advective time in the matrix ($L/v_x = t_{ad}$) to the diffusive time within the inclusions, was calculated through the use of the following formula, using the values given in Tables 3.1 and 3.2.

$$\mathrm{Pe}_{m/im} = \frac{v_x}{L} \frac{a^2}{15 D^*_{im}} \tag{3.15}$$

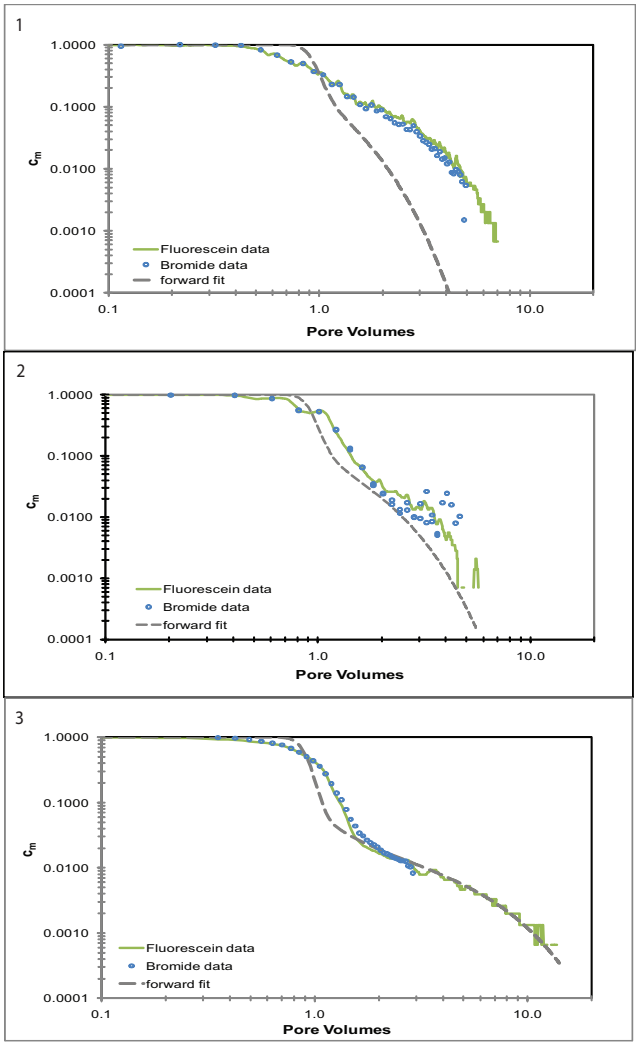


Figure 3.3: Multirate spherical diffusion model comparison using measured parameters

Comparing the two Péclet numbers revealed that increasing the flow rate resulted in a noticeable change of the dominant mass transfer process within the inclusions (see Figure 3.5). The area where the first two experiments fall is a region where both the diffusion in the inclusions and convection in the matrix have similar time scales, whereas the third experiment falls within the regime where the immobile phase is diffusion dominated. We notice that, as the flow rate increased to the 'Mobile-Immobile' regime, the spherical diffusion model more adequately represented the experimental data.

When $\mathrm{Pe}_{im} < 1$, diffusion is dominant within the inclusions, whereas with $\mathrm{Pe}_{m/im} < 1$, advection through the system out-competes the diffusion component of the inclusions, and the resulting transport behavior is close to Fickian. For Experiments #1 and #2, the advective time within the matrix was slower than the diffusive residence time in the inclusions, whereas the

Table 3.2: Transport parameters for two flow regimes

| Experiment # | 1 | 2 | 3 |
|---|---|---|---|
| $v_{im}$ (cm/hr) | 2.292E-03 | 3.924E-03 | 0.01842 |
| $v_x$ (cm/hr) | 0.972 | 1.662 | 7.812 |
| Q ($cm^3$/hr) | 337.2 | 577.2 | 2712 |
| $Pe_{im}$ | 0.029 | 0.049 | 0.234 |
| $Pe_{m/im}$ | 0.308 | 0.514 | 2.477 |

Table 3.3: Mass transport time scales

| Experiment # | 1 | 2 | 3 |
|---|---|---|---|
| $t_\alpha$ (hr) | 32.05 | 32.05 | 32.05 |
| $t_{ad}$ (hr) | 102.88 | 60.17 | 12.80 |
| $t_{ad,im}$ (hr) | 1089.80 | 637.43 | 135.60 |

diffusive flux through the inclusions was dominant over the advective flux through the matrix for Experiment #3.

We investigated this phenomena further by comparing three mass transfer times within the system: the mean diffusive time through the inclusions, $t_\alpha$; the advective time through the matrix, $t_{ad}$; and the advective time through the inclusions, $t_{ad,im}$. For the three experiments, values for these parameters are provided in Table 3.3.

We note that, when $t_\alpha < t_{ad}$, the diffusive regime is not evident within the mass recovery curve. On the other hand, when $t_\alpha > t_{ad}$, the spherical diffusion model more adequately represents the experimental data, with the diffusive regime most notable in the results from Experiment #3. Interestingly, as $t_\alpha$ approaches half the value of $t_{ad}$, the spherical diffusion model approaches a reasonable representation of the experimental data (see Figure 3.4). This was due to the assumption from the spherical diffusion model that transport through the inclusions is due to diffusion. As the diffusive residence time within the inclusions becomes longer than the advective time through the matrix, which occurs as the flow rate within the system increases, the model's assumptions become more appropriate for the experimental results.

Other than inaccurate assumptions for this model's use, at least for Experiments #1 and #2, other sources of error could propagate from the calculated dispersivity value. The value used for this study was based upon homogeneous measurements from the matrix. With this system being a combination of both matrix and inclusions, the dispersivity may change due to the influence of the inclusions on the overall transport properties.

On the basis of these observations, the multirate spherical diffusion model was re-evaluated using two fitting parameters, the dispersivity ($\alpha_{L,m}$) and the multirate diffusion parameter $\left[\ln(D^*_{im}/a^2)\right]$. Comparison of the inverse model to the experimental data is shown in Figure 3.4, with inverse fit parameters detailed in Table 3.4.

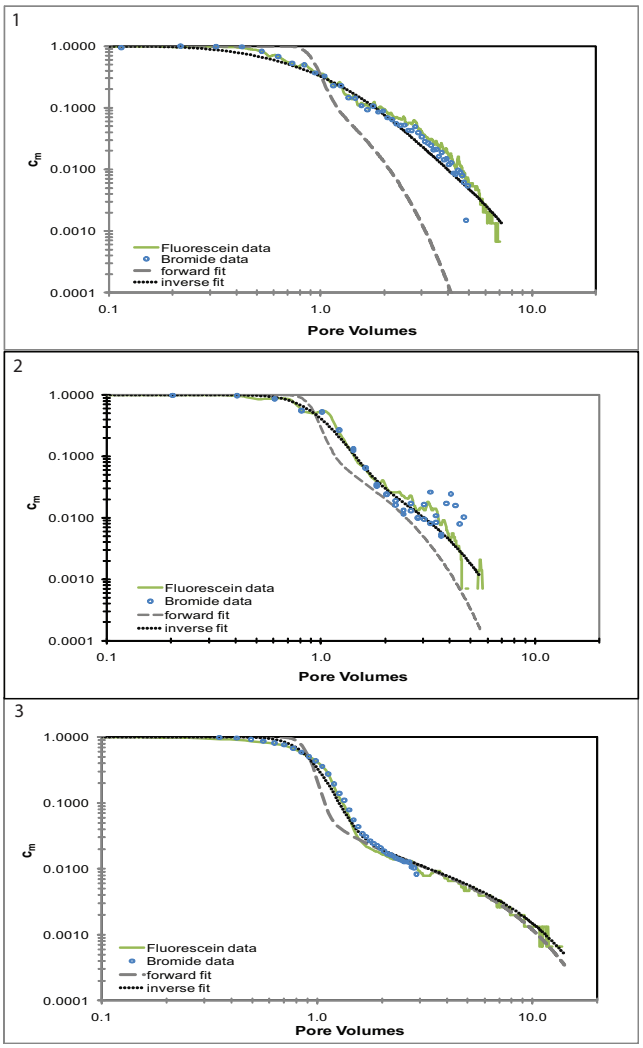


Figure 3.4: Multirate spherical diffusion model fit to data.

Table 3.4: Inverse fit parameters from multirate spherical diffusion model

| Experiment # | 1 | 2 | 3 |
|---|---|---|---|
| $v_x$ (cm/hr) | 0.97145 | 1.622 | 7.8183 |
| $\beta_{tot}$ | 0.1092 | 0.1092 | 0.1092 |
| $R_m$ | 1.0 | 1.0 | 1.0 |
| $R_{im}$ | 1.0 | 1.0 | 1.0 |
| $\alpha_{L,m}$ (cm) | 31.6938 | 4.3122 | 2.7174 |
| std. error | 0.1311 | 0.0544 | 0.0741 |
| $\ln\left(D^*_{im}/a^2\right)\left(hr^{-1}\right)$ | −7.5607 | −6.5968 | −6.2683 |
| std. error | 0.0213 | 0.0159 | 0.0114 |
| RMSE | 0.4194 | 0.2689 | 0.2176 |
| Average Standard Error | 0.2123 | 0.2100 | 0.1669 |

Table 3.5: Comparison between calculated and fit values for $D^*_{im}$ and $\alpha_{L,m}$

| parameter | $D^*_{im}$ (cm$^2$/hr) | $\alpha_{L,m}$ (cm) |
|---|---|---|
| given | 0.01358 | 0.5232 |
| Exp #1 fit | 0.00325 | 31.6938 |
| Exp #2 fit | 0.00853 | 4.3122 |
| Exp #3 fit | 0.01185 | 2.7174 |

All experiments were more adequately represented when the diffusion and dispersion coefficients were fit. A comparison between the given and fit values for $D^*_{im}$ and $\alpha_{L,m}$ are shown in Table 3.5. As can be seen, the diffusion coefficient is nearly the same between the given and fit value for Experiment #3. This is promising, since the model should provide an accurate representation of this system under these conditions. Interestingly, the dispersivity was fit at nearly five times the measured value for the homogeneous system. This indicates that the addition of the inclusions does cause an increase to the dispersivity due to the extended length for solute transport around these more diffuse objects.

Comparing the fit of the model to Experiments #1 and #2, we see that the value for the diffusion coefficient decreases while the dispersivity increases as the flow rate is reduced. This does not make sense, since the dispersivity and diffusion coefficients should not change as a function of flow rate. It is hypothesized that, due to the advective time through the matrix being longer than the diffusive time through the inclusions, the model is attempting to fit this phenomena by increasing the two fitting parameters to unrealistic values. This model is not capable of modeling a system where the concentration at the boundary between the inclusions and matrix is changing.

## 3.6 Conclusions

Three experiments were performed for this study at varying flow rates. As the flow rate within the system was increased, the tailing effects of the breakthrough curves showed a distinct change in shape. The parameters measured for the experimental system were input into the spherical diffusion model in order to determine if the model could adequately represent the experimental results. It was determined that, as the flow rate increased, the model provided a more adequate representation.

As the flow through the system was increased, the dominant mass transport mechanism changed. We began by assuming that, due to the ratio of hydraulic conductivities within the two types of media used, the spherical diffusion model would adequately represent the experimental results. After evaluating the values for the three mass transport times within the system (see Table 3.3), we noted that at slower flow rates the advective transport through the matrix and

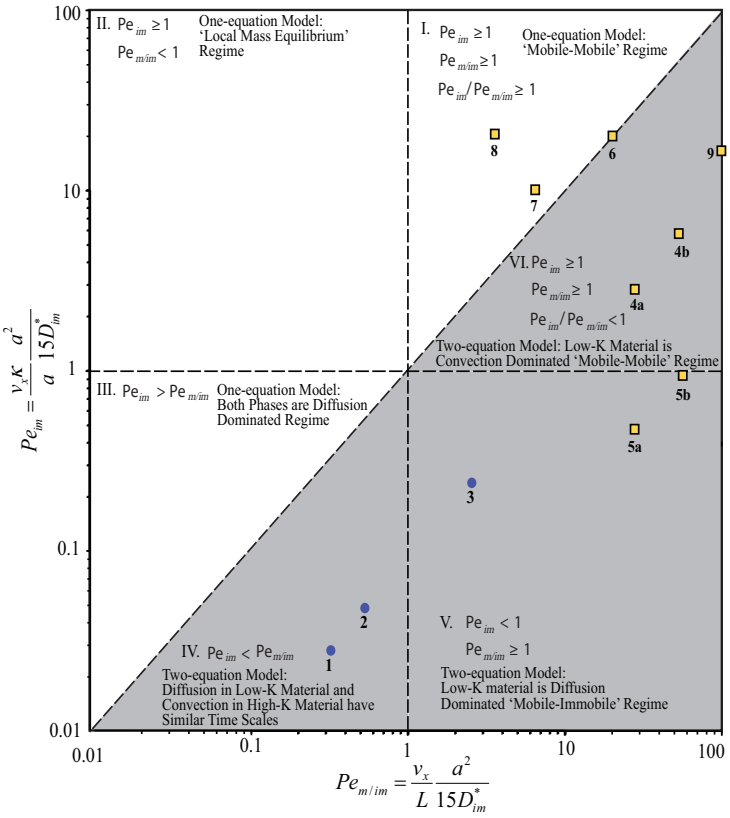


| Data Point # | Reference | Data Point # | Reference |
|---|---|---|---|
| 1 | This study: q = 5.62 ml/min | 5b | [73]: k = 1800; q = 1.32 ml/min |
| 2 | This study: q = 9.62 ml/min | 6 | [40]: Experiment 2 |
| 3 | This study: q = 45.2 ml/min | 7 | [3] |
| 4a | [73]: k = 300; q = 0.66 ml/min | 8 | [53] |
| 4b | [73]: k = 300; q = 1.32 ml/min | 9 | [34] |
| 5a | [73]: k = 1800; q = 0.66 ml/min | | |

Figure 3.5: Transport regimes as a function of $Pe_{im}$ and $Pe_{m,im}$.

the diffusive transport through the inclusions both play a dominant role in the overall transport. The diffusive time through the inclusions is shorter, but on the same order of magnitude as the advective time through the matrix for the first two experiments. At a critical flow rate (near that of the second experiment), the spherical diffusion model begins to provide a more adequate representation (see Figure 3.3) due to the advective time through the matrix becoming smaller than the diffusive time through the inclusions.

In analyzing the mass recovery curve behavior for this study, we found that there are many small scale processes influencing the overall mass transport within the system. The calculations of the Péclet numbers and mass transport time scales for the system provided insight into what was occurring within the system (e.g. diffusion out of the inclusions, advection through the

inclusions, and advection through the entire system [73]). We note that for this system, an increase to the flow rate resulted in more typical diffusion dominated mass transport through the inclusions.

Forward fitting the mass recovery curves proved adequate for the fast and medium flow rate experiments, where the spherical diffusion model followed the same trend as the experimental data. As the flow rate was decreased further, the spherical diffusion model began to deviate from the measured data. This was due to a non-constant concentration near the boundary between the matrix and inclusions. The combination of the two transport processes during complete mass recovery resulted in small-scale influences that could not be adequately described using the typical diffusion model. This was represented in Figure 3.5. The faster flow rate experiment provided values for the two Péclet numbers that fell within the diffusive mass transfer regime. As the flow rate decreased, the solute had more time to sample the varying flow velocities within the system. This allowed both the advective time within the matrix and the diffusive time within the inclusions to have similar influences on transport, which could not adequately be described by a two-equation model where the immobile phase is diffusion dominated.

The fit values for the effective diffusion coefficient increase with increasing flow rate within the system. Experiment #3 was found to be within the diffusion dominated 'mobile-immobile' mass transport regime (Figure 3.5), and the fit parameters were more meaningful due to the adequacy of the assumptions from the model. Interestingly, for Experiment #3 the inverse fit showed a nearly five times increase in the dispersivity than that assumed from homogeneous measurements. We conclude that the additions of the inclusions to the system increased the characteristic length for the dispersion as shown from the model fit. For Experiments #1 and #2, we note that the assumptions from the model construction are not adequate, therefore the fit transport parameters do not provide any numerical meaning. We believe that, as the flow rate is reduced, the impact of both the immobile diffusion coefficient and mobile advective component begin to cause some small-scale variations in overall mass transport that cannot be described using the two-equation 'mobile-immobile' diffusion model. The model tries to represent the processes occurring and attempts to fit the experimental data by adjusting the two fit parameters until the model converged to a statistically adequate representation.

The prediction of reliable estimates for bulk mass transport rates must incorporate measurements of individual fast and slow mass transport processes, which is in agreement with the conclusions made in [26]. When the advective transport through the matrix becomes longer than the diffusive time through the inclusions, the spherical diffusion model assumptions fall apart and begins to fail as the overall flow through the system was reduced. A more adequate model to represent the observations within this system would need to account for the changes in concentration at the interface between the inclusions and matrix when the advective time

through the matrix is similar in time scale to the diffusive time through the inclusions.

## Acknowledgments

This research was supported in part by the OSU/PSU IGERT Earth's Subsurface Biosphere Interdisciplinary Doctoral Fellowship program, the IWW/USGS Small Grants program, and .

# Chapter 4 – Direct Numerical Analysis of Non-Fickian Transport in a Highly Heterogeneous Laboratory System

S. J. Harrington[a], M. Porter[a], and B. D. Wood[*,a]

[a]School of Chemical, Biological, and Environmental Engineering, Oregon State University, 103 Gleeson Hall, Corvallis, Oregon, USA 97331-2702

Advances in Water Resources
11830 Westline Industrial Drive
St. Louis, MO 63146 USA
To be submitted

## 4.1 Abstract

Transport through highly heterogeneous porous media has been extensively studied; mainly for its applications to subsurface remediation, but also for many industrial processes, such as oil recovery. In order to gain a more fundamental understanding of this type of subsurface transport, we analyzed the transport of an inert solute through a highly heterogeneous experimental system at three flow rates. Physical properties and solute transport parameters were measured prior to and during the experimental construction. The tracer, containing fluorescein and lithium bromide, provided mass recovery curves at flow rates of 5.62, 9.62, and 45.2 ml/min. All measurements from the experimental system were used to construct a three-dimensional representation using the commercially available computational fluid dynamics software STAR-CCM+. This direct numerical simulation used the average measured values for the diffusion coefficient and dispersivity from homogeneous simulations, with the assumption that a single set of transport parameters could be used to describe the results from all three experiments. From the initial comparison, the single set of measured transport parameters was found to be inadequate at representing all three experiments. Subsequent analysis, adjusting the dispersivity of the matrix and diffusion coefficient for the inclusions, resulted in an improved fit, but was still unable to capture the trend of the late time mass recovery for all three studies. The DNS representation, using measured parameters, was compared to a multirate spherical diffusion model representation to determine how well the two compared. Interestingly, the DNS was incapable of providing the same numerical results as the upscaled model. Therefore, further refinements need to be made before its ability to represent this experimental system can be analyzed.

## 4.2 Introduction

Understanding of solute transport within the subsurface is important for applications including contaminant remediation (such as for the sites on the EPA's National Priorities List [20]), oil recovery [36], and crop irrigation to name a few. A number of theoretical models have been developed to represent the transport processes occurring within highly heterogeneous porous media, where there is a high variance in the log-conductivities of the sediments involved [6, 5, 11, 14, 17, 29, 45, 50, 66, 70, 71, 72]. Highly heterogeneous flow fields draw out solute transport considerably, resulting in long, non-Fickian 'tailing'. This phenomenon cannot adequately be described using the conventional advection-dispersion equation (ADE) [6], leading to an increased interest to develop a more robust modeling approach.

The focus of this work is to integrate both experimental and theoretical results to gain a more fundamental understanding of solute transport in highly heterogeneous porous media. This is done with the use of a laboratory constructed highly heterogeneous environment (e.g.

a binary spatial conductivity field) consisting of two distinct regions: (1) a high hydraulic conductivity (e.g. $K_m$ = 4.66 cm/min) matrix material, and (2) low conductivity (e.g. $K_{im}$ = 0.011 cm/min) inclusions. This type of system has been found in natural environments [8, 47, 55] and represents a simplistic application for this solute transport research.

To begin, a three-dimensional experimental flowcell was randomly packed with two materials, a high conductivity matrix and 203 low conductivity spherical inclusions as detailed in Section 4.3 and Appendix A.1. Three transport experiments were performed at different flow rates, with the resulting concentration versus time data collected from time zero, or completely saturated, to a final time when no measurable concentration was coming out of the flowcell. A numerical representation of the system, detailed in Section 4.3.4, was subsequently formulated using the commercially available STAR-CCM+ (©CD-Adapco) computational fluid dynamics (CFD) software. This representation was constructed using average measured parameters. Our objective was to determine how well these parameters represented the overall transport for all three experiments through comparison between the model and experimental results. An analysis of the experimental data and flow through the two materials is presented in Section 4.5.1, with the comparison to the direct numerical simulation (DNS) given in Section 4.5.2.

## 4.3 Material and Methods

The heterogeneous experimental system was constructed through the use of two sizes of Spheriglass solid glass spheres (Potters Industries Inc., Valley Forge, PA). A larger particle size sand was used as the matrix material, with a finer material used to construct the spherical inclusions.

### 4.3.1 Matrix material

The matrix was constructed from A-240 Spheriglass solid glass spheres with a particle size range between 2 and 2.8 mm. Its bulk density (2.5 ±0.1 g/cm$^3$) was calculated by performing water displacement measurements, whereas hydraulic conductivity (4.66 ±0.96 cm/min) was determined through the use of a constant head permeameter. Porosity (0.40 ±0.03) was measured during wet packing of the experimental system. The matrix portion of the experimental set-up provided approximately 86.7% of the total volume.

### 4.3.2 Inclusions

Spherical inclusions were prepared by sintering low conductivity 2530 Spheriglass solid glass spheres within graphite carbon molds of a sphere (internal diameter = 5 cm). The 2530 material had an initial average particle size of 0.07 mm and hydraulic conductivity, calculated using a falling head permeameter, of 0.0032 cm/min. The molds were filled and heated two at a time in

a muffle furnace at 725°C for 2.5 hours. After cooling overnight, the inclusions were removed and sanded using fine grain sand paper in order to remove any loose material and ensure they each had a smooth spherical shape. Each inclusion was numbered and subsequently weighed to obtain its individual dry weight.

The dry inclusions were then purged with carbon dioxide ($CO_2$) to remove all air from the pore space and allow for more thorough saturation due to its higher solubility in water. This was followed by saturating with a solution of 100 ppm sodium borate in DI water. Sodium borate was used as a microbial growth inhibitor. The saturated inclusions were weighed, with the difference between their dry and wet weight being used to determine their individual porosity ($\theta_{im}$; see Table A.1 in Appendix) using Eq. 4.1. Porosity is equal to the product of the difference between the weight of the inclusion when saturated and their dry weight with the density of water, providing the volume of fluid within the inclusion, divided by the sum of the solid and fluid volumes.

$$\theta_{im} = \frac{V_{fluid}}{V_{solid} + V_{fluid}} \tag{4.1}$$

Individual hydraulic conductivities were calculated through the use of pressure drop measurements. This was achieved using a dual syringe pump attached to a stainless steel column, with measurements of pressure taken before and after the inclusion (see Figure 4.1). The inclusions were individually placed within the stainless steel column, and held in place using c- and o-rings. Pressure drop was measured as centimeters water at a constant flow rate, with these values subsequently used to calculate conductivity via Darcy's Law, shown in Eq. 4.2.

$$K_{im} = -\frac{Q}{A_{im}} \frac{dh_{im}}{dL} \tag{4.2}$$

In this equation, $K_{im}$ is the hydraulic conductivity of the inclusion [length/time]; $Q$ is the flow rate through the column [length$^3$/time]; $A_{im}$ is the cross-sectional area of the inclusion [length$^2$]; $dh_{im}$ is the pressure drop measured across the inclusion [length]; and $dL$ is the length between the two pressure measurement ports.

Once all measurements had been performed in duplicate, they were again submerged in the 100 ppm sodium borate solution. Averages from all 203 inclusions used within the experimental system resulted in an average bulk density of 2.43 ±0.1 g/cm$^3$, hydraulic conductivity of 0.011 ±0.007 cm/min, and porosity of 0.31 ±0.003. As can be seen, the sintering process resulted in an over three fold increase for the hydraulic conductivity value from the loose material, changing from 0.0032 cm/min for the 2530 sand to an average of 0.011 cm/min for the sintered spheres.

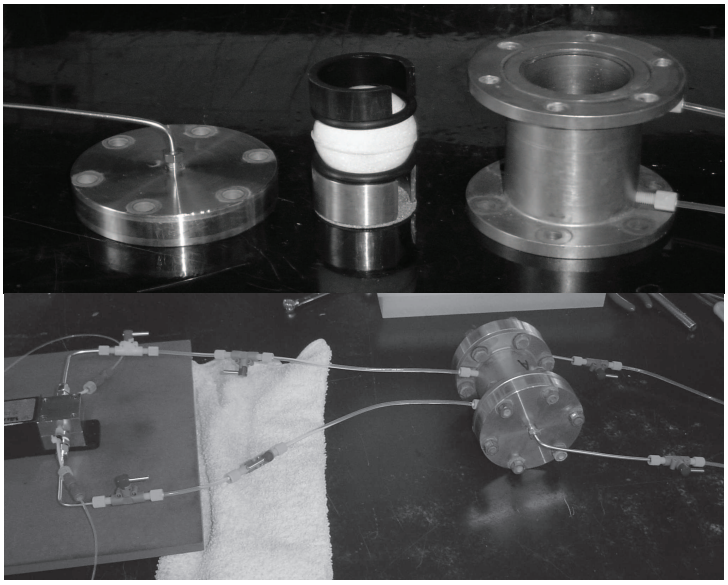

Figure 4.1: Equipment for measuring pressure drop across inclusion. Top: Column and internal configuration used for measuring pressure drop across inclusions. Bottom: Pressure transducer connected to column with inclusion.

### 4.3.3 Experimental Design

The experimental system consisted of an aluminum flowcell with an internal height, width, and depth of 1 m x 0.5 m x 0.2 m. The flowcell was constructed of individual 1.6 cm cast aluminum sheets that were machined to be connected with hex-head bolts. The flowcell was wet packed, with the saturated inclusions placed within the high conductivity matrix material as determined using a randomizing code written in Matlab (see Appendix, section A.1). This code was used to achieve the packing structure for the inclusions through the use of its random number generator (see Figure 4.2). Since each inclusion was numbered, their individual position within the experimental volume was noted in (x,y,z) coordinates (see Table A.1 in Appendix A.1). The mass of added tracer (34,713 ±2 g) and A-240 matrix material (139,365 ±4 g) were recorded in order to calculate the porosity of the matrix material.

The tracer consisted of a 100 ppm sodium borate solution, with lithium bromide and fluorescein added as inert solutes. Each experiment had slightly different concentrations, with the measured values shown in Table 4.1 below. The pH of the solution was adjusted to 9.3 ±0.3, since the maximum peak emission for fluorescein was found to be near this pH value [13]. This solution was pumped through the flowcell prior to each experiment in order to ensure both the matrix and inclusions were saturated with this solution. Complete saturation was determined through a comparison of samples taken at the inlet and outlet.

Three experiments were conducted with average flow rates of 5.62 ±0.48 ml/min, 9.62

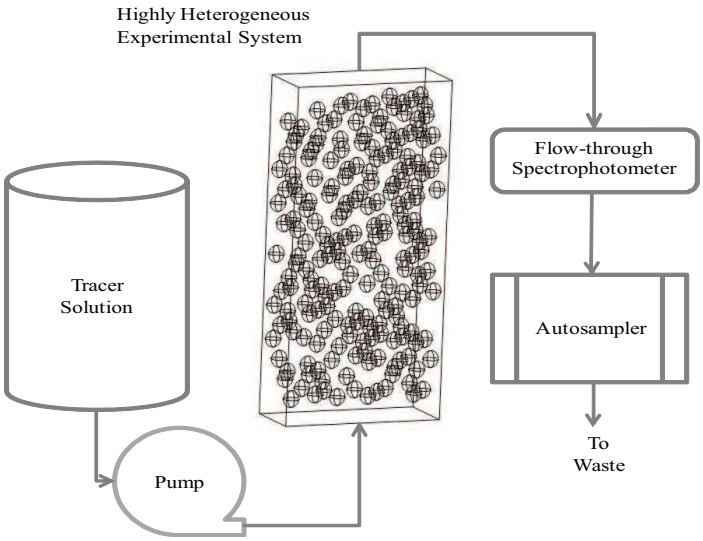


Figure 4.2: Experimental set-up for Highly Heterogeneous System

Table 4.1: Measured tracer concentrations for each experiment.

| Experiment # | $Br^-$ (ppm from LiBr) | Fluorescein (ppm) |
|---|---|---|
| 1 | 30 | 1.50 ±0.02 |
| 2 | 27 | 1.43 ±0.02 |
| 3 | 30 | 1.52 ±0.02 |

±0.68 ml/min, and 45.2 ±3.53 ml/min. The tracer solution was recovered by injecting a 100 ppm sodium borate solution at pH 9.3 ±0.3 through the inlet. With the use of the flow rates and calculated volumes of fluid within the inclusions and matrix, the time for one pore volume (PV) was calculated to be approximately 114.2 hours, 66.73 hours, and 14.2 hours for Experiments #1, #2, and #3, respectively. One PV was equivalent to the time it took to replace all of the fluid within the system (e.g. the total volume of fluid within the matrix and inclusions divided by the flow rate).

### 4.3.4 Analytical Tools

Concentration measurements for fluorescein were obtained for the first and third experiments using a model 10-AU-005-CE fluorometer (Turner Designs, Sunnyvale, CA) with a flow cell sampler. A flow-through spectrophotometer with OOIBase 32 software from Ocean Optics was used for the second experiment. Throughout the three studies, samples were taken at the outlet for analyses of bromide ($Br^-$) using a Gilson 223 sample changer and anlayzed using ion chromatography (IC; Dionex DX-120).

## 4.4 Theory

### 4.4.1 Experimental Transport Parameters

Transport parameters were measured prior to and during wet packing of the flowcell. There was only one parameter (flow rate; $Q$) that varied between the three experiments. Since the same system was used for all three flow rate analyses, we assume that a single set of transport parameters should be adequate in describing all of the experimental results. Measured parameters used in the model included the average porosity of the inclusions ($\theta_{im}$) and matrix ($\theta_m$), the molecular diffusion coefficient for fluorescein ($D$), and the effective diffusion coefficient for the inclusions ($D^*_{im}$) and matrix ($D^*_m$) which were calculated using the Maxwell relation:

$$D^*_x = D\left(\frac{2}{3-\theta_x}\right) \quad \text{for } x = \text{im or m} \tag{4.3}$$

The average hydraulic conductivities of the matrix ($K_m$) and inclusions ($K_{im}$) were also used, along with the longitudinal and transverse dispersivities for fluorescein within the matrix ($\alpha_{L,m}$ and $\alpha_{T,m}$) and inclusions ($\alpha_{L,im}$ and $\alpha_{T,im}$), with the transverse dispersivity assumed to be $1/10^{th}$ of the calculated longitudinal value. Flow rate measurements were taken periodically throughout each of the three experiments (see Table A.7 in Appendix A.4) and averaged. The final parameters used for the simulations are shown in Table 4.2.

Table 4.2: Parameters used within CFD model.

| Parameter | Value |
|---|---|
| $\theta_m$ | 0.40 |
| $\theta_{im}$ | 0.31 |
| $D\left(\frac{m^2}{s}\right)$ | 4.900E-10 |
| $D^*_m\left(\frac{m^2}{s}\right)$ | 3.769E-10 |
| $D^*_{im}\left(\frac{m^2}{s}\right)$ | 3.643E-10 |
| $K_m\left(\frac{m}{s}\right)$ | 7.767E-04 |
| $K_{im}\left(\frac{m}{s}\right)$ | 1.833E-06 |
| $\alpha_{L,m}$ (m) | 5.232E-03 |
| $\alpha_{T,m}$ (m) | 5.232E-04 |
| $\alpha_{L,im}$ (m) | 1.522E-03 |
| $\alpha_{T,im}$ (m) | 1.522E-04 |
| $Q_1\left(\frac{m^3}{s}\right)$ | 9.367E-08 |
| $Q_2\left(\frac{m^3}{s}\right)$ | 1.603E-07 |
| $Q_3\left(\frac{m^3}{s}\right)$ | 7.533E-07 |

### 4.4.2 CFD Design

The computer simulation was created using Star-CCM, with flowcell dimensions of 1 m x 0.51 m x 0.21 m. The width and depth were made slightly larger than the actual dimensions in order to remove errors, since some of the inclusions were touching the wall in the actual experimental flowcell. The geometry of the inclusions were then added, with their centers described according to the measured (x,y,z) coordinates (see Table A.1 in Appendix A.1).

After the geometry was created, the boundary conditions were then selected. For the flowcell, the inlet face was set to a constant velocity, the walls were set as no-flow, and the outlet face was set to a constant atmospheric pressure. The inlet and outlet boundary conditions were located along the whole face, whereas the experimental system had 24 evenly spaced ports along the inlet and outlet faces to direct flow. The interface between the matrix and inclusions was set to a continuity boundary.

Once the geometry and boundary conditions were set, the simulation was run twice. The first run determined the steady-state flow field. This provided velocity information throughout the geometry. Once this was solved, and found to be grid and time step independent, the results were subsequently used to solve the transient transport model. For this simulation, the concentration in the flowcell was set to a normalized concentration of 1, with the inlet set to a constant concentration of zero. At the outlet, the diffusive flux of concentration was set to zero so the tracer could only exit the system by convection.

Different conductivity and porosity values were programmed for the inclusions and matrix. Average measured values for the diffusion coefficient and dispersivity were also input into the model. Since the velocity field was solved for in each volume grid, the dispersion tensor could be calculated at each individual volume mesh throughout the geometry using the equation $\mathcal{D} = \alpha * v + D^*$. The only variability between the three simulations was the velocity and dispersion tensor field due to the three different values for the flow rate, $Q$.

For the transport model, the Distributed Resistance (Porous Media) Flow method was used. Initial conditions were a constant initial concentration throughout the geometry, with a zero concentration along the inlet face at time greater than zero. The CFD simulation was then run using the default solvers. The final solution was subsequently optimized to achieve mesh and time-step convergence.

## 4.5 Results

### 4.5.1 Experimental Data Analysis

The experimental mass recovery curves were prepared using concentration versus time data collected from all three transport studies (data available in Appendix A.2). Results showed

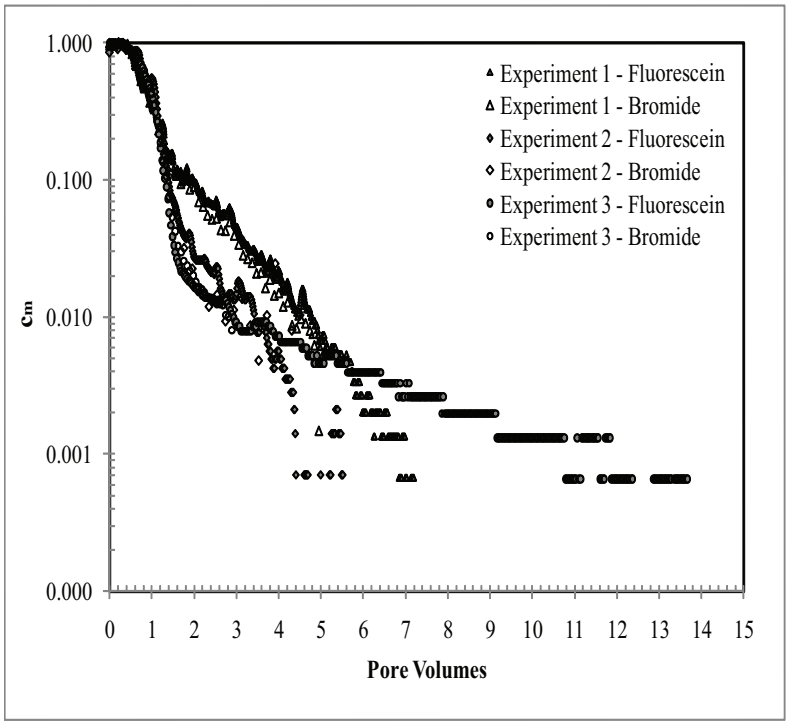


Figure 4.3: Dimensionless plots of all experiments

slight variations between the slow, medium, and fast flow rates (see Figure 4.3). The slower flow rates (Experiments #1 and #2) showed faster removal of concentration from the system, with nearly identical late-time slopes. At about two pore volumes, Experiment #3 began to show a reduction in slope, leading to what is typically referred to as classic non-Fickian tailing. Overall mass recovery took slightly over 7, 5, and 12 pore volumes for Experiments #1, #2, and #3, respectively.

In order to more thoroughly analyze why the three experiments behaved differently, we calculated two different Péclet numbers. The immobile Péclet number, $\mathrm{Pe}_{im}$, compared the ratio of the diffusive ($a^2/15D^*_{im}$) and advective ($a/v_x\kappa$) times within the inclusions. The mobile/immobile Péclet number, $\mathrm{Pe}_{m/im}$, compared the diffusive time in the inclusions to the advective time in the matrix ($L/v_x$). These have previously been shown as $\mathrm{Pe}_{\omega\omega}$ and $\mathrm{Pe}_{\eta\omega}$ in Golfier et al. [22], or as a Péclet number and a Damköhler number in Zinn et al. [73]. The immobile Péclet number was calculated by

$$\mathrm{Pe}_{im} = \frac{v_x\kappa}{a}\frac{a^2}{15D^*_{im}} \tag{4.4}$$

whereas $\mathrm{Pe}_{m/im}$ was calculated using

$$\mathrm{Pe}_{m/im} = \frac{v_x}{L}\frac{a^2}{15D^*_{im}} \tag{4.5}$$

To determine the values for these parameters, the average pore water velocity within the matrix $\left(v_x = \frac{Q}{V_m A_{xc} \theta_m}\right)$, the radius of the inclusions ($a$ = 2.5 cm), the total length of the system ($L$ = 100 cm), and the ratio of hydraulic conductivities of the inclusions to that of the matrix ($\kappa = \mathrm{K}_{im}/\mathrm{K}_m$ = 0.00236) were calculated. For the average pore water velocity, the flow rate ($Q$) was divided by the product of the volume fraction of matrix material in the system ($V_m$ = 0.867), the cross-sectional area of the system ($A_{xc}$ = 1000 cm$^2$), and the porosity of the matrix material ($\theta_m$ = 0.40). Results of these calculations for all three experiments are shown in Table 4.3.

Table 4.3: Mass transport time scales for each experiment.

| Experiment # | $v_x$ (cm$^3$/hr) | $\frac{a}{v_x \kappa}$ (hr) | $\frac{a^2}{15D^*_{im}}$ (hr) | $\frac{L}{v_x}$ (hr) | $\mathrm{Pe}_{im}$ | $\mathrm{Pe}_{m,im}$ |
|---|---|---|---|---|---|---|
| 1 | 0.972 | 1089.80 | 32.05 | 102.88 | 0.029 | 0.308 |
| 2 | 1.662 | 637.43 | 32.05 | 60.17 | 0.049 | 0.514 |
| 3 | 7.812 | 135.60 | 32.05 | 12.80 | 0.234 | 2.477 |

The Péclet numbers were then plotted in Figure 4.4. This figure is similar to that shown in previous studies [73, 22], and is an indicator of the predominant flow regimes for mass transport as a function of the two Péclet numbers. In comparing where the three experiments lie, a noticeable change in the dominant mass transport process within the inclusions could be seen as the flow rate was increased. The first two experiments fell in a regime that until now was unlabeled, whereas the third experiment fell within the regime where the immobile phase is more diffusion dominated. As diffusion within the inclusions began to dominate over mass transport, the resultant mass recovery curve began to show more predominant non-Fickian tailing. This explains the differences between the total time for mass recovery between the three curves, as diffusion dominated flow results in longer, more drawn out tailing.

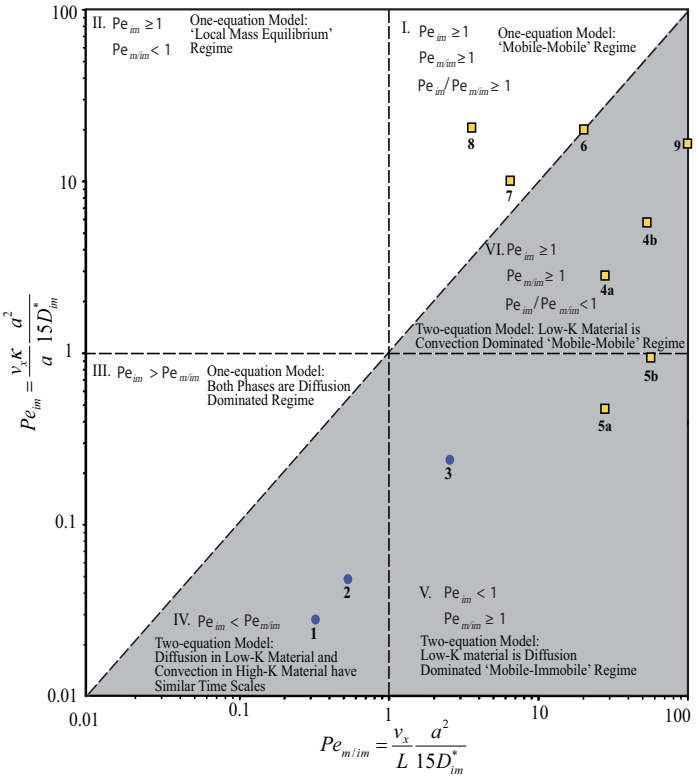


| Data Point # | Reference | Data Point # | Reference |
|---|---|---|---|
| 1 | This study: q = 5.62 ml/min | 5b | [73]: k = 1800; q = 1.32 ml/min |
| 2 | This study: q = 9.62 ml/min | 6 | [40]: Experiment 2 |
| 3 | This study: q = 45.2 ml/min | 7 | [3] |
| 4a | [73]: k = 300; q = 0.66 ml/min | 8 | [53] |
| 4b | [73]: k = 300; q = 1.32 ml/min | 9 | [34] |
| 5a | [73]: k = 1800; q = 0.66 ml/min | | |

Figure 4.4: Transport regimes as a function of $Pe_{im}$ and $Pe_{m,im}$.

### 4.5.2 Model Comparison

The DNS was initially compared with the experimental data to determine how well it represented the processes occurring within the 3D flowcell. Further comparison was performed with a multirate spherical diffusion model from the STAMMT-L software [30] in order to ensure the model was functioning properly and producing accurate results. The results of these comparisons are detailed below.

#### 4.5.2.1 Comparison of Fit with Experimental Data

Measured concentration versus time data from the outlet of the flowcell (see Appendix, Tables A.2, A.3, and A.4 for Experiments #1, #2, and #3, respectively) were then compared to the

concentration (summed over the outlet face of the DNS) versus time data from the model for analysis, as seen in Figure 4.5. For all initial model runs, the DNS did not represent the experimental results as well as anticipated.

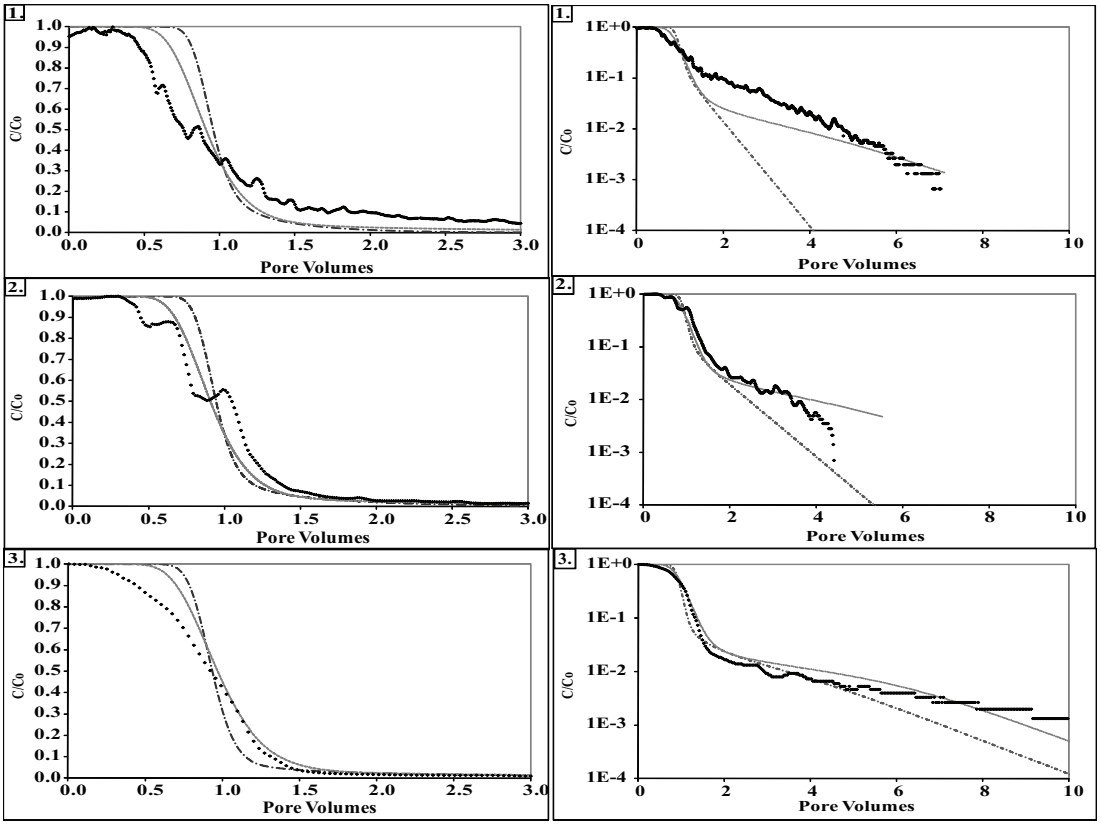


(a) Early Time Data Comparison (b) Late Time Data Comparison

Figure 4.5: Comparison between experimental data and STAR-CCM+ DNS, where numbered graphs represent corresponding experiment number. (a) Focus on early-time comparison between the experimental data and DNS results, shown in arithmatic scales; (b) Focus on late-time comparison between the experimental data and DNS results, shown in logarithmic scale. Symbols = experimental data, dot-dash line = initial DNS fit, and dotted line = DNS with adjusted parameters.

The average relative errors between the model and experimental data were calculated using Eq. 4.6, and are shown in Table 4.4. The relative error was set equivalent to the magnitude of the difference between the experimental concentration value at time step i, $c_{m,i,experiment}$, and the model concentration at the same time step, $c_{m,i,model}$, and dividing by the magnitude of the experimental concentration at time step *i*. The average relative error was the sum of all of the *i* time steps, where *i* equals 1 through *n*, divided by the total number of time steps, *n*.

$$\text{Average Relative Error } = \frac{1}{n}\Sigma_{i=1}^{n}\left(\frac{|(c_{m,i,experiment} - c_{m,i,model})|}{c_{m,i,experiment}}\right) \tag{4.6}$$

Table 4.4: Average relative error between initial simulation and experimental data.

| Experiment # | Average Relative Error |
|---|---|
| 1 | 83.03 % |
| 2 | 49.26 % |
| 3 | 54.34 % |

The average relative error was 83% for the first experiment, where the model did not adequately represent the initial drop in concentration or the final concentration tailing within the mass recovery curve. Improved representations were seen with the second and third experiments, but the model still did not follow the initial experimental drop in concentration at early times. Examination of these figures indicated potential underestimation of the overall transport parameters describing the system. Initially, the dispersion and diffusion parameters were calculated for the individual porous media within the system. It was hypothesized that the combination of the two media could have altered these two parameters; therefore, adjustments were made within the model.

For the matrix material, the dispersivity was multiplied by a factor of 5. This was done to adjust for the inclusions, which may have caused more spreading of the initial concentration front within the system. It was assumed that the majority of the initial mass recovery would be from the tracer within the matrix. If this volume had to move around the inclusions, due to their slow mass transport behavior, the homogeneous dispersivity value used may have been too small.

The inclusion diffusion coefficient was also adjusted by dividing by a factor of 10. This initial value was based upon Maxwell's equation, which takes into account the porosity of the material and the molecular diffusion coefficient for fluorescein. For the inclusions, the individual porosities varied between 0.18 to 0.38, with an average of 0.31, while the molecular diffusion coefficient was obtained from a paper by Saylor et al. [52]. The molecular diffusion coefficient could easily be as much as an order of magnitude smaller due to the sintering process used in the construction of the inclusions. The variability of the porosities could have also reduced the overall diffusion coefficient for the inclusions, with the average value being an inadequate assumption for use with this parameter.

With these adjustments, the refined DNS showed significant improvement (see Figure 4.5, dotted line versus symbols) in both the fit of the simulation at early-time, which was due mostly to the increased value of the matrix dispersivity, as well as the late-time data, due in part to the reduction of the inclusion diffusion coefficient. The overall adjustments to the

simulation provided adequate representations of the fast and medium flow rate data, but was still lacking in its ability to represent the late-time results from Experiment #1. The average relative error between the simulations and experiments are shown in Table 4.5, showing a noticeable reduction from the original simulation.

Table 4.5: Average relative error between adjusted simulation and experimental data.

| Experiment # | Average Relative Error |
|---|---|
| 1 | 44.35 % |
| 2 | 36.99 % |
| 3 | 44.51 % |

#### 4.5.2.2 Comparison of Fit with Multirate Model

In comparing the fit between the model representation and the experimental results, it was hypothesized that there may be some inconsistencies in the model construction resulting in its failure to fit all three experiments. This was analyzed through comparison of its results with a multirate spherical diffusion model.

The multirate spherical diffusion model is a more upscaled modeling approach. It takes into consideration key assumptions in order to simplify the mathematical solution. Some of these assumptions include: (1) one-dimensional dual porosity transport; (2) a purely diffuse immobile low-conductivity spherical zone; (3) steady-state flow; (4) rate limited mass transport between the two domains; and (5) continuity of concentration at the interface between the mobile and immobile domains. The general form of the multirate model employed by STAMMT-L is shown in Eqs (4.7) through (4.13) below.

ADMT
$$\frac{\partial c_m}{\partial t} + \Gamma = \frac{\alpha_{L,m} v_x}{R_m} \frac{\partial^2 c_m}{\partial x^2} - \frac{v_x}{R_m} \frac{\partial c_m}{\partial x} \quad \text{for } 0 < x < L \tag{4.7}$$

Sphere Source/Sink
$$\Gamma = \int_0^\infty \beta_{tot} \frac{\partial c_m(t-\tau)}{\partial t} g^*(\tau) d\tau \tag{4.8}$$

Initial Conditions
$$c_m|_{t=0} = c_{im}|_{t=0} = 1 \tag{4.9}$$

Upstream B.C.
$$c_m|_{x=0} = 0 \tag{4.10}$$

Downstream B.C.
$$\left.\frac{\partial c_m}{\partial x}\right|_{x=L} = 0 \tag{4.11}$$

Outer B.C. for Inclusions
$$c_{im}|_{r=0} = c_m \tag{4.12}$$

B.C. for Center of Inclusions
$$\left.\frac{\partial c_{im}}{\partial r}\right|_{r=a} = 0 \tag{4.13}$$

Equation (4.7) is the basic form of ADMT, with the source/sink term ($\Gamma$) for the multirate distribution given by Eq (4.8). In the ADMT equation, $c_m$ [mass/length$^3$] is the cross-sectional area averaged concentration in the matrix; $\alpha_{L,m}$ [length] is the longitudinal mobile dispersivity; $v_x$ [length/time] is the average axial pore water velocity in the mobile phase, as the inclusions are assumed to be purely diffuse; $t$ is time; $x$ [length] is the space coordinate; and $R_m$ [-] is the mobile retardation coefficient. For Eq (4.8), $\beta_{tot}$ [-] is the capacity coefficient, defined as the ratio of immobile domain pore space to mobile domain pore space, and $g^*(\tau)$ $\left[T^{-1}\right]$ is the memory function. The initial concentration in both the matrix and inclusions (e.g. mobile and immobile phase, described by $c_m$ and $c_{im}$) are 1, as seen in Eq (4.9), and the injected concentration at $t = 0$ is zero in Eq (4.10). The downstream boundary condition for the matrix is set to be zero flux [Eq (4.11)]; the outer boundary of the inclusions are assumed to be the same concentration as the surrounding matrix [Eq (4.12)]; and the center boundary of the inclusions is also set to be zero flux [Eq (4.13)].

The functional form of the memory function, $g^*(t)$, is dependent upon the particular mass transport model being used. These functions can be thought of as the probability density of a molecule, having entered the immobile zone at $t = 0$, to be remaining in the immobile zone at time $t$. The memory function is related to the spherical diffusion rate coefficient by Eq (4.14), where $a$ is the radius of the inclusions [length].

$$g^*(t) = \sum_{j=1}^{\infty} 6\beta_{tot} \frac{D^*_{im}}{a^2} \exp\left[-j^2\pi^2 \frac{D^*_{im}}{a^2} t\right] \tag{4.14}$$

This numerical model was run using the same measured values from the experimental flow-

cell in order to compare the two model results, which are shown in Figure 4.6. It is evident through this comparison that further refinements need to be made to the DNS in order to validate its application for this experimental system. The most prominent discrepancy with its representation of the results is seen at longer times, where the diffusive tailing occurs. This leads one to assume there are either inconsistencies in the geometry of the DNS, the boundary conditions between the inclusions and matrix are not adequately represented, or other issues are causing deviations with the model's ability to represent diffusion out of the inclusions accurately.

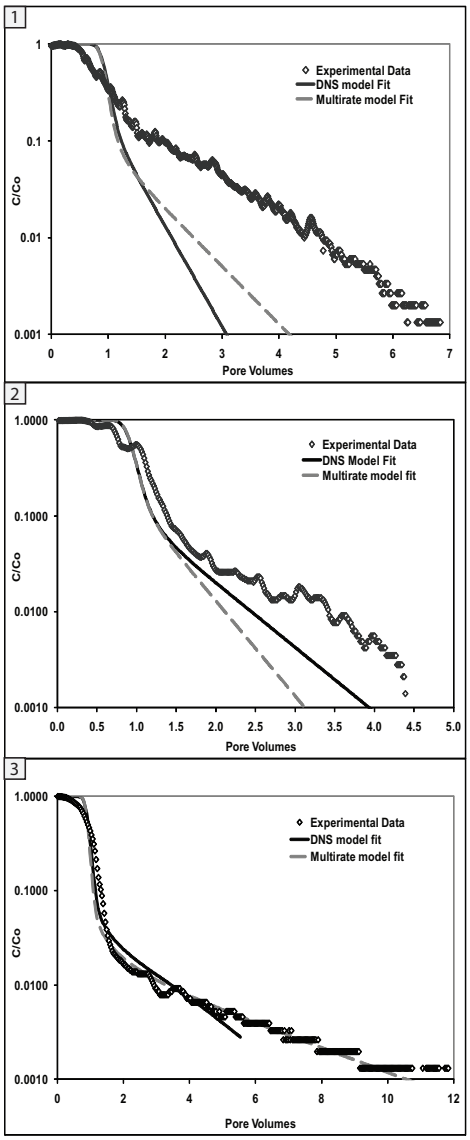


Figure 4.6: Comparison of DNS and Multirate numerical results for Experiments #1, #2, and #3.

## 4.6 Discussion and Conclusions

Numerous theoretical methods have been, and are currently being developed in an attempt to more adequately represent the processes affecting transport within highly heterogeneous environments. This study focused on the ability of a DNS, created using the commercially available CFD software STAR-CCM+ (© CD-Adapco), to adequately represent a synthetic highly-heterogeneous environment. The experimental system was thoroughly characterized prior to and during construction in order to obtain all relevant information that would be necessary to create an accurate model representation. Three experiments were run within this flowcell at increasing flow rates. Mass recovery data was collected at the outlet in order to validate the DNS results.

Experimental mass recovery curves showed variability in the tailing for the three flow rates. Experiments #1 and #2 resulted in faster removal of concentration from the system when compared to Experiment #3. The data from Experiment #3 was indicative of what is typically viewed as non-Fickian tailing. This was evident by the initial sharp decrease in concentration followed by a prolonged narrow tailing, with complete mass recovery taking longer than any of the other experiments.

The overall shapes of the three mass recovery curves could be justified through an examination of the dominant mass transport regimes. This was achieved through a comparison of the immobile and mobile/immobile Péclet numbers, $\mathrm{Pe}_{im}$ and $\mathrm{Pe}_{m/im}$. As the flow rate was increased, the dominant mass transport process within the inclusions changed. Experiments #1 and #2 fell within the regime where diffusion in the inclusions and convection in the matrix have similar time scales. This meant that transport through both media were influencing the overall mass recovery curve. Experiment #3 was in the regime where the immobile phase was more diffusion dominated; mass transport through the matrix was due to the overall flow rate, while transport through the inclusions was mostly due to diffusion.

The DNS was constructed such that a single set of parameters were used to explain all of the experiments. Initial simulations provided an adequate representation of the system, with error reduction possible through further refinement of the dispersivity of the matrix and diffusion coefficient for the inclusions. The dispersivity of the matrix material was adjusted by a factor of five increase, while the diffusion coefficient for the inclusions was reduced by a factor of $1/10^{th}$. These refinements were performed due to uncertainties in the initial values, which were obtained from measurements taken from the individual materials and published values. The refined simulation showed improved correlations to the experimental results, indicating that the heterogeneity of the system resulted in variability of these parameters.

Due to the change in dominant mass transport regimes between the experiments, we believe a single set of parameters may not be adequate for all three flow rates. This is assumed due to the large difference shown between the three late-time slopes in Figure 4.3. As an example,

the dispersivity of the matrix was adjusted with the assumption that mass transport through the inclusions was impeding flow through the system similarly for all three experiments. Since this is not accurate for the first two experiments due to the change in the dominant mass transport process for the inclusions, the value of the dispersivity may vary between the three studies.

Through comparison of the DNS results with a multirate spherical diffusion model, it is evident that further adjustments are necessary in order to improve its correlation to the experimental results. The two numerical methods should have provided the same solutions when the identical parameters were used for both. This was proven not to be the case, as could be seen in Figure 4.6. The DNS may not be an adequate method of representing this type of experimental system. Further work on its construction and refinements to its development are necessary to determine its ability to represent this type of complex environment. Further theoretical work is planned to determine if the DNS would be an applicable numerical method to describe flow through highly heterogeneous binary spatial conductivity fields.

## Acknowledgments

This research was supported in part by the OSU/PSU IGERT Earth's Subsurface Biosphere Interdisciplinary Doctoral Fellowship program, the IWW/USGS Small Grants program, and

# Chapter 5 – Overall Conclusions

This research focused on merging experimental research with theoretical analysis. Two experimental systems were analyzed. The first focused on how chemical adjustments made to a natural sediment affected the transport of a reactive chemical solute. The second focused on how a physically heterogeneous system affected transport of an inert solute. Both systems resulted in the development of non-Fickian 'tailing,' which could not adequately be represented using the conventional ADE. For the first experimental system (Chapter 2), the resultant data were fit using a multirate reaction model available within the STAMMT-L code [30]. The second experimental system was initially simulated using a multirate spherical diffusion model (Chapter 3) available within the STAMMT-L code, and subsequently analyzed by a DNS (Chapter 4) performed using the commercially available computational fluid dynamics software STAR-CCM+ (©CD-Adapco).

The two theoretical analyses varied in that the DNS was theoretically capable of describing processes occurring at the smaller 'Darcy' scale, while the multirate STAMMT-L model was an upscaled version of this microscale model. The DNS solves the conservation equations, using different parameter values to describe flow through the two distinct types of media used within the system. STAMMT-L modifies the ADE by incorporating a source/sink term, and makes assumptions concerning the dominant mass transport processes for the overall system. Prior to analysis, it was assumed that both theories were adequate for their respective use.

In Chapter 2, two multirate reaction models were compared to experimental BTCs. Results showed that without full mass recovery data, the fit model simulation parameters were suspect. It was uncertain whether the parameters fit by the model would change had there been complete mass recovery data available. Overall, the model was able to represent the experimental results well and provided some useful indications of how the mobility of the solute was affected due to adjustments made to the sediment chemistry. Improvements could have been made if more thorough measurements and analyses had been available for the system.

In Chapter 3, analysis of experimental results from the highly heterogeneous experimental system were performed using a multirate spherical diffusion model. Initial results using measured parameter values showed adequate representation of Experiment #3, with larger errors between the model and data for the other two experiments. The model was allowed to fit the data by varying the diffusion and dispersivity. More adequate representations were achieved with smaller diffusion coefficients for the inclusions and a larger longitudinal dispersivity values for the matrix. Upon further examination of the time scales of mass transport within the inclusions and matrix, we noted that this model was not appropriate for Experiments #1 and

#2. This was due to the diffusion in the inclusions and the advection in the matrix having similar time scales. When diffusion out of the inclusions does not take longer than advection out of the matrix, the spherical diffusion model becomes inadequate due to its assumption of continuity of concentrations at the interface between the two phases. Therefore, this model should not be relied upon for these cases. Interestingly, for Experiment #3 the fit values for the diffusion coefficient and dispersivity provided some insight into how the addition of the inclusions affected the homogeneous measurements used to describe the overall solute transport. The fit value for the dispersivity showed a nearly five fold increase from homogeneous matrix measurements, indicating that individual material measurements may not be adequate in describing a heterogeneous environment.

In Chapter 4 we analyzed the applicability of a DNS to represent a well characterized highly heterogeneous experimental system. Three experiments were run with differing flow rates. The DNS was constructed as accurately as possible, using measurements of the individual materials and their properties prior to and during construction of the experimental system. The results of the theoretical analysis were compared to the experimental mass recovery data collected at the outlet. Initial results showed better representation of Experiment #3 in comparison to the other two sets of data by the model. Slight adjustments to the dispersivity coefficient of the matrix and the diffusion coefficient for the inclusions improved the DNS representation, but was still lacking in its ability to represent the tailing shown for Experiment #1. Further validation of the model was performed through comparison of its results using the measured transport parameters for the system with the multirate spherical diffusion model. This comparison showed that the DNS did not adequately follow the same tailing trend as the multirate solution, indicating that the DNS results could not be relied upon for indicating how transport was occurring within this system. Further adjustments were necessary for this model in order to ensure its applicability for this type of highly heterogeneous porous system.

Through the three studies described above, it is obvious that a thorough knowledge of the experimental design is important when choosing the appropriate modeling technique to use. If the system is not well characterized and/or does not provide a complete set of data for comparison, the modeling software does not provide adequate numerical results. The numerical models need to be validated in order to ensure their results provide accurate information, and the mathematical assumptions need to be accurate, otherwise they will not provide accurate parameters to describe the processes affecting transport. Ultimately, it is important for one to attempt to understand the system being studied as thoroughly as possible and collect as much information as necessary to provide an adequate picture of all of the processes affecting solute transport within heterogeneous environments.

Heterogeneities affect solute transport in many ways; extending the time for mass recovery through non-Fickian tailing and creating multiple reaction rates that cannot be described using

the conventional ADE. When incomplete mass recovery data is available, the results of model simulations cannot be relied upon to provide accurate parameter estimations for the system. Even when complete information is known, the small-scale perturbations may have a larger effect on the overall mass transport than one would assume.

Upscaled solute transport models are powerful tools, providing quicker representations of transport behavior in complex systems. It is important to be positive that the ingrained assumptions are accurate for the system being studied, otherwise the results may provide an inadequate representation of what is really occurring. Direct numerical simulations are a also complicated and time consuming numerical methods. They require a large amount of information to construct an adequate representation of the system, and a large amount of computing power to run. When their solutions are validated, they are capable of providing a more detailed representation of what is occurring and, along with detailed mathematical analysis, can provide a more accurate picture of the effects of heterogeneities on the overall solute transport process. Without accurate validation, the DNS will not produce adequate results.

Ultimately, it is important to gather as much information about the system as possible and collect as much data as is necessary to completely describe experiments from beginning to end. Analyses can then be made to ensure the correct assumptions are made, the correct modeling approach is being used, and the most accurate results are gathered to thoroughly describe the overall solute transport through the system.

# Bibliography

[1] E. E. Adams and L. W. Gelhar. Field-study of dispersion in a heterogeneous aquifer .2. Spatial moments analysis. *Water Resour. Res.*, 28(12):3293–3307, 1992. doi:10.1029/92WR0175.

[2] M. O. Barnett, P. M. Jardine, S. C. Brooks, and H. M. Selim. Adsorption and transport of uranium(VI) in subsurface media. *Soil Sci. Soc. Am. J.*, 64(3):908–917, 2000.

[3] G. R. Barth, M. C. Hill, T. H. Illangasekare, and H. Rajaram. Predictive modeling of flow and transport in a two-dimensional intermediate-scale, heterogeneous porous medium. *Water Resour. Res.*, 37(10):2503–2512, October 2001.

[4] D. A. Benson, S. W. Wheatcraft, and M. M. Meerschaert. Application of a fractional advection-dispersion equation. *Water Resour. Res.*, 36(6):1403–1412, 2000. doi:10.1029/2000WR900031.

[5] B. Berkowitz, J. Klafter, R. Metzler, and H. Scher. Physical pictures of transport in heterogeneous media: Advection-dispersion, random-walk, and fractional derivative formulations. *Water Resour. Res.*, 38(10):1191 9–1–9–12, 2002. doi:10.1029/2001WR001030.

[6] B. Berkowitz, H. Scher, and S. E. Silliman. Anomalous transport in laboratory-scale, heterogeneous porous media. *Water Resour. Res.*, 36(1):149–158, 2000. doi:10.1029/1999WR900295.

[7] B. C. Bostick, S. Fendorf, M. O. Barnett, P. M. Jardine, and S. C. Brooks. Uranyl surface complexes formed on subsurface media from DOE facilities. *Soil Sci. Soc. Am. J.*, 66(1):99–108, 2002.

[8] C. J. Brown, J. D. Coates, and M. A. A. Schoonen. Localized sulfate-reducing zones in a coastal plain aquifer. *Ground Water*, 37(4):505–516, 1999. doi:10.1111/j.1745-6584.1999.tb01136.x.

[9] D. Brugge, J. L. de Lemos, and B. Oldmixon. Exposure pathways and health effects associated with chemical and radiological toxicity of natural uranium: A review. *Rev. Environ. Health*, 20(3):177–93, 2005.

[10] J. Chastanet and B. D. Wood. Mass transfer process in a two-region medium. *Water Resour. Res.*, 44(5):W05413 1–16, 2008. doi:10.1029/2006WR005553.

[11] F. Cherblanc, A. Ahmadi, and M. Quintard. Two-medium description of dispersion in heterogeneous porous media: Calculation of macroscopic properties. *Water Resour. Res.*, 39(6):SBH 6–1–6–20, 2003. doi:10.1029/2002WR001559.

[12] F. Cherblanc, A. Ahmadi, and M. Quintard. Two-domain description of solute transport in heterogeneous porous media: Comparison between theoretical predictions and numerical experiments. *Adv. Water Resour.*, 30(5):1127–1143, 2007. doi:10.1016/j.advwatres.2006.10.004.

[13] Invitrogen Corporation. Fluorescein, oregon green, and rhodamine green dyes. http://www.invitrogen.com/site/us/en/home/References/Molecular-Probes-The-Handbook/Fluorophores-and-Their-Amine-Reactive-Derivatives/Fluorescein-Oregon-Green-and-Rhodamine-Green-Dyes.html, April 2010.

[14] J. H. Cushman and T. R. Ginn. Fractional advection-dispersion equation: A classical mass balance with convolution-Fickian flux. *Water Resour. Res.*, 36(12):3763–3766, 2000. doi:10.1029/2000WR900261.

[15] J-R. de Dreuzy, A. Beaudoin, and J. Erhel. Asymptotic dispersion in 2D heterogeneous porous media determined by parallel numerical simulations. *Water Resour. Res.*, 43:W10439, 2007. doi:10.1092/2006WR005394.

[16] F. Delay, P. Ackerer, and C. Danquigny. Simulating solute transport in porous or fractured formations using random walk particle tracking: A review. *Vadose Zone J.*, 4(2):360–379, 2005. doi:10.2136/vzj2004.0125.

[17] F. W. Deng and J. H. Cushman. Comparison of moments for classical-Fickian, quasi-Fickian, and convolution-Fickian dispersion of a conservative tracer. *Water Resour. Res.*, 31(4):1147–1149, 1995. doi:10.1029/94WR02853.

[18] W. M. Dong, W. P. Ball, C. X. Liu, Z. M. Wang, A. T. Stone, J. Bai, and J. M. Zachara. Influence of calcite and dissolved calcium on uranium(VI) sorption to a Hanford subsurface sediment. *Environ. Sci. Technol.*, 39(20):7949–7955, 2005.

[19] D. A. Dzombak and F. M. M. Morel. *Surface complexation modeling: Hydrous ferric oxide*. John Wiley and Sons, Inc., New York, NY, 1 edition, 1990.

[20] U. S. EPA. National priorities list (npl). www.epa.gov/superfund/sites/npl/, March 2010.

[21] A. Fiori, I. Jankovic, G. Dagan, and V. Cvetkovic. Ergodic transport through aquifers of non-Gaussian log conductivity distribution and occurrence of anomalous behavior. *Water Resour. Res.*, 43(9):W09407 1–13, 2007. doi:10.1029/2007WR005976.

[22] F. Golfier, M. Quintard, F. Cherblanc, B. A. Zinn, and B. D. Wood. Comparison of theory and experiment for solute transport in highly heterogeneous porous medium. *Adv. Water Resour.*, 30(11):2235–2261, 2007. doi:10.1016/j.advwatres.2007.05.004.

[23] V. M. Goloviznin, I. A. Korotkin, K. Pruess, V. N. Semenov, and O. S. Sorokovikova. Stochastic models of solute transport in highly heterogeneous geologic media. *Vadose Zone J.*, 7(4):1207–1217, November 2008. doi:10.2136/vzj2007.0150.

[24] D. Gorman-Lewis, P. C. Burns, and J. B. Fein. Review of uranyl mineral solubility measurements. *J. Chem. Thermodyn.*, 40(3):335–352, 2008.

[25] R. Haggerty, S. W. Fleming, L. C. Meigs, and S. A. McKenna. Tracer tests in a fractured dolomite 2. Analysis of mass transfer in single-well injection-withdrawal tests. *Water Resour. Res.*, 37(5):1129–1142, 2001.

[26] R. Haggerty and S. M. Gorelick. Multiple-rate mass-transfer for modeling diffusion and surface-reactions in media with pore-scale heterogeneity. *Water Resour. Res.*, 31(10):2383–2400, 1995.

[27] R. Haggerty and S. M. Gorelick. Modeling mass transfer processes in soil columns with pore-scale heterogeneity. *Soil Sci. Soc. Am. J.*, 62(1):62–74, 1998.

[28] R. Haggerty, C. F. Harvey, C. F. von Schwerin, and L. C. Meigs. What controls the apparent timescale of solute mass transfer in aquifers and soils? A comparison of experimental results. *Water Resour. Res.*, 40(1):1–13, 2004.

[29] R. Haggerty, S. A. McKenna, and L. C. Meigs. On the late-time behavior of tracer test breakthrough curves. *Water Resour. Res.*, 36(12):3467–3479, 2000.

[30] R. Haggerty and P. Reeves. *STAMMT-L user manual, ERMS no. 520308*. Sandia National Laboratories, 2002.

[31] R. P. Han, W. H. Zou, Y. Wang, and L. Zhu. Removal of uranium(VI) from aqueous solutions by manganese oxide coated zeolite: Discussion of adsorption isotherms and pH effect. *J. Environ. Radioact.*, 93(3):127–143, 2007.

[32] S. J. Harrington. U(vi) transport in subsurface materials: Is two-site, one-species modeling sufficient? M.S. Thesis, Oregon State University, Corvallis, OR, September 2004.

[33] C. F. Harvey and S. M. Gorelick. Rate-limited mass transfer or macrodispersion: Which dominates plume evolution at the macrodispersion experiment (MADE) site? *Water Resour. Res.*, 36(3):637–650, 2000. Paper no. 1999WR900247.

[34] H. Hoteit, R. Mose, A. Younes, F. Lehmann, and P. Ackerer. Three-dimensional modeling of mass transfer in porous media using the mixed hybrid finite elements and the random-walk methods. *Math. Geol.*, 34(4):435–456, May 2002.

[35] C. K. D. Hsi and D. Langmuir. Adsorption of uranyl onto ferric oxyhydroxides - Application of the surface complexation site-binding model. *Geochim. Cosmochim. Acta*, 49(9):1931–1941, 1985.

[36] O. Huseby, A. Haugan, J. Sagen, J. Muller, B. Bennett, S. Larter, E. S. Kikkinides, A. K. Stubos, F. Yousefian, J.-F. Thovert, and P. M. Adler. Transport of organic components from immobile and bypassed oil in porous media. *AICHE J.*, 49(5):1085–1094, May 2003.

[37] S. D. Kelly, K. M. Kemner, and S. C. Brooks. X-ray absorption spectroscopy identifies calcium-uranyl-carbonate complexes at environmental concentrations. *Geochim. Cosmochim. Acta*, 71(4):821–834, 2007.

[38] S. D. Kelly, M. G. Newville, L. Cheng, K. M. Kemner, S. R. Sutton, P. Fenter, N. C. Sturchio, and C. Spotl. Uranyl incorporation in natural calcite. *Environ. Sci. Technol.*, 37(7):1284–1287, 2003.

[39] M. Konz, P. Ackerer, E. Meier, P. Huggenberger, E. Zechner, and D. Gechter. On the measurement of solute concentrations in 2-D flow tank experiments. *Hydrol. Earth Syst. Sci.*, 12:727–738, 2008. www.hydrol-earth-syst-sci.net/12/727/2008/.

[40] L. Li, D. A. Barry, P. J. Culligan-Hensley, and K. Bajracharya. Mass transfer in soil with local stratification of hydraulic conductivity. *Water Resour. Res*, 30(11):2891–2900, November 1993.

[41] C. X. Liu, J. M. Zachara, N. P. Qafoku, and Z. M. Wang. Scale-dependent desorption of uranium from contaminated subsurface sediments. *Water Resour. Res.*, 44(8):1–13, 2008.

[42] J. Luo, M. Dentz, O. A. Cirpka, and P. K. Kitanidis. Breakthrough curve tailing in a dipole flow field. *Water Resour. Res.*, 43:W09403, 2007. doi:10.1029/2006WR005600.

[43] G. Margolin and B. Berkowitz. Application of continuous time random walks to transport in porous media. *J. Phys. Chem. B*, 104(16):3942–3947, 2000. doi:10.1021/jp993721x.

[44] S. A. McKenna, L. C. Meigs, and R. Haggerty. Tracer tests in fractured dolomite 3. Double-porosity, multiple-rate mass transfer processes in convergent flow tracer tests. *Water Resour. Res.*, 37(5):1143–1154, 2001.

[45] M. M. Meerschaert, D. A. Benson, and B. Baumer. Multidimensional advection and fractional dispersion. *Phys. Rev. E*, 59(5):5026–5028, 1999.

[46] L. N. Moyes, R. H. Parkman, J. M. Charnock, D. J. Vaughan, F. R. Livens, C. R. Hughes, and A. Braithwaite. Uranium uptake from aqueous solution by interaction with goethite, lepidocrocite, muscovite, and mackinawite: An X-ray absorption spectroscopy study. *Environ. Sci. Technol.*, 34(6):1062–1068, 2000.

[47] E. M. Murphy, J. A. Schramke, J. K. Fredrickson, H. W. Bledsoe, A. J. Francis, D. S. Sklarew, and J. C. Linehan. The influence of microbial activity and sedimentary organic-carbon on the isotope geochemistry of the Middendorf aquifer. *Water Resour. Res.*, 28(3):723–740, 1992. doi:10.1029/91WR0267.

[48] N. P. Qafoku, J. M. Zachara, C. X. Liu, P. L. Gassman, O. S. Qafoku, and S. C. Smith. Kinetic desorption and sorption of U(VI) during reactive transport in a contaminated Hanford sediment. *Environ. Sci. Technol.*, 39(9):3157–3165, 2005.

[49] M. Quintard, L. Bletzacker, D. Chenu, and S. Whitaker. Nonlinear, multicomponent, mass transport in porous media. *Chem. Eng. Sci.*, 61(8):2643–2669, 2006. doi:10.1016/j.ces.2005.11.034.

[50] M. Quintard, F. Cherblanc, and S. Whitaker. Dispersion in heterogeneous porous media: One-equation non-equilibrium model. *Transport Porous Med.*, 44(1):181–203, 2001. doi:10.1023/A:1010746011296.

[51] S. A. Rani, B. Pitts, and P. S. Stewart. Rapid diffusion of fluorescent tracers into *Staphylococcus epidermidis* biofilms visualized by time lapse microscopy. *Antimicrob. Agents Chemother.*, 49(2):728–732, Feb. 2005. doi:10.1128/AAC.49.2.728-732.2005.

[52] J. R. Saylor and K. R. Sreenivasan. Differential diffusion in low reynolds number water jets. *Physics of Fluids*, 10(5):1135–1146, 1998.

[53] S. E. Silliman and L. Zheng. Comparison of observations from a laboratory model with stochastic theory: Initial analysis of hydraulic and tracer experiments. *Transport Porous Med.*, 42(1–2):85–107, January 2001.

[54] E. R. Sylwester, E. A. Hudson, and P. G. Allen. The structure of uranium(VI) sorption complexes on silica, alumina, and montmorillonite. *Geochim. Cosmochim. Acta*, 64(14):2431–2438, 2000.

[55] V. C. Tidwell and J. L. Wilson. Upscaling experiments conducted on a block of volcanic tuff: Results for a bimodal permeability distribution. *Water Resour. Res.*, 35(11):3375–3387, 1999. doi:10.1029/1999WR900161.

[56] T. K. Tokunaga, J. M. Wan, J. Pena, S. R. Sutton, and M. Newville. Hexavalent uranium diffusion into soils from concentrated acidic and alkaline solutions. *Environ. Sci. Technol.*, 38(11):3056–3062, 2004.

[57] N. Toride, F. J. Leij, and M. Th. van Genuchten. *The CXTFIT code for estimating transport parameters from laboratory or field tracer experiments*. US Salinity Laboratory, USDA, ARS, 1999.

[58] W. Um, R. J. Serne, C. F. Brown, and G. V. Last. U(VI) adsorption on aquifer sediments at the Hanford Site. *J. Contam. Hydrol.*, 93(1-4):255–269, 2007.

[59] USEPA. Radionuclides in drinking water. www.epa.gov/safewater/radionuclides/index.html, September 2006.

[60] T. D. Waite, J. A. Davis, T. E. Payne, G. A. Waychunas, and N. Xu. Uranium(VI) adsorption to ferrihydrite - Application of a surface complexation model. *Geochim. Cosmochim. Acta*, 58(24):5465–5478, 1994.

[61] J. Wan, J. T. Larsen, T. K. Tokunaga, and Z. Zheng. pH neutralization and zonation in alkaline-saline tank waste plumes. *Environ. Sci. Technol.*, 38(5):1321–1329, 2004.

[62] J. Wan, T. K. Tokunaga, J. T. Larsen, and R. J. Serne. Geochemical evolution of highly alkaline and saline tank waste plumes during seepage through vadose zone sediments. *Geochim. Cosmochim. Acta*, 68(3):491–502, 2004.

[63] Z. M. Wang, J. M. Zachara, P. L. Gassman, C. X. Liu, O. Qafoku, W. Yantasee, and J. G. Catalan. Fluorescence spectroscopy of U(VI)-silicates and U(VI)-contaminated Hanford sediment. *Geochim. Cosmochim. Acta*, 69(6):1391–1403, 2005.

[64] Z. M. Wang, J. M. Zachara, J. P. McKinley, and S. C. Smith. Cryogenic laser induced U(VI) fluorescence studies of a U(VI) substituted natural calcite: Implications to U(VI) speciation in contaminated Hanford sediments. *Environ. Sci. Technol.*, 39(8):2651–2659, 2005.

[65] S. Whitaker. *The Method of Volume Averaging*, volume 13 of *Theory and Applications of Transport in Porous Media*. Kluwer Academic Publishers, 101 Philip Drive, Norwell, MA 02061, 1999. ISBN 0-7923-5486-9.

[66] B. D. Wood, F. Golfier, F. Cherblanc, M. Quintard, and S. Whitaker. Upscaling transport in two-region bimodal porous media: Comparison of theory and experiment. Austin, Texas, 2003a. Proceedings of the SIAM Conference of Mathematics and Computational Issues in the Geosciences (GS03), Society for Industrial and Applied Mathematics.

[67] S. B. Yabusaki, Y. L. Fang, and S. R. Waichler. Building conceptual models of field-scale uranium reactive transport in a dynamic vadose zone-aquifer-river system. *Water Resour. Res.*, 44(12):1–24, 2008.

[68] J. M. Zachara, J. Serne, M. Freshley, F. Mann, F. Anderson, M. Wood, T. Jones, and D. Myers. Geochemical processes controlling migration of tank wastes in Hanford's vadose zone. *Vadose Zone J.*, 6(4):985–1003, 2007.

[69] F. Zhang, G. T. Yeh, J. C. Parker, S. C. Brooks, M. N. Pace, Y. J. Kim, P. M. Jardine, and D. B. Watson. A reaction-based paradigm to model reactive chemical transport in groundwater with general kinetic and equilibrium reactions. *J. Contam. Hydrol.*, 92(1-2):10–32, 2007.

[70] Q. Zhang. The asymptotic scaling behavior of mixing induced by a random velocity-field. *Adv. Appl. Math.*, 16(1):23–58, 1995.

[71] Q. Zhang. Multi-length-scale theories for scale-up problem and renormalized perturbation expansion. *Adv. Water Resour.*, 20(5-6):317–333, 1997. doi:10.1016/S0309-1708(96)00048-6.

[72] B. Zinn and C. F. Harvey. When good statistical models of aquifer heterogeneity go bad: A comparison of flow, dispersion, and mass transfer in connected and multivariate Gaussian hydraulic conductivity fields. *Water Resour. Res.*, 39(3):SBH 4–1–4–18, 2003. doi:10.1029/2001WR001146.

[73] B. Zinn, L. C. Meigs, C. F. Harvey, R. Haggerty, W. J. Peplinski, and C. F. Von Schwerin. Experimental visualization of solute transport and mass transfer processes in two-dimensional conductivity fields with connected regions of high conductivity. *Environ. Sci. Technol.*, 38(14):3916–3926, 2004. doi:10.1021/es034958g.

# APPENDICES

# Appendix A – Appendix for Chapters 3 and 4

## A.1 Characterization of Inclusions

A total of 221 inclusions were formed by sintering fine sand into a spherical shape. This was performed with the use of a spherical carbon mold placed in a muffle furnace. Each inclusion was formed and measured individually. Of the 221 inclusions created, only 203 were used in the construction of the highly heterogeneous system. The inclusions are described in Table A.1. This information was used to thoroughly characterize the highly heterogeneous system. Each measurement is made in duplicate and averaged. The inclusions are placed in the experimental system, with their x, y, and z coordinates determined through the use of the following Matlab code:

```
% Random placement of inclusions in Experimental System
% System dimensions are Y = 100 cm x X = 50 cm x Z = 20 cm
% Inclusions are spherical with a diameter of 5 cm
% Disect system into 5 cm x 5 cm x 5 cm cubes and randomly place
% inclusions inside.
% Ensure no placement of inclusions within first 5 cm of inlet or outlet
% or in direct contact (no nearest neighbor).
clear;
format long;
P=0.6; % Assuming 14% coverage of internal area of system
H=20; % Height of experimental system; 100 cm split into twenty 5 cm
% lengths
L=12;  % Length of experimental system; 50 cm split into ten 5 cm lengths
% + two blanks on each side
D=6;  % Depth of experimental system; 20 cm split into four 5 cm lengths
% + two blanks on each side
s=zeros (20,6,12); % Sets up the 3D matrix with initial values of zero
% at each coordinate
r=rand (20,6,12); % Sets up a 3D matrix with random values placed in each
% coordinate of a value between zero and one
count=0; % Keeping track of the total number of inclusions within the
% system
```

```
a=0; % For nearest neighbor distinction
n=0;  % Keeping track of the total number of inclusions in the system
for i=2:1:H-1; % Height loop
    for j=2:1:D-1; % Depth loop
        for k=2:1:L-1; % Length loop
            a=s (i-1,j,k)+s (i+1,j,k)+s (i,j-1,k)+s (i,j+1,k)+s \
(i,j,k-1)+s (i,j,k+1);  %  Add values of nearest neighbor's cells
            if r (i,j,k) <= P
                if a < 1  % Want to ensure no inclusion at the
% nearest neighbors; Diagonals are ok.
                    s(i,j,k)=1;  % If no inclusion at nearest
% neighbors and random # is in range, place inclusion
                    n=count+1;  % Add 1 to count of inclusions
% in system
                 else
                    s (i,j,k)=0;  %  Otherwise do not place inclusion
                    n=count;  %  Leave count as it was
                end
            end
            count=n;
        end
    end
end
s
count
volume=(count*65.45)/100000
% Written by Stephanie Harrington
```

Here, the experimental system is broken down into x, y, and z coordinates of 50 cm x 100 cm x 20 cm, with the zero axis being at the bottom-left-rear corner; the x-axis is the length; the y-axis is the height; and the z-axis is the depth. Placement of the inclusions was done by hand using a removable grid within the experimental system.

Table A.1: Average values of measured physical parameters and placement coordinates for 203 inclusions placed within the experimental system

| Sphere # | Avg. K (cm/min) | Avg. porosity | Avg. $V_{solid}$ ($cm^3$) | Avg. $V_{fluid}$ ($cm^3$) | x (cm) | y (cm) | z (cm) |
|---|---|---|---|---|---|---|---|
| 1 | 0.0058 | 0.29 | 41.62 | 17.05 | 22.5 | 37.5 | 7.5 |
| 2 | 0.0106 | 0.32 | 40.97 | 19.28 | 32.5 | 67.5 | 17.5 |
| 3 | 0.0091 | 0.34 | 40.72 | 20.78 | 27.5 | 77.5 | 17.5 |
| 4 | 0.0087 | 0.31 | 42.60 | 18.86 | 12.5 | 12.5 | 7.5 |
| 5 | 0.0057 | 0.31 | 42.49 | 18.84 | 37.5 | 22.5 | 2.5 |
| 6 | 0.0058 | 0.31 | 42.57 | 19.48 | 42.5 | 62.5 | 7.5 |
| 7 | 0.0167 | 0.35 | 41.54 | 21.99 | 22.5 | 77.5 | 2.5 |
| 8 | 0.0068 | 0.33 | 41.13 | 19.80 | 37.5 | 92.5 | 2.5 |
| 9 | 0.0067 | 0.31 | 41.69 | 18.93 | 17.5 | 7.5 | 7.5 |
| 10 | 0.0055 | 0.31 | 40.90 | 18.46 | 37.5 | 37.5 | 17.5 |
| 11 | 0.0264 | 0.32 | 41.25 | 19.40 | 7.5 | 47.5 | 7.5 |
| 12 | 0.0083 | 0.32 | 41.49 | 19.28 | 32.5 | 92.5 | 17.5 |
| 13 | 0.0094 | 0.34 | 41.23 | 20.82 | 17.5 | 92.5 | 12.5 |
| 14 | 0.0068 | 0.29 | 41.92 | 16.91 | 42.5 | 72.5 | 7.5 |
| 15 | 0.0156 | 0.28 | 42.54 | 16.23 | 2.5 | 87.5 | 7.5 |
| 16 | 0.0058 | 0.28 | 41.04 | 16.11 | 22.5 | 27.5 | 12.5 |
| 17 | 0.0095 | 0.30 | 41.44 | 17.85 | 37.5 | 82.5 | 2.5 |
| 18 | 0.0044 | 0.28 | 41.23 | 16.20 | 17.5 | 52.5 | 12.5 |
| 19 | 0.0045 | 0.29 | 41.04 | 16.40 | 47.5 | 52.5 | 12.5 |
| 20 | 0.0065 | 0.23 | 40.97 | 12.06 | 12.5 | 42.5 | 2.5 |
| 21 | 0.0122 | 0.21 | 40.67 | 10.81 | 2.5 | 32.5 | 12.5 |
| 22 | 0.0055 | 0.30 | 41.61 | 17.68 | 22.5 | 72.5 | 7.5 |
| 23 | 0.0070 | 0.27 | 42.13 | 15.95 | 32.5 | 32.5 | 17.5 |
| 24 | 0.0020 | 0.22 | 41.03 | 11.38 | 22.5 | 87.5 | 12.5 |
| 25 | 0.0019 | 0.22 | 41.84 | 11.85 | 17.5 | 17.5 | 12.5 |
| 26 | 0.0067 | 0.28 | 40.87 | 15.55 | 32.5 | 82.5 | 17.5 |
| 27 | 0.0067 | 0.31 | 42.61 | 19.50 | 2.5 | 47.5 | 17.5 |
| 28 | 0.0100 | 0.26 | 41.28 | 14.42 | 2.5 | 57.5 | 17.5 |
| 29 | 0.0030 | 0.22 | 41.00 | 11.26 | 22.5 | 62.5 | 7.5 |
| 30 | 0.0099 | 0.28 | 41.97 | 16.32 | 2.5 | 77.5 | 7.5 |
| 31 | 0.0057 | 0.28 | 41.46 | 16.27 | 27.5 | 47.5 | 7.5 |
| 32 | 0.0194 | 0.30 | 40.79 | 17.52 | 12.5 | 32.5 | 2.5 |

Continued on next page...

Table A.1 – Measured inclusion parameters, continued

| Sphere # | Avg. K (cm/min) | Avg. porosity | Avg. $V_{solid}$ ($cm^3$) | Avg. $V_{fluid}$ ($cm^3$) | x (cm) | y (cm) | z (cm) |
|---|---|---|---|---|---|---|---|
| 33 | 0.0158 | 0.32 | 41.01 | 19.18 | 7.5 | 12.5 | 2.5 |
| 34 | 0.0130 | 0.29 | 42.25 | 17.29 | 47.5 | 22.5 | 2.5 |
| 36 | 0.0164 | 0.26 | 41.04 | 14.75 | 7.5 | 72.5 | 17.5 |
| 37 | 0.0041 | 0.21 | 40.75 | 10.85 | 12.5 | 87.5 | 12.5 |
| 38 | 0.0214 | 0.18 | 41.24 | 9.15 | 22.5 | 47.5 | 2.5 |
| 39 | 0.0044 | 0.27 | 40.92 | 15.29 | 2.5 | 27.5 | 17.5 |
| 40 | 0.0121 | 0.20 | 40.72 | 10.33 | 37.5 | 72.5 | 12.5 |
| 41 | 0.0119 | 0.35 | 40.95 | 21.70 | 2.5 | 67.5 | 7.5 |
| 42 | 0.0242 | 0.35 | 40.80 | 22.04 | 7.5 | 27.5 | 2.5 |
| 43 | 0.0110 | 0.34 | 40.97 | 20.89 | 17.5 | 32.5 | 7.5 |
| 44 | 0.0078 | 0.33 | 41.96 | 20.79 | 17.5 | 67.5 | 7.5 |
| 45 | 0.0189 | 0.36 | 40.65 | 22.99 | 2.5 | 27.5 | 7.5 |
| 46 | 0.0115 | 0.34 | 41.66 | 21.35 | 17.5 | 62.5 | 17.5 |
| 47 | 0.0101 | 0.34 | 40.83 | 21.13 | 22.5 | 92.5 | 7.5 |
| 48 | 0.0057 | 0.30 | 41.43 | 18.12 | 2.5 | 42.5 | 12.5 |
| 49 | 0.0068 | 0.31 | 41.05 | 18.31 | 2.5 | 12.5 | 12.5 |
| 50 | 0.0212 | 0.35 | 40.93 | 22.29 | 17.5 | 37.5 | 12.5 |
| 51 | 0.0144 | 0.36 | 40.98 | 23.26 | 42.5 | 7.5 | 17.5 |
| 52 | 0.0157 | 0.36 | 41.14 | 23.33 | 12.5 | 67.5 | 17.5 |
| 53 | 0.0097 | 0.32 | 41.19 | 19.69 | 12.5 | 22.5 | 2.5 |
| 54 | 0.0112 | 0.34 | 41.24 | 21.48 | 37.5 | 62.5 | 12.5 |
| 55 | 0.0087 | 0.33 | 40.87 | 20.12 | 2.5 | 22.5 | 2.5 |
| 56 | 0.0094 | 0.34 | 42.56 | 21.51 | 32.5 | 52.5 | 7.5 |
| 57 | 0.0088 | 0.28 | 41.47 | 16.32 | 22.5 | 57.5 | 2.5 |
| 58 | 0.0107 | 0.34 | 40.98 | 21.10 | 7.5 | 62.5 | 12.5 |
| 59 | 0.0075 | 0.33 | 41.22 | 20.00 | 17.5 | 87.5 | 7.5 |
| 60 | 0.0167 | 0.33 | 41.29 | 19.89 | 7.5 | 17.5 | 17.5 |
| 61 | 0.0159 | 0.35 | 41.77 | 22.10 | 7.5 | 32.5 | 17.5 |
| 62 | 0.0062 | 0.31 | 42.62 | 18.73 | 12.5 | 37.5 | 7.5 |
| 63 | 0.0064 | 0.31 | 41.42 | 18.81 | 27.5 | 82.5 | 7.5 |
| 64 | 0.0220 | 0.32 | 41.35 | 19.46 | 2.5 | 67.5 | 17.5 |
| 65 | 0.0098 | 0.33 | 41.45 | 20.37 | 27.5 | 17.5 | 17.5 |
| 66 | 0.0206 | 0.32 | 41.18 | 19.69 | 47.5 | 87.5 | 7.5 |

Continued on next page...

Table A.1 – Measured inclusion parameters, continued

| Sphere # | Avg. K (cm/min) | Avg. porosity | Avg. $V_{solid}$ ($cm^3$) | Avg. $V_{fluid}$ ($cm^3$) | x (cm) | y (cm) | z (cm) |
|---|---|---|---|---|---|---|---|
| 67 | 0.0091 | 0.34 | 40.85 | 21.16 | 27.5 | 57.5 | 17.5 |
| 68 | 0.0051 | 0.26 | 41.64 | 14.95 | 47.5 | 72.5 | 12.5 |
| 69 | 0.0133 | 0.33 | 41.23 | 20.41 | 47.5 | 82.5 | 12.5 |
| 70 | 0.0106 | 0.32 | 42.37 | 20.12 | 12.5 | 47.5 | 12.5 |
| 71 | 0.0087 | 0.33 | 40.64 | 20.18 | 37.5 | 12.5 | 12.5 |
| 72 | 0.0080 | 0.33 | 40.86 | 20.03 | 2.5 | 32.5 | 2.5 |
| 73 | 0.0103 | 0.30 | 41.83 | 17.96 | 17.5 | 52.5 | 2.5 |
| 74 | 0.0123 | 0.31 | 40.93 | 18.06 | 12.5 | 37.5 | 17.5 |
| 75 | 0.0087 | 0.32 | 41.32 | 19.86 | 7.5 | 82.5 | 17.5 |
| 76 | 0.0071 | 0.30 | 41.07 | 17.86 | 17.5 | 37.5 | 2.5 |
| 77 | 0.0116 | 0.33 | 41.05 | 20.50 | 42.5 | 42.5 | 7.5 |
| 78 | 0.0120 | 0.30 | 40.56 | 17.20 | 42.5 | 92.5 | 17.5 |
| 79 | 0.0092 | 0.28 | 42.19 | 16.57 | 27.5 | 72.5 | 12.5 |
| 80 | 0.0081 | 0.31 | 40.58 | 18.46 | 37.5 | 82.5 | 12.5 |
| 81 | 0.0101 | 0.30 | 40.65 | 17.35 | 42.5 | 82.5 | 7.5 |
| 82 | 0.0077 | 0.31 | 41.21 | 18.78 | 7.5 | 82.5 | 2.5 |
| 83 | 0.0116 | 0.32 | 40.99 | 19.37 | 17.5 | 12.5 | 2.5 |
| 84 | 0.0158 | 0.32 | 41.51 | 19.72 | 27.5 | 62.5 | 2.5 |
| 85 | 0.0247 | 0.32 | 41.40 | 19.16 | 12.5 | 27.5 | 17.5 |
| 86 | 0.0098 | 0.35 | 41.32 | 22.38 | 17.5 | 47.5 | 17.5 |
| 87 | 0.0091 | 0.33 | 40.78 | 20.26 | 17.5 | 82.5 | 12.5 |
| 88 | 0.0158 | 0.36 | 40.98 | 22.58 | 12.5 | 77.5 | 2.5 |
| 89 | 0.0185 | 0.35 | 40.80 | 21.90 | 32.5 | 22.5 | 7.5 |
| 90 | 0.0205 | 0.37 | 40.92 | 24.02 | 12.5 | 52.5 | 17.5 |
| 91 | 0.0092 | 0.32 | 41.17 | 19.24 | 7.5 | 57.5 | 2.5 |
| 92 | 0.0111 | 0.35 | 40.81 | 22.22 | 2.5 | 87.5 | 17.5 |
| 93 | 0.0103 | 0.33 | 41.21 | 20.23 | 12.5 | 62.5 | 2.5 |
| 94 | 0.0096 | 0.35 | 41.51 | 22.56 | 47.5 | 12.5 | 7.5 |
| 95 | 0.0229 | 0.32 | 41.74 | 19.92 | 37.5 | 32.5 | 12.5 |
| 96 | 0.0085 | 0.34 | 41.09 | 20.78 | 27.5 | 27.5 | 7.5 |
| 97 | 0.0148 | 0.34 | 41.02 | 20.83 | 27.5 | 92.5 | 12.5 |
| 98 | 0.0084 | 0.33 | 42.53 | 21.24 | 27.5 | 22.5 | 2.5 |
| 99 | 0.0107 | 0.32 | 40.96 | 19.60 | 2.5 | 72.5 | 12.5 |

Continued on next page...

Table A.1 – Measured inclusion parameters, continued

| Sphere # | Avg. K (cm/min) | Avg. porosity | Avg. $V_{solid}$ ($cm^3$) | Avg. $V_{fluid}$ ($cm^3$) | x (cm) | y (cm) | z (cm) |
|---|---|---|---|---|---|---|---|
| 100 | 0.0088 | 0.33 | 41.70 | 20.22 | 17.5 | 72.5 | 17.5 |
| 101 | 0.0204 | 0.37 | 41.63 | 24.50 | 32.5 | 27.5 | 12.5 |
| 102 | 0.0081 | 0.33 | 40.98 | 20.12 | 22.5 | 92.5 | 17.5 |
| 104 | 0.0172 | 0.38 | 40.28 | 24.26 | 17.5 | 22.5 | 17.5 |
| 105 | 0.0045 | 0.35 | 40.46 | 21.65 | 7.5 | 42.5 | 17.5 |
| 108 | 0.0038 | 0.31 | 40.68 | 18.65 | 22.5 | 12.5 | 12.5 |
| 109 | 0.0079 | 0.31 | 41.67 | 18.82 | 32.5 | 77.5 | 12.5 |
| 110 | 0.0165 | 0.37 | 40.58 | 23.91 | 32.5 | 87.5 | 7.5 |
| 111 | 0.0090 | 0.34 | 40.92 | 20.80 | 17.5 | 7.5 | 17.5 |
| 112 | 0.0192 | 0.37 | 40.69 | 23.82 | 37.5 | 77.5 | 7.5 |
| 113 | 0.0157 | 0.32 | 40.91 | 19.02 | 12.5 | 7.5 | 2.5 |
| 114 | 0.0061 | 0.30 | 40.82 | 17.77 | 27.5 | 7.5 | 7.5 |
| 115 | 0.0107 | 0.35 | 41.01 | 22.54 | 22.5 | 32.5 | 17.5 |
| 116 | 0.0147 | 0.33 | 40.93 | 20.50 | 7.5 | 37.5 | 2.5 |
| 117 | 0.0080 | 0.33 | 40.43 | 19.47 | 2.5 | 17.5 | 7.5 |
| 118 | 0.0029 | 0.30 | 40.86 | 17.81 | 7.5 | 92.5 | 17.5 |
| 119 | 0.0119 | 0.31 | 39.74 | 17.92 | 12.5 | 32.5 | 12.5 |
| 120 | 0.0057 | 0.35 | 40.57 | 21.39 | 37.5 | 32.5 | 2.5 |
| 121 | 0.0121 | 0.37 | 39.74 | 23.41 | 47.5 | 37.5 | 7.5 |
| 122 | 0.0116 | 0.37 | 40.79 | 23.58 | 27.5 | 7.5 | 17.5 |
| 123 | 0.0058 | 0.32 | 40.81 | 18.95 | 32.5 | 17.5 | 2.5 |
| 124 | 0.0064 | 0.30 | 40.16 | 16.80 | 12.5 | 57.5 | 7.5 |
| 125 | 0.0054 | 0.34 | 41.14 | 21.06 | 2.5 | 7.5 | 17.5 |
| 126 | 0.0041 | 0.28 | 40.39 | 15.56 | 12.5 | 77.5 | 17.5 |
| 128 | 0.0059 | 0.28 | 39.96 | 15.59 | 2.5 | 72.5 | 2.5 |
| 131 | 0.0062 | 0.35 | 40.08 | 21.25 | 42.5 | 42.5 | 17.5 |
| 133 | 0.0017 | 0.27 | 40.53 | 14.93 | 42.5 | 12.5 | 2.5 |
| 134 | 0.0044 | 0.32 | 40.27 | 19.00 | 17.5 | 47.5 | 7.5 |
| 135 | 0.0036 | 0.31 | 40.27 | 18.33 | 42.5 | 67.5 | 2.5 |
| 137 | 0.0068 | 0.33 | 40.92 | 19.97 | 2.5 | 37.5 | 7.5 |
| 138 | 0.0085 | 0.29 | 40.71 | 16.28 | 37.5 | 17.5 | 17.5 |
| 139 | 0.0110 | 0.31 | 41.06 | 18.67 | 32.5 | 7.5 | 12.5 |
| 140 | 0.0047 | 0.34 | 40.92 | 21.41 | 37.5 | 37.5 | 7.5 |

Continued on next page...

Table A.1 – Measured inclusion parameters, continued

| Sphere # | Avg. K (cm/min) | Avg. porosity | Avg. $V_{solid}$ ($cm^3$) | Avg. $V_{fluid}$ ($cm^3$) | x (cm) | y (cm) | z (cm) |
|---|---|---|---|---|---|---|---|
| 141 | 0.0252 | 0.36 | 40.28 | 22.23 | 32.5 | 62.5 | 7.5 |
| 142 | 0.0073 | 0.26 | 41.71 | 14.63 | 42.5 | 47.5 | 12.5 |
| 143 | 0.0042 | 0.30 | 41.16 | 17.82 | 12.5 | 7.5 | 12.5 |
| 144 | 0.0196 | 0.35 | 41.04 | 22.00 | 37.5 | 67.5 | 7.5 |
| 146 | 0.0100 | 0.32 | 40.88 | 19.01 | 42.5 | 22.5 | 7.5 |
| 147 | 0.0273 | 0.28 | 41.22 | 15.81 | 37.5 | 77.5 | 17.5 |
| 148 | 0.0035 | 0.33 | 40.82 | 20.45 | 2.5 | 62.5 | 2.5 |
| 149 | 0.0087 | 0.30 | 41.86 | 17.92 | 22.5 | 82.5 | 17.5 |
| 150 | 0.0029 | 0.35 | 40.73 | 21.67 | 37.5 | 7.5 | 7.5 |
| 151 | 0.0036 | 0.34 | 40.50 | 20.79 | 47.5 | 32.5 | 2.5 |
| 152 | 0.0018 | 0.27 | 40.90 | 15.33 | 32.5 | 37.5 | 2.5 |
| 154 | 0.0113 | 0.27 | 40.94 | 15.09 | 42.5 | 87.5 | 12.5 |
| 155 | 0.0130 | 0.32 | 41.90 | 19.93 | 2.5 | 47.5 | 2.5 |
| 156 | 0.0027 | 0.32 | 40.31 | 19.04 | 27.5 | 87.5 | 17.5 |
| 158 | 0.0042 | 0.33 | 40.78 | 20.42 | 27.5 | 47.5 | 17.5 |
| 159 | 0.0024 | 0.26 | 41.75 | 14.37 | 47.5 | 22.5 | 12.5 |
| 161 | 0.0068 | 0.33 | 41.00 | 20.27 | 22.5 | 52.5 | 7.5 |
| 162 | 0.0044 | 0.29 | 41.16 | 16.58 | 47.5 | 52.5 | 2.5 |
| 163 | 0.0111 | 0.34 | 41.04 | 21.26 | 47.5 | 82.5 | 2.5 |
| 164 | 0.0051 | 0.28 | 40.75 | 15.59 | 42.5 | 52.5 | 7.5 |
| 165 | 0.0019 | 0.27 | 40.30 | 14.69 | 2.5 | 82.5 | 12.5 |
| 166 | 0.0142 | 0.28 | 40.82 | 16.08 | 32.5 | 57.5 | 12.5 |
| 167 | 0.0042 | 0.34 | 41.61 | 21.16 | 32.5 | 47.5 | 2.5 |
| 169 | 0.0040 | 0.32 | 40.94 | 19.46 | 27.5 | 72.5 | 2.5 |
| 170 | 0.0029 | 0.28 | 41.00 | 16.03 | 7.5 | 52.5 | 12.5 |
| 171 | 0.0053 | 0.23 | 40.92 | 12.08 | 22.5 | 42.5 | 12.5 |
| 172 | 0.0047 | 0.33 | 41.86 | 20.37 | 37.5 | 22.5 | 12.5 |
| 173 | 0.0056 | 0.28 | 40.74 | 16.06 | 12.5 | 82.5 | 7.5 |
| 174 | 0.0044 | 0.33 | 41.07 | 20.14 | 2.5 | 57.5 | 7.5 |
| 175 | 0.0056 | 0.29 | 40.79 | 16.97 | 32.5 | 67.5 | 2.5 |
| 176 | 0.0047 | 0.34 | 40.80 | 21.40 | 27.5 | 17.5 | 7.5 |
| 177 | 0.0077 | 0.25 | 41.73 | 14.08 | 7.5 | 77.5 | 12.5 |
| 178 | 0.0157 | 0.31 | 40.66 | 17.95 | 22.5 | 67.5 | 17.5 |

Continued on next page...

Table A.1 – Measured inclusion parameters, continued

| Sphere # | Avg. K (cm/min) | Avg. porosity | Avg. $V_{solid}$ ($cm^3$) | Avg. $V_{fluid}$ ($cm^3$) | x (cm) | y (cm) | z (cm) |
|---|---|---|---|---|---|---|---|
| 179 | 0.0092 | 0.35 | 40.99 | 22.03 | 37.5 | 47.5 | 17.5 |
| 180 | 0.0100 | 0.34 | 40.44 | 20.81 | 42.5 | 57.5 | 12.5 |
| 181 | 0.0173 | 0.37 | 39.70 | 22.83 | 32.5 | 17.5 | 12.5 |
| 182 | 0.0020 | 0.26 | 40.43 | 14.10 | 47.5 | 77.5 | 17.5 |
| 184 | 0.0376 | 0.31 | 40.86 | 18.19 | 47.5 | 7.5 | 2.5 |
| 185 | 0.0120 | 0.26 | 41.63 | 14.84 | 27.5 | 22.5 | 12.5 |
| 186 | 0.0101 | 0.31 | 41.15 | 18.59 | 12.5 | 12.5 | 17.5 |
| 187 | 0.0039 | 0.29 | 41.12 | 16.72 | 37.5 | 52.5 | 2.5 |
| 188 | 0.0063 | 0.33 | 40.59 | 20.25 | 32.5 | 27.5 | 2.5 |
| 189 | 0.0378 | 0.30 | 41.02 | 17.77 | 47.5 | 92.5 | 2.5 |
| 190 | 0.0042 | 0.27 | 41.10 | 14.87 | 27.5 | 62.5 | 12.5 |
| 191 | 0.0086 | 0.33 | 41.84 | 21.07 | 47.5 | 47.5 | 7.5 |
| 193 | 0.0077 | 0.29 | 40.96 | 16.46 | 12.5 | 22.5 | 12.5 |
| 194 | 0.0065 | 0.32 | 40.93 | 19.20 | 42.5 | 72.5 | 17.5 |
| 195 | 0.0038 | 0.29 | 41.62 | 16.69 | 37.5 | 92.5 | 12.5 |
| 196 | 0.0168 | 0.34 | 40.94 | 21.27 | 32.5 | 77.5 | 2.5 |
| 197 | 0.0028 | 0.26 | 40.54 | 14.15 | 27.5 | 52.5 | 2.5 |
| 198 | 0.0216 | 0.36 | 40.25 | 22.77 | 42.5 | 27.5 | 2.5 |
| 199 | 0.0146 | 0.33 | 40.59 | 20.15 | 47.5 | 62.5 | 2.5 |
| 200 | 0.0446 | 0.29 | 40.61 | 16.75 | 42.5 | 17.5 | 12.5 |
| 201 | 0.0091 | 0.32 | 40.58 | 19.36 | 22.5 | 27.5 | 2.5 |
| 202 | 0.0139 | 0.31 | 40.88 | 17.97 | 42.5 | 87.5 | 2.5 |
| 203 | 0.0137 | 0.34 | 41.00 | 21.19 | 47.5 | 67.5 | 17.5 |
| 204 | 0.0290 | 0.32 | 40.59 | 19.10 | 47.5 | 37.5 | 17.5 |
| 205 | 0.0057 | 0.29 | 40.91 | 17.00 | 37.5 | 57.5 | 17.5 |
| 206 | 0.0121 | 0.31 | 41.82 | 18.70 | 37.5 | 27.5 | 17.5 |
| 207 | 0.0129 | 0.30 | 40.35 | 17.30 | 42.5 | 67.5 | 12.5 |
| 208 | 0.0209 | 0.23 | 41.37 | 12.16 | 42.5 | 82.5 | 17.5 |
| 209 | 0.0048 | 0.25 | 40.33 | 13.32 | 42.5 | 92.5 | 7.5 |
| 210 | 0.0110 | 0.33 | 40.79 | 20.35 | 47.5 | 7.5 | 12.5 |
| 211 | 0.0172 | 0.31 | 40.62 | 18.57 | 27.5 | 27.5 | 17.5 |
| 212 | 0.0124 | 0.35 | 40.71 | 21.73 | 42.5 | 57.5 | 2.5 |
| 213 | 0.0403 | 0.31 | 40.95 | 18.83 | 7.5 | 67.5 | 2.5 |

Continued on next page...

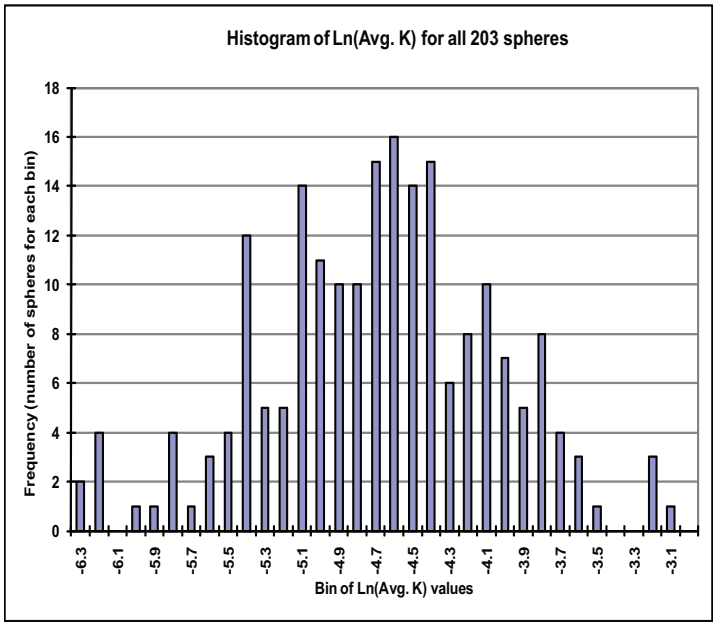


Figure A.1: Histogram of inclusions for 3D experimental system.

Table A.1 – Measured inclusion parameters, continued

| Sphere # | Avg. K (cm/min) | Avg. porosity | Avg. $V_{solid}$ ($cm^3$) | Avg. $V_{fluid}$ ($cm^3$) | x (cm) | y (cm) | z (cm) |
|---|---|---|---|---|---|---|---|
| 214 | 0.0231 | 0.32 | 40.37 | 18.82 | 47.5 | 72.5 | 2.5 |
| 215 | 0.0058 | 0.24 | 40.73 | 12.84 | 32.5 | 42.5 | 12.5 |
| 216 | 0.0070 | 0.30 | 41.72 | 17.99 | 42.5 | 52.5 | 17.5 |
| 218 | 0.0071 | 0.23 | 41.05 | 12.32 | 42.5 | 22.5 | 17.5 |
| 220 | 0.0144 | 0.33 | 40.43 | 19.96 | 47.5 | 17.5 | 17.5 |
| 221 | 0.0174 | 0.31 | 41.16 | 18.74 | 47.5 | 42.5 | 12.5 |

A histogram of the inclusions used for the experimental system is shown in Figure A.1. This shows the number of inclusions which fit into each grouping of log(Avg. K) values.

## A.2 Outlet BTC data

Table A.2: Average dimensionless concentration and time data for Experiment # 1 (Q = 5.62 ml/min; 1PV = 114.2 hr; Fluorescein Co = 1.5 mg/L; and Bromide Co = 30 mg/L)

| Time (PV) | Fluorescein C/Co | Time (PV) | Bromide C/Co |
|---|---|---|---|
| 0.0028 | 0.9527 | 0.0054 | 1.0650 |
| 0.0115 | 0.9540 | 0.0114 | 1.0259 |
| 0.0203 | 0.9587 | 0.1164 | 1.0231 |
| 0.0290 | 0.9607 | 0.2214 | 1.0794 |
| 0.0378 | 0.9647 | 0.3265 | 1.0660 |
| 0.0465 | 0.9680 | 0.4315 | 1.0487 |
| 0.0553 | 0.9707 | 0.5365 | 0.8918 |
| 0.0640 | 0.9707 | 0.6416 | 0.7306 |
| 0.0728 | 0.9720 | 0.7466 | 0.5662 |
| 0.0815 | 0.9740 | 0.8516 | 0.5353 |
| 0.0903 | 0.9780 | 0.9567 | 0.3955 |
| 0.0991 | 0.9833 | 1.0617 | 0.3537 |
| 0.1078 | 0.9800 | 1.1667 | 0.2476 |
| 0.1166 | 0.9860 | 1.2718 | 0.2473 |
| 0.1253 | 0.9893 | 1.3768 | 0.1576 |
| 0.1341 | 0.9947 | 1.4818 | 0.1541 |
| 0.1428 | 0.9913 | 1.5869 | 0.1159 |
| 0.1516 | 0.9873 | 1.6919 | 0.1009 |
| 0.1603 | 0.9953 | 1.7969 | 0.1147 |
| 0.1691 | 0.9933 | 1.9020 | 0.0920 |
| 0.1778 | 0.9860 | 2.0070 | 0.0959 |
| 0.1866 | 0.9787 | 2.1120 | 0.0744 |
| 0.1953 | 0.9733 | 2.2171 | 0.0689 |
| 0.2041 | 0.9693 | 2.3221 | 0.0593 |
| 0.2128 | 0.9667 | 2.4271 | 0.0556 |
| 0.2216 | 0.9707 | 2.5322 | 0.0565 |
| 0.2303 | 0.9620 | 2.6372 | 0.0465 |
| 0.2391 | 0.9767 | 2.7422 | 0.0459 |
| 0.2478 | 0.9600 | 2.8473 | 0.0532 |
| 0.2566 | 0.9747 | 2.9523 | 0.0424 |
| 0.2654 | 0.9813 | 3.0573 | 0.0365 |

Continued on next page...

Table A.2 – Dimensionless BTC data, Exp # 1, continued

| Time (PV) | Fluorescein C/Co | Time (PV) | Bromide C/Co |
|---|---|---|---|
| 0.2741 | 0.9747 | 3.1624 | 0.0304 |
| 0.2829 | 0.9860 | 3.2674 | 0.0287 |
| 0.2916 | 0.9980 | 3.3724 | 0.0269 |
| 0.3004 | 0.9833 | 3.4775 | 0.0225 |
| 0.3091 | 0.9820 | 3.5825 | 0.0228 |
| 0.3179 | 0.9787 | 3.6875 | 0.0176 |
| 0.3266 | 0.9813 | 3.7926 | 0.0203 |
| 0.3354 | 0.9773 | 3.8976 | 0.0155 |
| 0.3441 | 0.9773 | 4.0027 | 0.0162 |
| 0.3529 | 0.9700 | 4.1077 | 0.0129 |
| 0.3616 | 0.9667 | 4.2127 | 0.0139 |
| 0.3704 | 0.9660 | 4.3178 | 0.0094 |
| 0.3791 | 0.9593 | 4.4228 | 0.0090 |
| 0.3879 | 0.9580 | 4.5278 | 0.0105 |
| 0.3966 | 0.9633 | 4.6329 | 0.0097 |
| 0.4054 | 0.9567 | 4.7379 | 0.0086 |
| 0.4142 | 0.9507 | 4.8429 | 0.0067 |
| 0.4229 | 0.9493 | 4.9480 | 0.0016 |
| 0.4317 | 0.9440 | 5.0530 | 0.0058 |
| 0.4404 | 0.9313 | | |
| 0.4492 | 0.9233 | | |
| 0.4579 | 0.9120 | | |
| 0.4667 | 0.9000 | | |
| 0.4754 | 0.8907 | | |
| 0.4842 | 0.8813 | | |
| 0.4929 | 0.8807 | | |
| 0.5017 | 0.8693 | | |
| 0.5104 | 0.8613 | | |
| 0.5192 | 0.8480 | | |
| 0.5279 | 0.8367 | | |
| 0.5367 | 0.8247 | | |
| 0.5454 | 0.8060 | | |
| 0.5542 | 0.7800 | | |
| 0.5630 | 0.7473 | | |

Continued on next page...

Table A.2 – Dimensionless BTC data, Exp # 1, continued

| Time (PV) | Fluorescein C/Co | Time (PV) | Bromide C/Co |
|---|---|---|---|
| 0.5717 | 0.7120 | | |
| 0.5805 | 0.6800 | | |
| 0.5892 | 0.6767 | | |
| 0.5980 | 0.7000 | | |
| 0.6067 | 0.7053 | | |
| 0.6155 | 0.7140 | | |
| 0.6242 | 0.7153 | | |
| 0.6330 | 0.7080 | | |
| 0.6417 | 0.6867 | | |
| 0.6505 | 0.6627 | | |
| 0.6592 | 0.6407 | | |
| 0.6680 | 0.6273 | | |
| 0.6767 | 0.6060 | | |
| 0.6855 | 0.5913 | | |
| 0.6942 | 0.5733 | | |
| 0.7030 | 0.5607 | | |
| 0.7117 | 0.5493 | | |
| 0.7205 | 0.5407 | | |
| 0.7293 | 0.5360 | | |
| 0.7380 | 0.5267 | | |
| 0.7468 | 0.5200 | | |
| 0.7555 | 0.5093 | | |
| 0.7643 | 0.4933 | | |
| 0.7730 | 0.4780 | | |
| 0.7818 | 0.4627 | | |
| 0.7905 | 0.4567 | | |
| 0.7993 | 0.4627 | | |
| 0.8080 | 0.4713 | | |
| 0.8168 | 0.4840 | | |
| 0.8255 | 0.4980 | | |
| 0.8343 | 0.5067 | | |
| 0.8430 | 0.5100 | | |
| 0.8518 | 0.5133 | | |
| 0.8605 | 0.5147 | | |

Continued on next page...

Table A.2 – Dimensionless BTC data, Exp # 1, continued

| Time (PV) | Fluorescein C/Co | Time (PV) | Bromide C/Co |
|---|---|---|---|
| 0.8693 | 0.5033 | | |
| 0.8781 | 0.4820 | | |
| 0.8868 | 0.4633 | | |
| 0.8956 | 0.4447 | | |
| 0.9043 | 0.4327 | | |
| 0.9131 | 0.4233 | | |
| 0.9218 | 0.4133 | | |
| 0.9306 | 0.4020 | | |
| 0.9393 | 0.3953 | | |
| 0.9481 | 0.3867 | | |
| 0.9568 | 0.3793 | | |
| 0.9656 | 0.3707 | | |
| 0.9743 | 0.3607 | | |
| 0.9831 | 0.3520 | | |
| 0.9918 | 0.3407 | | |
| 1.0006 | 0.3313 | | |
| 1.0093 | 0.3333 | | |
| 1.0181 | 0.3473 | | |
| 1.0268 | 0.3540 | | |
| 1.0356 | 0.3580 | | |
| 1.0444 | 0.3573 | | |
| 1.0531 | 0.3507 | | |
| 1.0619 | 0.3400 | | |
| 1.0706 | 0.3253 | | |
| 1.0794 | 0.3133 | | |
| 1.0881 | 0.3013 | | |
| 1.0969 | 0.2927 | | |
| 1.1056 | 0.2853 | | |
| 1.1144 | 0.2760 | | |
| 1.1231 | 0.2660 | | |
| 1.1319 | 0.2593 | | |
| 1.1406 | 0.2527 | | |
| 1.1494 | 0.2507 | | |
| 1.1581 | 0.2467 | | |

Continued on next page...

Table A.2 – Dimensionless BTC data, Exp # 1, continued

| Time (PV) | Fluorescein C/Co | Time (PV) | Bromide C/Co |
|---|---|---|---|
| 1.1669 | 0.2387 | | |
| 1.1756 | 0.2320 | | |
| 1.1844 | 0.2287 | | |
| 1.1932 | 0.2280 | | |
| 1.2019 | 0.2260 | | |
| 1.2107 | 0.2280 | | |
| 1.2194 | 0.2420 | | |
| 1.2282 | 0.2527 | | |
| 1.2369 | 0.2580 | | |
| 1.2457 | 0.2627 | | |
| 1.2544 | 0.2600 | | |
| 1.2632 | 0.2540 | | |
| 1.2719 | 0.2467 | | |
| 1.2807 | 0.2353 | | |
| 1.2894 | 0.2140 | | |
| 1.2982 | 0.1920 | | |
| 1.3069 | 0.1760 | | |
| 1.3157 | 0.1700 | | |
| 1.3244 | 0.1640 | | |
| 1.3332 | 0.1627 | | |
| 1.3419 | 0.1627 | | |
| 1.3507 | 0.1613 | | |
| 1.3595 | 0.1607 | | |
| 1.3682 | 0.1613 | | |
| 1.3770 | 0.1593 | | |
| 1.3857 | 0.1580 | | |
| 1.3945 | 0.1513 | | |
| 1.4032 | 0.1447 | | |
| 1.4120 | 0.1420 | | |
| 1.4207 | 0.1400 | | |
| 1.4295 | 0.1387 | | |
| 1.4382 | 0.1420 | | |
| 1.4470 | 0.1480 | | |
| 1.4557 | 0.1573 | | |

Continued on next page...

Table A.2 – Dimensionless BTC data, Exp # 1, continued

| Time (PV) | Fluorescein C/Co | Time (PV) | Bromide C/Co |
|---|---|---|---|
| 1.4645 | 0.1573 | | |
| 1.4732 | 0.1580 | | |
| 1.4820 | 0.1567 | | |
| 1.4907 | 0.1493 | | |
| 1.4995 | 0.1360 | | |
| 1.5083 | 0.1213 | | |
| 1.5170 | 0.1127 | | |
| 1.5258 | 0.1107 | | |
| 1.5345 | 0.1087 | | |
| 1.5433 | 0.1100 | | |
| 1.5520 | 0.1127 | | |
| 1.5608 | 0.1140 | | |
| 1.5695 | 0.1160 | | |
| 1.5783 | 0.1173 | | |
| 1.5870 | 0.1207 | | |
| 1.5958 | 0.1207 | | |
| 1.6045 | 0.1187 | | |
| 1.6133 | 0.1160 | | |
| 1.6220 | 0.1140 | | |
| 1.6308 | 0.1133 | | |
| 1.6395 | 0.1127 | | |
| 1.6483 | 0.1087 | | |
| 1.6570 | 0.1100 | | |
| 1.6658 | 0.1133 | | |
| 1.6746 | 0.1167 | | |
| 1.6833 | 0.1153 | | |
| 1.6921 | 0.1113 | | |
| 1.7008 | 0.1060 | | |
| 1.7096 | 0.0993 | | |
| 1.7183 | 0.0953 | | |
| 1.7271 | 0.0967 | | |
| 1.7358 | 0.0993 | | |
| 1.7446 | 0.1027 | | |
| 1.7533 | 0.1053 | | |

Continued on next page...

Table A.2 – Dimensionless BTC data, Exp # 1, continued

| Time (PV) | Fluorescein C/Co | Time (PV) | Bromide C/Co |
|---|---|---|---|
| 1.7621 | 0.1073 | | |
| 1.7708 | 0.1093 | | |
| 1.7796 | 0.1120 | | |
| 1.7883 | 0.1133 | | |
| 1.7971 | 0.1147 | | |
| 1.8058 | 0.1180 | | |
| 1.8146 | 0.1227 | | |
| 1.8234 | 0.1240 | | |
| 1.8321 | 0.1207 | | |
| 1.8409 | 0.1127 | | |
| 1.8496 | 0.1060 | | |
| 1.8584 | 0.1013 | | |
| 1.8671 | 0.0993 | | |
| 1.8759 | 0.0980 | | |
| 1.8846 | 0.0967 | | |
| 1.8934 | 0.0967 | | |
| 1.9021 | 0.0967 | | |
| 1.9109 | 0.0980 | | |
| 1.9196 | 0.0993 | | |
| 1.9284 | 0.1007 | | |
| 1.9371 | 0.1027 | | |
| 1.9459 | 0.1040 | | |
| 1.9546 | 0.1040 | | |
| 1.9634 | 0.1027 | | |
| 1.9721 | 0.1007 | | |
| 1.9809 | 0.0987 | | |
| 1.9897 | 0.0973 | | |
| 1.9984 | 0.0967 | | |
| 2.0072 | 0.0960 | | |
| 2.0159 | 0.0960 | | |
| 2.0247 | 0.0953 | | |
| 2.0334 | 0.0953 | | |
| 2.0422 | 0.0953 | | |
| 2.0509 | 0.0933 | | |

Continued on next page...

Table A.2 – Dimensionless BTC data, Exp # 1, continued

| Time (PV) | Fluorescein C/Co | Time (PV) | Bromide C/Co |
|---|---|---|---|
| 2.0597 | 0.0913 | | |
| 2.0684 | 0.0893 | | |
| 2.0772 | 0.0880 | | |
| 2.0859 | 0.0860 | | |
| 2.0947 | 0.0840 | | |
| 2.1034 | 0.0820 | | |
| 2.1122 | 0.0813 | | |
| 2.1209 | 0.0813 | | |
| 2.1297 | 0.0807 | | |
| 2.1385 | 0.0793 | | |
| 2.1472 | 0.0787 | | |
| 2.1560 | 0.0787 | | |
| 2.1647 | 0.0800 | | |
| 2.1735 | 0.0813 | | |
| 2.1822 | 0.0833 | | |
| 2.1910 | 0.0833 | | |
| 2.1997 | 0.0793 | | |
| 2.2085 | 0.0767 | | |
| 2.2172 | 0.0753 | | |
| 2.2260 | 0.0747 | | |
| 2.2347 | 0.0733 | | |
| 2.2435 | 0.0707 | | |
| 2.2522 | 0.0680 | | |
| 2.2610 | 0.0673 | | |
| 2.2697 | 0.0673 | | |
| 2.2785 | 0.0680 | | |
| 2.2872 | 0.0687 | | |
| 2.2960 | 0.0693 | | |
| 2.3048 | 0.0693 | | |
| 2.3135 | 0.0693 | | |
| 2.3310 | 0.0707 | | |
| 2.3398 | 0.0700 | | |
| 2.3485 | 0.0693 | | |
| 2.3573 | 0.0687 | | |

Continued on next page...

Table A.2 – Dimensionless BTC data, Exp # 1, continued

| Time (PV) | Fluorescein C/Co | Time (PV) | Bromide C/Co |
|---|---|---|---|
| 2.3660 | 0.0680 | | |
| 2.3748 | 0.0680 | | |
| 2.3835 | 0.0680 | | |
| 2.3923 | 0.0673 | | |
| 2.4010 | 0.0667 | | |
| 2.4098 | 0.0667 | | |
| 2.4185 | 0.0660 | | |
| 2.4273 | 0.0667 | | |
| 2.4360 | 0.0667 | | |
| 2.4448 | 0.0660 | | |
| 2.4536 | 0.0653 | | |
| 2.4623 | 0.0647 | | |
| 2.4711 | 0.0647 | | |
| 2.4798 | 0.0640 | | |
| 2.4886 | 0.0640 | | |
| 2.4973 | 0.0667 | | |
| 2.5061 | 0.0700 | | |
| 2.5148 | 0.0720 | | |
| 2.5236 | 0.0713 | | |
| 2.5323 | 0.0693 | | |
| 2.5411 | 0.0680 | | |
| 2.5498 | 0.0660 | | |
| 2.5586 | 0.0627 | | |
| 2.5673 | 0.0593 | | |
| 2.5761 | 0.0573 | | |
| 2.5848 | 0.0567 | | |
| 2.5936 | 0.0567 | | |
| 2.6023 | 0.0573 | | |
| 2.6111 | 0.0560 | | |
| 2.6199 | 0.0533 | | |
| 2.6286 | 0.0540 | | |
| 2.6374 | 0.0553 | | |
| 2.6461 | 0.0560 | | |
| 2.6549 | 0.0567 | | |

Continued on next page...

Table A.2 – Dimensionless BTC data, Exp # 1, continued

| Time (PV) | Fluorescein C/Co | Time (PV) | Bromide C/Co |
|---|---|---|---|
| 2.6636 | 0.0567 | | |
| 2.6724 | 0.0567 | | |
| 2.6811 | 0.0573 | | |
| 2.6899 | 0.0567 | | |
| 2.6986 | 0.0567 | | |
| 2.7074 | 0.0567 | | |
| 2.7161 | 0.0573 | | |
| 2.7249 | 0.0560 | | |
| 2.7336 | 0.0553 | | |
| 2.7424 | 0.0547 | | |
| 2.7511 | 0.0540 | | |
| 2.7599 | 0.0547 | | |
| 2.7687 | 0.0547 | | |
| 2.7774 | 0.0567 | | |
| 2.7862 | 0.0587 | | |
| 2.7949 | 0.0600 | | |
| 2.8037 | 0.0607 | | |
| 2.8124 | 0.0620 | | |
| 2.8212 | 0.0627 | | |
| 2.8299 | 0.0633 | | |
| 2.8387 | 0.0620 | | |
| 2.8474 | 0.0613 | | |
| 2.8562 | 0.0593 | | |
| 2.8649 | 0.0593 | | |
| 2.8737 | 0.0593 | | |
| 2.8824 | 0.0587 | | |
| 2.8912 | 0.0573 | | |
| 2.8999 | 0.0553 | | |
| 2.9087 | 0.0533 | | |
| 2.9175 | 0.0507 | | |
| 2.9262 | 0.0493 | | |
| 2.9350 | 0.0480 | | |
| 2.9437 | 0.0467 | | |
| 2.9525 | 0.0467 | | |

Continued on next page...

Table A.2 – Dimensionless BTC data, Exp # 1, continued

| Time (PV) | Fluorescein C/Co | Time (PV) | Bromide C/Co |
|---|---|---|---|
| 2.9612 | 0.0460 | | |
| 2.9700 | 0.0453 | | |
| 2.9787 | 0.0447 | | |
| 2.9875 | 0.0440 | | |
| 2.9962 | 0.0447 | | |
| 3.0050 | 0.0447 | | |
| 3.0137 | 0.0453 | | |
| 3.0225 | 0.0447 | | |
| 3.0312 | 0.0440 | | |
| 3.0400 | 0.0427 | | |
| 3.0487 | 0.0420 | | |
| 3.0575 | 0.0413 | | |
| 3.0662 | 0.0407 | | |
| 3.0750 | 0.0407 | | |
| 3.0838 | 0.0393 | | |
| 3.0925 | 0.0380 | | |
| 3.1013 | 0.0373 | | |
| 3.1100 | 0.0373 | | |
| 3.1188 | 0.0367 | | |
| 3.1275 | 0.0367 | | |
| 3.1363 | 0.0367 | | |
| 3.1450 | 0.0367 | | |
| 3.1538 | 0.0367 | | |
| 3.1625 | 0.0360 | | |
| 3.1713 | 0.0353 | | |
| 3.1800 | 0.0353 | | |
| 3.1888 | 0.0347 | | |
| 3.1975 | 0.0340 | | |
| 3.2063 | 0.0340 | | |
| 3.2150 | 0.0340 | | |
| 3.2238 | 0.0333 | | |
| 3.2326 | 0.0333 | | |
| 3.2413 | 0.0333 | | |
| 3.2501 | 0.0333 | | |

Continued on next page...

Table A.2 – Dimensionless BTC data, Exp # 1, continued

| Time (PV) | Fluorescein C/Co | Time (PV) | Bromide C/Co |
|---|---|---|---|
| 3.2588 | 0.0333 | | |
| 3.2676 | 0.0333 | | |
| 3.2763 | 0.0320 | | |
| 3.2851 | 0.0313 | | |
| 3.2938 | 0.0313 | | |
| 3.3026 | 0.0313 | | |
| 3.3113 | 0.0307 | | |
| 3.3201 | 0.0307 | | |
| 3.3288 | 0.0300 | | |
| 3.3376 | 0.0300 | | |
| 3.3463 | 0.0300 | | |
| 3.3551 | 0.0300 | | |
| 3.3638 | 0.0307 | | |
| 3.3726 | 0.0307 | | |
| 3.3813 | 0.0307 | | |
| 3.3901 | 0.0313 | | |
| 3.3989 | 0.0313 | | |
| 3.4076 | 0.0313 | | |
| 3.4164 | 0.0307 | | |
| 3.4251 | 0.0307 | | |
| 3.4339 | 0.0300 | | |
| 3.4426 | 0.0300 | | |
| 3.4514 | 0.0293 | | |
| 3.4601 | 0.0293 | | |
| 3.4689 | 0.0280 | | |
| 3.4776 | 0.0273 | | |
| 3.4864 | 0.0260 | | |
| 3.4951 | 0.0253 | | |
| 3.5039 | 0.0253 | | |
| 3.5126 | 0.0253 | | |
| 3.5214 | 0.0253 | | |
| 3.5301 | 0.0253 | | |
| 3.5389 | 0.0260 | | |
| 3.5477 | 0.0267 | | |

Continued on next page...

Table A.2 – Dimensionless BTC data, Exp # 1, continued

| Time (PV) | Fluorescein C/Co | Time (PV) | Bromide C/Co |
|---|---|---|---|
| 3.5564 | 0.0273 | | |
| 3.5652 | 0.0280 | | |
| 3.5739 | 0.0287 | | |
| 3.5827 | 0.0287 | | |
| 3.5914 | 0.0287 | | |
| 3.6002 | 0.0280 | | |
| 3.6089 | 0.0273 | | |
| 3.6177 | 0.0267 | | |
| 3.6264 | 0.0253 | | |
| 3.6352 | 0.0253 | | |
| 3.6439 | 0.0253 | | |
| 3.6527 | 0.0253 | | |
| 3.6614 | 0.0247 | | |
| 3.6702 | 0.0240 | | |
| 3.6789 | 0.0227 | | |
| 3.6877 | 0.0220 | | |
| 3.6964 | 0.0213 | | |
| 3.7052 | 0.0207 | | |
| 3.7140 | 0.0207 | | |
| 3.7227 | 0.0213 | | |
| 3.7315 | 0.0213 | | |
| 3.7402 | 0.0213 | | |
| 3.7490 | 0.0227 | | |
| 3.7577 | 0.0233 | | |
| 3.7665 | 0.0240 | | |
| 3.7752 | 0.0253 | | |
| 3.7840 | 0.0260 | | |
| 3.7927 | 0.0267 | | |
| 3.8015 | 0.0267 | | |
| 3.8102 | 0.0253 | | |
| 3.8190 | 0.0247 | | |
| 3.8277 | 0.0233 | | |
| 3.8365 | 0.0233 | | |
| 3.8452 | 0.0227 | | |

Continued on next page...

Table A.2 – Dimensionless BTC data, Exp # 1, continued

| Time (PV) | Fluorescein C/Co | Time (PV) | Bromide C/Co |
|---|---|---|---|
| 3.8540 | 0.0227 | | |
| 3.8628 | 0.0227 | | |
| 3.8715 | 0.0220 | | |
| 3.8803 | 0.0213 | | |
| 3.8890 | 0.0207 | | |
| 3.8978 | 0.0200 | | |
| 3.9065 | 0.0193 | | |
| 3.9153 | 0.0193 | | |
| 3.9240 | 0.0187 | | |
| 3.9328 | 0.0187 | | |
| 3.9415 | 0.0187 | | |
| 3.9503 | 0.0187 | | |
| 3.9590 | 0.0193 | | |
| 3.9678 | 0.0207 | | |
| 3.9765 | 0.0213 | | |
| 3.9853 | 0.0220 | | |
| 3.9940 | 0.0220 | | |
| 4.0028 | 0.0213 | | |
| 4.0115 | 0.0213 | | |
| 4.0203 | 0.0213 | | |
| 4.0291 | 0.0200 | | |
| 4.0378 | 0.0193 | | |
| 4.0466 | 0.0187 | | |
| 4.0553 | 0.0187 | | |
| 4.0641 | 0.0180 | | |
| 4.0728 | 0.0180 | | |
| 4.0816 | 0.0180 | | |
| 4.0903 | 0.0180 | | |
| 4.0991 | 0.0173 | | |
| 4.1078 | 0.0160 | | |
| 4.1166 | 0.0153 | | |
| 4.1253 | 0.0153 | | |
| 4.1341 | 0.0153 | | |
| 4.1428 | 0.0153 | | |

Continued on next page...

Table A.2 – Dimensionless BTC data, Exp # 1, continued

| Time (PV) | Fluorescein C/Co | Time (PV) | Bromide C/Co |
|---|---|---|---|
| 4.1516 | 0.0153 | | |
| 4.1603 | 0.0160 | | |
| 4.1691 | 0.0167 | | |
| 4.1779 | 0.0173 | | |
| 4.1866 | 0.0173 | | |
| 4.1954 | 0.0180 | | |
| 4.2041 | 0.0180 | | |
| 4.2129 | 0.0173 | | |
| 4.2216 | 0.0173 | | |
| 4.2304 | 0.0167 | | |
| 4.2391 | 0.0160 | | |
| 4.2479 | 0.0153 | | |
| 4.2566 | 0.0147 | | |
| 4.2654 | 0.0147 | | |
| 4.2741 | 0.0147 | | |
| 4.2829 | 0.0140 | | |
| 4.2916 | 0.0140 | | |
| 4.3004 | 0.0133 | | |
| 4.3091 | 0.0127 | | |
| 4.3179 | 0.0127 | | |
| 4.3266 | 0.0127 | | |
| 4.3354 | 0.0127 | | |
| 4.3442 | 0.0120 | | |
| 4.3529 | 0.0120 | | |
| 4.3617 | 0.0113 | | |
| 4.3704 | 0.0113 | | |
| 4.3792 | 0.0113 | | |
| 4.3879 | 0.0113 | | |
| 4.3967 | 0.0113 | | |
| 4.4054 | 0.0113 | | |
| 4.4142 | 0.0107 | | |
| 4.4229 | 0.0107 | | |
| 4.4317 | 0.0107 | | |
| 4.4404 | 0.0100 | | |

Continued on next page...

Table A.2 – Dimensionless BTC data, Exp # 1, continued

| Time (PV) | Fluorescein C/Co | Time (PV) | Bromide C/Co |
|---|---|---|---|
| 4.4492 | 0.0107 | | |
| 4.4579 | 0.0107 | | |
| 4.4667 | 0.0107 | | |
| 4.4754 | 0.0113 | | |
| 4.4842 | 0.0113 | | |
| 4.4930 | 0.0120 | | |
| 4.5017 | 0.0127 | | |
| 4.5105 | 0.0133 | | |
| 4.5192 | 0.0140 | | |
| 4.5280 | 0.0147 | | |
| 4.5367 | 0.0153 | | |
| 4.5455 | 0.0160 | | |
| 4.5542 | 0.0160 | | |
| 4.5630 | 0.0160 | | |
| 4.5717 | 0.0160 | | |
| 4.5805 | 0.0153 | | |
| 4.5892 | 0.0147 | | |
| 4.5980 | 0.0140 | | |
| 4.6067 | 0.0133 | | |
| 4.6155 | 0.0127 | | |
| 4.6242 | 0.0127 | | |
| 4.6330 | 0.0120 | | |
| 4.6417 | 0.0120 | | |
| 4.6505 | 0.0113 | | |
| 4.6593 | 0.0113 | | |
| 4.6680 | 0.0113 | | |
| 4.6768 | 0.0113 | | |
| 4.6855 | 0.0113 | | |
| 4.6943 | 0.0113 | | |
| 4.7030 | 0.0113 | | |
| 4.7118 | 0.0113 | | |
| 4.7205 | 0.0113 | | |
| 4.7293 | 0.0113 | | |
| 4.7380 | 0.0107 | | |

Continued on next page...

Table A.2 – Dimensionless BTC data, Exp # 1, continued

| Time (PV) | Fluorescein C/Co | Time (PV) | Bromide C/Co |
|---|---|---|---|
| 4.7468 | 0.0107 | | |
| 4.7555 | 0.0100 | | |
| 4.7643 | 0.0100 | | |
| 4.7730 | 0.0073 | | |
| 4.7818 | 0.0093 | | |
| 4.7905 | 0.0093 | | |
| 4.7993 | 0.0093 | | |
| 4.8081 | 0.0093 | | |
| 4.8168 | 0.0093 | | |
| 4.8256 | 0.0093 | | |
| 4.8343 | 0.0093 | | |
| 4.8431 | 0.0093 | | |
| 4.8518 | 0.0087 | | |
| 4.8606 | 0.0087 | | |
| 4.8693 | 0.0087 | | |
| 4.8781 | 0.0087 | | |
| 4.8868 | 0.0087 | | |
| 4.8956 | 0.0087 | | |
| 4.9043 | 0.0080 | | |
| 4.9131 | 0.0080 | | |
| 4.9218 | 0.0073 | | |
| 4.9306 | 0.0073 | | |
| 4.9393 | 0.0067 | | |
| 4.9481 | 0.0067 | | |
| 4.9569 | 0.0067 | | |
| 4.9656 | 0.0060 | | |
| 4.9744 | 0.0060 | | |
| 4.9831 | 0.0067 | | |
| 4.9919 | 0.0067 | | |
| 5.0006 | 0.0067 | | |
| 5.0094 | 0.0067 | | |
| 5.0181 | 0.0067 | | |
| 5.0269 | 0.0073 | | |
| 5.0356 | 0.0073 | | |

Continued on next page...

Table A.2 – Dimensionless BTC data, Exp # 1, continued

| Time (PV) | Fluorescein C/Co | Time (PV) | Bromide C/Co |
|---|---|---|---|
| 5.0444 | 0.0073 | | |
| 5.0531 | 0.0073 | | |
| 5.0619 | 0.0073 | | |
| 5.0706 | 0.0073 | | |
| 5.0794 | 0.0067 | | |
| 5.0881 | 0.0067 | | |
| 5.0969 | 0.0067 | | |
| 5.1056 | 0.0060 | | |
| 5.1144 | 0.0060 | | |
| 5.1232 | 0.0060 | | |
| 5.1319 | 0.0060 | | |
| 5.1407 | 0.0060 | | |
| 5.1494 | 0.0060 | | |
| 5.1582 | 0.0053 | | |
| 5.1669 | 0.0053 | | |
| 5.1757 | 0.0053 | | |
| 5.1844 | 0.0053 | | |
| 5.1932 | 0.0053 | | |
| 5.2019 | 0.0053 | | |
| 5.2107 | 0.0053 | | |
| 5.2194 | 0.0053 | | |
| 5.2282 | 0.0053 | | |
| 5.2369 | 0.0060 | | |
| 5.2457 | 0.0060 | | |
| 5.2544 | 0.0060 | | |
| 5.2632 | 0.0060 | | |
| 5.2720 | 0.0060 | | |
| 5.2807 | 0.0060 | | |
| 5.2895 | 0.0060 | | |
| 5.2982 | 0.0060 | | |
| 5.3070 | 0.0060 | | |
| 5.3157 | 0.0060 | | |
| 5.3245 | 0.0060 | | |
| 5.3332 | 0.0060 | | |

Continued on next page...

Table A.2 – Dimensionless BTC data, Exp # 1, continued

| Time (PV) | Fluorescein C/Co | Time (PV) | Bromide C/Co |
|---|---|---|---|
| 5.3420 | 0.0053 | | |
| 5.3507 | 0.0053 | | |
| 5.3595 | 0.0053 | | |
| 5.3682 | 0.0053 | | |
| 5.3770 | 0.0053 | | |
| 5.3857 | 0.0053 | | |
| 5.3945 | 0.0053 | | |
| 5.4032 | 0.0053 | | |
| 5.4118 | 0.0053 | | |
| 5.4206 | 0.0053 | | |
| 5.4294 | 0.0053 | | |
| 5.4381 | 0.0053 | | |
| 5.4469 | 0.0053 | | |
| 5.4556 | 0.0053 | | |
| 5.4644 | 0.0053 | | |
| 5.4731 | 0.0053 | | |
| 5.4819 | 0.0053 | | |
| 5.4906 | 0.0047 | | |
| 5.4994 | 0.0047 | | |
| 5.5081 | 0.0047 | | |
| 5.5169 | 0.0047 | | |
| 5.5256 | 0.0047 | | |
| 5.5344 | 0.0047 | | |
| 5.5431 | 0.0047 | | |
| 5.5519 | 0.0047 | | |
| 5.5606 | 0.0047 | | |
| 5.5694 | 0.0047 | | |
| 5.5782 | 0.0047 | | |
| 5.5869 | 0.0047 | | |
| 5.5957 | 0.0053 | | |
| 5.6044 | 0.0047 | | |
| 5.6132 | 0.0047 | | |
| 5.6219 | 0.0047 | | |
| 5.6307 | 0.0047 | | |

Continued on next page...

Table A.2 – Dimensionless BTC data, Exp # 1, continued

| Time (PV) | Fluorescein C/Co | Time (PV) | Bromide C/Co |
|---|---|---|---|
| 5.6394 | 0.0047 | | |
| 5.6482 | 0.0047 | | |
| 5.6569 | 0.0047 | | |
| 5.6657 | 0.0047 | | |
| 5.6744 | 0.0047 | | |
| 5.6832 | 0.0047 | | |
| 5.6919 | 0.0047 | | |
| 5.7007 | 0.0047 | | |
| 5.7094 | 0.0040 | | |
| 5.7182 | 0.0040 | | |
| 5.7269 | 0.0040 | | |
| 5.7357 | 0.0040 | | |
| 5.7445 | 0.0040 | | |
| 5.7532 | 0.0033 | | |
| 5.7620 | 0.0033 | | |
| 5.7707 | 0.0033 | | |
| 5.7795 | 0.0033 | | |
| 5.7882 | 0.0033 | | |
| 5.7970 | 0.0033 | | |
| 5.8057 | 0.0027 | | |
| 5.8145 | 0.0027 | | |
| 5.8232 | 0.0027 | | |
| 5.8320 | 0.0027 | | |
| 5.8407 | 0.0027 | | |
| 5.8495 | 0.0027 | | |
| 5.8582 | 0.0033 | | |
| 5.8670 | 0.0033 | | |
| 5.8757 | 0.0033 | | |
| 5.8845 | 0.0033 | | |
| 5.8933 | 0.0033 | | |
| 5.9020 | 0.0033 | | |
| 5.9108 | 0.0033 | | |
| 5.9195 | 0.0027 | | |
| 5.9283 | 0.0027 | | |

Continued on next page...

Table A.2 – Dimensionless BTC data, Exp # 1, continued

| Time (PV) | Fluorescein C/Co | Time (PV) | Bromide C/Co |
|---|---|---|---|
| 5.9370 | 0.0027 | | |
| 5.9458 | 0.0027 | | |
| 5.9545 | 0.0027 | | |
| 5.9633 | 0.0027 | | |
| 5.9720 | 0.0020 | | |
| 5.9808 | 0.0020 | | |
| 5.9895 | 0.0020 | | |
| 5.9983 | 0.0020 | | |
| 6.0070 | 0.0020 | | |
| 6.0158 | 0.0020 | | |
| 6.0245 | 0.0020 | | |
| 6.0333 | 0.0020 | | |
| 6.0421 | 0.0020 | | |
| 6.0508 | 0.0020 | | |
| 6.0596 | 0.0020 | | |
| 6.0683 | 0.0027 | | |
| 6.0771 | 0.0027 | | |
| 6.0858 | 0.0027 | | |
| 6.0946 | 0.0027 | | |
| 6.1033 | 0.0027 | | |
| 6.1121 | 0.0027 | | |
| 6.1208 | 0.0027 | | |
| 6.1296 | 0.0027 | | |
| 6.1383 | 0.0027 | | |
| 6.1471 | 0.0027 | | |
| 6.1558 | 0.0027 | | |
| 6.1646 | 0.0020 | | |
| 6.1733 | 0.0020 | | |
| 6.1821 | 0.0020 | | |
| 6.1908 | 0.0020 | | |
| 6.1996 | 0.0020 | | |
| 6.2084 | 0.0020 | | |
| 6.2171 | 0.0020 | | |
| 6.2259 | 0.0020 | | |

Continued on next page...

Table A.2 – Dimensionless BTC data, Exp # 1, continued

| Time (PV) | Fluorescein C/Co | Time (PV) | Bromide C/Co |
|---|---|---|---|
| 6.2346 | 0.0020 | | |
| 6.2434 | 0.0013 | | |
| 6.2521 | 0.0013 | | |
| 6.2609 | 0.0013 | | |
| 6.2696 | 0.0020 | | |
| 6.2784 | 0.0020 | | |
| 6.2871 | 0.0020 | | |
| 6.2959 | 0.0020 | | |
| 6.3046 | 0.0020 | | |
| 6.3134 | 0.0020 | | |
| 6.3221 | 0.0020 | | |
| 6.3309 | 0.0020 | | |
| 6.3396 | 0.0020 | | |
| 6.3484 | 0.0020 | | |
| 6.3572 | 0.0020 | | |
| 6.3659 | 0.0020 | | |
| 6.3747 | 0.0020 | | |
| 6.3834 | 0.0020 | | |
| 6.3922 | 0.0020 | | |
| 6.4009 | 0.0020 | | |
| 6.4097 | 0.0020 | | |
| 6.4184 | 0.0013 | | |
| 6.4272 | 0.0013 | | |
| 6.4359 | 0.0013 | | |
| 6.4447 | 0.0013 | | |
| 6.4534 | 0.0013 | | |
| 6.4622 | 0.0013 | | |
| 6.4709 | 0.0013 | | |
| 6.4797 | 0.0013 | | |
| 6.4884 | 0.0020 | | |
| 6.4972 | 0.0020 | | |
| 6.5059 | 0.0020 | | |
| 6.5147 | 0.0020 | | |
| 6.5235 | 0.0020 | | |

Continued on next page...

Table A.2 – Dimensionless BTC data, Exp # 1, continued

| Time (PV) | Fluorescein C/Co | Time (PV) | Bromide C/Co |
|---|---|---|---|
| 6.5322 | 0.0020 | | |
| 6.5410 | 0.0020 | | |
| 6.5497 | 0.0020 | | |
| 6.5585 | 0.0020 | | |
| 6.5672 | 0.0020 | | |
| 6.5760 | 0.0013 | | |
| 6.5847 | 0.0013 | | |
| 6.5935 | 0.0013 | | |
| 6.6022 | 0.0013 | | |
| 6.6110 | 0.0013 | | |
| 6.6197 | 0.0013 | | |
| 6.6285 | 0.0013 | | |
| 6.6372 | 0.0013 | | |
| 6.6460 | 0.0013 | | |
| 6.6547 | 0.0013 | | |
| 6.6635 | 0.0013 | | |
| 6.6723 | 0.0013 | | |
| 6.6810 | 0.0013 | | |
| 6.6898 | 0.0013 | | |
| 6.6985 | 0.0013 | | |
| 6.7073 | 0.0013 | | |
| 6.7160 | 0.0013 | | |
| 6.7248 | 0.0013 | | |
| 6.7335 | 0.0013 | | |
| 6.7423 | 0.0013 | | |
| 6.7510 | 0.0013 | | |
| 6.7598 | 0.0013 | | |
| 6.7685 | 0.0013 | | |
| 6.7773 | 0.0013 | | |
| 6.7860 | 0.0013 | | |
| 6.7948 | 0.0013 | | |
| 6.8035 | 0.0013 | | |
| 6.8123 | 0.0013 | | |
| 6.8210 | 0.0013 | | |

Continued on next page...

Table A.2 – Dimensionless BTC data, Exp # 1, continued

| Time (PV) | Fluorescein C/Co | Time (PV) | Bromide C/Co |
|---|---|---|---|
| 6.8298 | 0.0013 | | |
| 6.8386 | 0.0007 | | |
| 6.8473 | 0.0007 | | |
| 6.8561 | 0.0007 | | |
| 6.8648 | 0.0007 | | |
| 6.8736 | 0.0007 | | |
| 6.8823 | 0.0007 | | |
| 6.8911 | 0.0007 | | |
| 6.8998 | 0.0007 | | |
| 6.9086 | 0.0013 | | |
| 6.9173 | 0.0013 | | |
| 6.9261 | 0.0013 | | |
| 6.9348 | 0.0013 | | |
| 6.9436 | 0.0013 | | |
| 6.9523 | 0.0013 | | |
| 6.9611 | 0.0013 | | |
| 6.9698 | 0.0013 | | |
| 6.9786 | 0.0013 | | |
| 6.9874 | 0.0007 | | |
| 6.9961 | 0.0007 | | |
| 7.0049 | 0.0007 | | |
| 7.0136 | 0.0007 | | |
| 7.0224 | 0.0007 | | |

Table A.3: Average dimensionless concentration and time data for Experiment # 2 (Q = 9.62 ml/min; 1PV = 66.73 hr; Fluorescein Co = 1.43 mg/L; and Bromide Co = 27 mg/L)

| Time (PV) | Fluorescein C/Co | Time (PV) | Bromide C/Co |
|---|---|---|---|
| 0.0150 | 0.9902 | 0.0056 | 0.9282 |
| 0.0300 | 0.9881 | 0.1707 | 0.9183 |
| 0.0450 | 0.9895 | 0.3118 | 0.9312 |
| 0.0599 | 0.9888 | 0.5117 | 0.9041 |
| 0.0749 | 0.9902 | 0.6673 | 0.8736 |
| 0.0899 | 0.9902 | 0.8418 | 0.2759 |
| 0.1049 | 0.9909 | 1.0292 | 0.2333 |

Continued on next page...

Table A.3 – Dimensionless BTC data, Exp # 2, continued

| Time (PV) | Fluorescein C/Co | Time (PV) | Bromide C/Co |
|---|---|---|---|
| 0.1199 | 0.9902 | 1.1873 | 0.1779 |
| 0.1349 | 0.9916 | 1.4160 | 0.0388 |
| 0.1499 | 0.9923 | 1.5632 | 0.0213 |
| 0.1648 | 0.9923 | 1.7984 | 0.0058 |
| 0.1798 | 0.9930 | 1.9403 | 0.0098 |
| 0.1948 | 0.9951 | 2.1299 | 0.0138 |
| 0.2098 | 0.9965 | 2.3157 | 0.0081 |
| 0.2248 | 0.9986 | 2.5120 | 0.0063 |
| 0.2398 | 0.9986 | 2.6354 | 0.0176 |
| 0.2548 | 0.9993 | 2.8339 | 0.0248 |
| 0.2697 | 0.9986 | 2.9856 | 0.0544 |
| 0.2847 | 0.9993 | 3.1944 | 0.0097 |
| 0.2997 | 1.0000 | 3.3724 | 0.0114 |
| 0.3147 | 0.9965 | 3.7094 | 0.0101 |
| 0.3297 | 0.9923 | 4.0828 | 0.0055 |
| 0.3447 | 0.9874 | 4.3962 | 0.0054 |
| 0.3597 | 0.9790 | | |
| 0.3746 | 0.9720 | | |
| 0.3896 | 0.9664 | | |
| 0.4046 | 0.9594 | | |
| 0.4196 | 0.9488 | | |
| 0.4346 | 0.9257 | | |
| 0.4496 | 0.8963 | | |
| 0.4646 | 0.8760 | | |
| 0.4795 | 0.8626 | | |
| 0.4945 | 0.8577 | | |
| 0.5095 | 0.8542 | | |
| 0.5245 | 0.8676 | | |
| 0.5395 | 0.8655 | | |
| 0.5545 | 0.8648 | | |
| 0.5695 | 0.8669 | | |
| 0.5844 | 0.8711 | | |
| 0.5994 | 0.8760 | | |
| 0.6144 | 0.8774 | | |

Continued on next page...

Table A.3 – Dimensionless BTC data, Exp # 2, continued

| Time (PV) | Fluorescein C/Co | Time (PV) | Bromide C/Co |
|---|---|---|---|
| 0.6294 | 0.8781 | | |
| 0.6444 | 0.8767 | | |
| 0.6594 | 0.8746 | | |
| 0.6744 | 0.8648 | | |
| 0.6893 | 0.8458 | | |
| 0.7043 | 0.8122 | | |
| 0.7193 | 0.7659 | | |
| 0.7343 | 0.7211 | | |
| 0.7493 | 0.6741 | | |
| 0.7643 | 0.6286 | | |
| 0.7793 | 0.5767 | | |
| 0.7942 | 0.5375 | | |
| 0.8092 | 0.5270 | | |
| 0.8242 | 0.5256 | | |
| 0.8392 | 0.5214 | | |
| 0.8542 | 0.5151 | | |
| 0.8692 | 0.5095 | | |
| 0.8842 | 0.5032 | | |
| 0.8991 | 0.5060 | | |
| 0.9141 | 0.5116 | | |
| 0.9291 | 0.5186 | | |
| 0.9441 | 0.5249 | | |
| 0.9591 | 0.5326 | | |
| 0.9741 | 0.5466 | | |
| 0.9891 | 0.5550 | | |
| 1.0040 | 0.5522 | | |
| 1.0190 | 0.5417 | | |
| 1.0340 | 0.5214 | | |
| 1.0490 | 0.4989 | | |
| 1.0640 | 0.4688 | | |
| 1.0790 | 0.4373 | | |
| 1.0940 | 0.4001 | | |
| 1.1090 | 0.3616 | | |
| 1.1239 | 0.3280 | | |

Continued on next page...

Table A.3 – Dimensionless BTC data, Exp # 2, continued

| Time (PV) | Fluorescein C/Co | Time (PV) | Bromide C/Co |
|---|---|---|---|
| 1.1389 | 0.2922 | | |
| 1.1539 | 0.2670 | | |
| 1.1689 | 0.2467 | | |
| 1.1839 | 0.2341 | | |
| 1.1989 | 0.2193 | | |
| 1.2139 | 0.2060 | | |
| 1.2288 | 0.1934 | | |
| 1.2438 | 0.1787 | | |
| 1.2588 | 0.1668 | | |
| 1.2738 | 0.1542 | | |
| 1.2888 | 0.1486 | | |
| 1.3038 | 0.1395 | | |
| 1.3188 | 0.1331 | | |
| 1.3337 | 0.1261 | | |
| 1.3487 | 0.1156 | | |
| 1.3637 | 0.1093 | | |
| 1.3787 | 0.1023 | | |
| 1.3937 | 0.0953 | | |
| 1.4087 | 0.0890 | | |
| 1.4237 | 0.0834 | | |
| 1.4386 | 0.0785 | | |
| 1.4536 | 0.0764 | | |
| 1.4686 | 0.0743 | | |
| 1.4836 | 0.0736 | | |
| 1.4986 | 0.0708 | | |
| 1.5136 | 0.0694 | | |
| 1.5286 | 0.0673 | | |
| 1.5435 | 0.0652 | | |
| 1.5585 | 0.0631 | | |
| 1.5735 | 0.0596 | | |
| 1.5885 | 0.0568 | | |
| 1.6035 | 0.0547 | | |
| 1.6185 | 0.0526 | | |
| 1.6335 | 0.0498 | | |

Continued on next page...

Table A.3 – Dimensionless BTC data, Exp # 2, continued

| Time (PV) | Fluorescein C/Co | Time (PV) | Bromide C/Co |
|---|---|---|---|
| 1.6484 | 0.0484 | | |
| 1.6634 | 0.0463 | | |
| 1.6784 | 0.0448 | | |
| 1.6934 | 0.0434 | | |
| 1.7084 | 0.0427 | | |
| 1.7234 | 0.0413 | | |
| 1.7384 | 0.0406 | | |
| 1.7533 | 0.0392 | | |
| 1.7683 | 0.0385 | | |
| 1.7833 | 0.0378 | | |
| 1.7983 | 0.0371 | | |
| 1.8133 | 0.0371 | | |
| 1.8283 | 0.0378 | | |
| 1.8433 | 0.0378 | | |
| 1.8582 | 0.0392 | | |
| 1.8732 | 0.0406 | | |
| 1.8882 | 0.0406 | | |
| 1.9032 | 0.0392 | | |
| 1.9182 | 0.0371 | | |
| 1.9332 | 0.0350 | | |
| 1.9482 | 0.0322 | | |
| 1.9631 | 0.0301 | | |
| 1.9781 | 0.0287 | | |
| 1.9931 | 0.0273 | | |
| 2.0081 | 0.0266 | | |
| 2.0231 | 0.0266 | | |
| 2.0381 | 0.0259 | | |
| 2.0531 | 0.0259 | | |
| 2.0680 | 0.0259 | | |
| 2.0830 | 0.0259 | | |
| 2.0980 | 0.0259 | | |
| 2.1130 | 0.0259 | | |
| 2.1280 | 0.0259 | | |
| 2.1430 | 0.0259 | | |

Continued on next page...

Table A.3 – Dimensionless BTC data, Exp # 2, continued

| Time (PV) | Fluorescein C/Co | Time (PV) | Bromide C/Co |
|---|---|---|---|
| 2.1580 | 0.0259 | | |
| 2.1729 | 0.0259 | | |
| 2.1879 | 0.0259 | | |
| 2.2029 | 0.0259 | | |
| 2.2179 | 0.0259 | | |
| 2.2329 | 0.0266 | | |
| 2.2479 | 0.0266 | | |
| 2.2629 | 0.0259 | | |
| 2.2778 | 0.0252 | | |
| 2.2928 | 0.0238 | | |
| 2.3078 | 0.0231 | | |
| 2.3228 | 0.0231 | | |
| 2.3378 | 0.0224 | | |
| 2.3528 | 0.0224 | | |
| 2.3678 | 0.0217 | | |
| 2.3827 | 0.0217 | | |
| 2.3977 | 0.0210 | | |
| 2.4127 | 0.0210 | | |
| 2.4277 | 0.0210 | | |
| 2.4427 | 0.0210 | | |
| 2.4577 | 0.0210 | | |
| 2.4727 | 0.0203 | | |
| 2.4876 | 0.0210 | | |
| 2.5026 | 0.0224 | | |
| 2.5176 | 0.0231 | | |
| 2.5326 | 0.0231 | | |
| 2.5476 | 0.0231 | | |
| 2.5626 | 0.0224 | | |
| 2.5776 | 0.0203 | | |
| 2.5925 | 0.0189 | | |
| 2.6075 | 0.0175 | | |
| 2.6225 | 0.0161 | | |
| 2.6375 | 0.0154 | | |
| 2.6525 | 0.0154 | | |

Continued on next page...

Table A.3 – Dimensionless BTC data, Exp # 2, continued

| Time (PV) | Fluorescein C/Co | Time (PV) | Bromide C/Co |
|---|---|---|---|
| 2.6675 | 0.0147 | | |
| 2.6825 | 0.0140 | | |
| 2.6974 | 0.0133 | | |
| 2.7124 | 0.0133 | | |
| 2.7274 | 0.0133 | | |
| 2.7424 | 0.0133 | | |
| 2.7574 | 0.0133 | | |
| 2.7724 | 0.0133 | | |
| 2.7874 | 0.0140 | | |
| 2.8023 | 0.0140 | | |
| 2.8173 | 0.0147 | | |
| 2.8323 | 0.0147 | | |
| 2.8473 | 0.0147 | | |
| 2.8623 | 0.0147 | | |
| 2.8773 | 0.0147 | | |
| 2.8923 | 0.0140 | | |
| 2.9072 | 0.0140 | | |
| 2.9222 | 0.0133 | | |
| 2.9372 | 0.0133 | | |
| 2.9522 | 0.0133 | | |
| 2.9672 | 0.0133 | | |
| 2.9822 | 0.0140 | | |
| 2.9972 | 0.0147 | | |
| 3.0121 | 0.0161 | | |
| 3.0271 | 0.0175 | | |
| 3.0421 | 0.0182 | | |
| 3.0571 | 0.0182 | | |
| 3.0721 | 0.0175 | | |
| 3.0871 | 0.0175 | | |
| 3.1021 | 0.0168 | | |
| 3.1170 | 0.0161 | | |
| 3.1320 | 0.0154 | | |
| 3.1470 | 0.0147 | | |
| 3.1620 | 0.0140 | | |

Continued on next page...

Table A.3 – Dimensionless BTC data, Exp # 2, continued

| Time (PV) | Fluorescein C/Co | Time (PV) | Bromide C/Co |
|---|---|---|---|
| 3.1770 | 0.0140 | | |
| 3.1920 | 0.0133 | | |
| 3.2070 | 0.0133 | | |
| 3.2219 | 0.0133 | | |
| 3.2369 | 0.0140 | | |
| 3.2519 | 0.0140 | | |
| 3.2669 | 0.0140 | | |
| 3.2819 | 0.0140 | | |
| 3.2969 | 0.0140 | | |
| 3.3119 | 0.0140 | | |
| 3.3269 | 0.0140 | | |
| 3.3418 | 0.0133 | | |
| 3.3568 | 0.0133 | | |
| 3.3718 | 0.0126 | | |
| 3.3868 | 0.0119 | | |
| 3.4018 | 0.0112 | | |
| 3.4168 | 0.0105 | | |
| 3.4318 | 0.0091 | | |
| 3.4467 | 0.0084 | | |
| 3.4617 | 0.0084 | | |
| 3.4767 | 0.0077 | | |
| 3.4917 | 0.0077 | | |
| 3.5067 | 0.0077 | | |
| 3.5217 | 0.0077 | | |
| 3.5367 | 0.0077 | | |
| 3.5516 | 0.0084 | | |
| 3.5666 | 0.0084 | | |
| 3.5816 | 0.0091 | | |
| 3.5966 | 0.0091 | | |
| 3.6116 | 0.0091 | | |
| 3.6266 | 0.0091 | | |
| 3.6416 | 0.0091 | | |
| 3.6565 | 0.0084 | | |
| 3.6715 | 0.0084 | | |

Continued on next page...

Table A.3 – Dimensionless BTC data, Exp # 2, continued

| Time (PV) | Fluorescein C/Co | Time (PV) | Bromide C/Co |
|---|---|---|---|
| 3.6865 | 0.0077 | | |
| 3.7015 | 0.0077 | | |
| 3.7165 | 0.0070 | | |
| 3.7315 | 0.0063 | | |
| 3.7465 | 0.0063 | | |
| 3.7614 | 0.0063 | | |
| 3.7764 | 0.0056 | | |
| 3.7914 | 0.0056 | | |
| 3.8064 | 0.0056 | | |
| 3.8214 | 0.0049 | | |
| 3.8364 | 0.0049 | | |
| 3.8514 | 0.0049 | | |
| 3.8663 | 0.0042 | | |
| 3.8813 | 0.0042 | | |
| 3.8963 | 0.0042 | | |
| 3.9113 | 0.0049 | | |
| 3.9263 | 0.0049 | | |
| 3.9413 | 0.0049 | | |
| 3.9563 | 0.0056 | | |
| 3.9712 | 0.0056 | | |
| 3.9862 | 0.0056 | | |
| 4.0012 | 0.0056 | | |
| 4.0162 | 0.0049 | | |
| 4.0312 | 0.0049 | | |
| 4.0462 | 0.0049 | | |
| 4.0612 | 0.0049 | | |
| 4.0761 | 0.0042 | | |
| 4.0911 | 0.0042 | | |
| 4.1061 | 0.0042 | | |
| 4.1211 | 0.0042 | | |
| 4.1361 | 0.0042 | | |
| 4.1511 | 0.0035 | | |
| 4.1661 | 0.0035 | | |
| 4.1810 | 0.0035 | | |

Continued on next page...

Table A.3 – Dimensionless BTC data, Exp # 2, continued

| Time (PV) | Fluorescein C/Co | Time (PV) | Bromide C/Co |
|---|---|---|---|
| 4.1960 | 0.0035 | | |
| 4.2110 | 0.0035 | | |
| 4.2260 | 0.0035 | | |
| 4.2410 | 0.0035 | | |
| 4.2560 | 0.0035 | | |
| 4.2710 | 0.0035 | | |
| 4.2859 | 0.0028 | | |
| 4.3009 | 0.0028 | | |
| 4.3159 | 0.0028 | | |
| 4.3309 | 0.0028 | | |
| 4.3459 | 0.0028 | | |
| 4.3609 | 0.0021 | | |
| 4.3759 | 0.0021 | | |
| 4.3908 | 0.0014 | | |
| 4.4058 | 0.0007 | | |

Table A.4: Average dimensionless concentration and time data for Experiment # 3 (Q = 45.2 ml/min; 1PV = 14.2 hr; Fluorescein Co = 1.52 mg/L; and Bromide Co = 30 mg/L)

| Time (PV) | Fluorescein C/Co | Time (PV) | Bromide C/Co |
|---|---|---|---|
| 0.0047 | 1.0000 | 0.0704 | 1.0273 |
| 0.0399 | 0.9987 | 0.1408 | 1.0350 |
| 0.0751 | 0.9974 | 0.2113 | 1.0274 |
| 0.1103 | 0.9980 | 0.2817 | 1.0156 |
| 0.1455 | 0.9915 | 0.3521 | 0.9866 |
| 0.1808 | 0.9855 | 0.4225 | 0.9717 |
| 0.2160 | 0.9822 | 0.4930 | 0.9277 |
| 0.2512 | 0.9763 | 0.5634 | 0.8683 |
| 0.2864 | 0.9619 | 0.6338 | 0.8147 |
| 0.3216 | 0.9520 | 0.7042 | 0.7631 |
| 0.3568 | 0.9336 | 0.7746 | 0.6802 |
| 0.3920 | 0.9224 | 0.8451 | 0.5924 |
| 0.4272 | 0.9073 | 0.9155 | 0.5078 |
| 0.4624 | 0.8882 | 0.9859 | 0.4360 |
| 0.4977 | 0.8672 | 1.0563 | 0.3605 |

Continued on next page...

Table A.4 – Dimensionless BTC data, Exp # 3, continued

| Time (PV) | Fluorescein C/Co | Time (PV) | Bromide C/Co |
|---|---|---|---|
| 0.5329 | 0.8481 | 1.1268 | 0.2776 |
| 0.5681 | 0.8304 | 1.1972 | 0.1937 |
| 0.6033 | 0.8107 | 1.2676 | 0.1395 |
| 0.6385 | 0.7909 | 1.3380 | 0.1108 |
| 0.6737 | 0.7673 | 1.4085 | 0.0784 |
| 0.7089 | 0.7370 | 1.4789 | 0.0556 |
| 0.7441 | 0.7028 | 1.5493 | 0.0437 |
| 0.7793 | 0.6634 | 1.6197 | 0.0343 |
| 0.8146 | 0.6206 | 1.6901 | 0.0309 |
| 0.8498 | 0.5799 | 1.7606 | 0.0266 |
| 0.8850 | 0.5391 | 1.8310 | 0.0243 |
| 0.9202 | 0.5023 | 1.9014 | 0.0226 |
| 0.9554 | 0.4668 | 1.9718 | 0.0209 |
| 0.9906 | 0.4313 | 2.0423 | 0.0186 |
| 1.0258 | 0.3912 | 2.1127 | 0.0171 |
| 1.0610 | 0.3550 | 2.1831 | 0.0165 |
| 1.0962 | 0.3130 | 2.2535 | 0.0156 |
| 1.1315 | 0.2650 | 2.3239 | 0.0145 |
| 1.1667 | 0.2150 | 2.3944 | 0.0140 |
| 1.2019 | 0.1723 | 2.4648 | 0.0135 |
| 1.2371 | 0.1387 | 2.5352 | 0.0128 |
| 1.2723 | 0.1170 | 2.6056 | 0.0128 |
| 1.3075 | 0.1032 | 2.6761 | 0.0127 |
| 1.3427 | 0.0888 | 2.7465 | 0.0107 |
| 1.3779 | 0.0730 | 2.8169 | 0.0104 |
| 1.4131 | 0.0579 | 2.8873 | 0.0083 |
| 1.4484 | 0.0467 | | |
| 1.4836 | 0.0388 | | |
| 1.5188 | 0.0335 | | |
| 1.5540 | 0.0296 | | |
| 1.5892 | 0.0270 | | |
| 1.6244 | 0.0250 | | |
| 1.6596 | 0.0230 | | |
| 1.6948 | 0.0217 | | |

Continued on next page...

Table A.4 – Dimensionless BTC data, Exp # 3, continued

| Time (PV) | Fluorescein C/Co | Time (PV) | Bromide C/Co |
|---|---|---|---|
| 1.7300 | 0.0210 | | |
| 1.7653 | 0.0204 | | |
| 1.8005 | 0.0197 | | |
| 1.8357 | 0.0191 | | |
| 1.8709 | 0.0184 | | |
| 1.9061 | 0.0184 | | |
| 1.9413 | 0.0178 | | |
| 1.9765 | 0.0171 | | |
| 2.0117 | 0.0164 | | |
| 2.0469 | 0.0164 | | |
| 2.0822 | 0.0158 | | |
| 2.1174 | 0.0151 | | |
| 2.1526 | 0.0151 | | |
| 2.1878 | 0.0145 | | |
| 2.2230 | 0.0145 | | |
| 2.2582 | 0.0138 | | |
| 2.2934 | 0.0138 | | |
| 2.3286 | 0.0138 | | |
| 2.3638 | 0.0138 | | |
| 2.3991 | 0.0138 | | |
| 2.4343 | 0.0131 | | |
| 2.4695 | 0.0131 | | |
| 2.5047 | 0.0131 | | |
| 2.5399 | 0.0131 | | |
| 2.5751 | 0.0131 | | |
| 2.6103 | 0.0131 | | |
| 2.6455 | 0.0131 | | |
| 2.6808 | 0.0131 | | |
| 2.7160 | 0.0131 | | |
| 2.7512 | 0.0131 | | |
| 2.7864 | 0.0125 | | |
| 2.8216 | 0.0118 | | |
| 2.8568 | 0.0112 | | |
| 2.8920 | 0.0105 | | |

Continued on next page...

Table A.4 – Dimensionless BTC data, Exp # 3, continued

| Time (PV) | Fluorescein C/Co | Time (PV) | Bromide C/Co |
|---|---|---|---|
| 2.9272 | 0.0099 | | |
| 2.9624 | 0.0092 | | |
| 2.9977 | 0.0092 | | |
| 3.0329 | 0.0085 | | |
| 3.0681 | 0.0085 | | |
| 3.1033 | 0.0079 | | |
| 3.1385 | 0.0079 | | |
| 3.1737 | 0.0079 | | |
| 3.2089 | 0.0079 | | |
| 3.2441 | 0.0079 | | |
| 3.2793 | 0.0079 | | |
| 3.3146 | 0.0079 | | |
| 3.3498 | 0.0079 | | |
| 3.3850 | 0.0085 | | |
| 3.4202 | 0.0085 | | |
| 3.4554 | 0.0085 | | |
| 3.4906 | 0.0092 | | |
| 3.5258 | 0.0092 | | |
| 3.5610 | 0.0092 | | |
| 3.5962 | 0.0092 | | |
| 3.6315 | 0.0092 | | |
| 3.6667 | 0.0092 | | |
| 3.7019 | 0.0092 | | |
| 3.7371 | 0.0085 | | |
| 3.7723 | 0.0085 | | |
| 3.8075 | 0.0085 | | |
| 3.8427 | 0.0079 | | |
| 3.8779 | 0.0079 | | |
| 3.9131 | 0.0072 | | |
| 3.9484 | 0.0072 | | |
| 3.9836 | 0.0072 | | |
| 4.0188 | 0.0072 | | |
| 4.0540 | 0.0066 | | |
| 4.0892 | 0.0066 | | |

Continued on next page...

Table A.4 – Dimensionless BTC data, Exp # 3, continued

| Time (PV) | Fluorescein C/Co | Time (PV) | Bromide C/Co |
|---|---|---|---|
| 4.1244 | 0.0066 | | |
| 4.1596 | 0.0066 | | |
| 4.1948 | 0.0066 | | |
| 4.2300 | 0.0066 | | |
| 4.2653 | 0.0066 | | |
| 4.3005 | 0.0066 | | |
| 4.3357 | 0.0066 | | |
| 4.3709 | 0.0066 | | |
| 4.4061 | 0.0066 | | |
| 4.4413 | 0.0066 | | |
| 4.4765 | 0.0066 | | |
| 4.5117 | 0.0066 | | |
| 4.5469 | 0.0059 | | |
| 4.5822 | 0.0059 | | |
| 4.6174 | 0.0059 | | |
| 4.6526 | 0.0059 | | |
| 4.6878 | 0.0053 | | |
| 4.7230 | 0.0053 | | |
| 4.7582 | 0.0053 | | |
| 4.7934 | 0.0053 | | |
| 4.8286 | 0.0046 | | |
| 4.8638 | 0.0046 | | |
| 4.8991 | 0.0053 | | |
| 4.9343 | 0.0046 | | |
| 4.9695 | 0.0046 | | |
| 5.0047 | 0.0046 | | |
| 5.0399 | 0.0046 | | |
| 5.0751 | 0.0046 | | |
| 5.1103 | 0.0053 | | |
| 5.1455 | 0.0053 | | |
| 5.1808 | 0.0053 | | |
| 5.2160 | 0.0053 | | |
| 5.2512 | 0.0053 | | |
| 5.2864 | 0.0053 | | |

Continued on next page...

Table A.4 – Dimensionless BTC data, Exp # 3, continued

| Time (PV) | Fluorescein C/Co | Time (PV) | Bromide C/Co |
|---|---|---|---|
| 5.3216 | 0.0053 | | |
| 5.3568 | 0.0053 | | |
| 5.3920 | 0.0046 | | |
| 5.4272 | 0.0046 | | |
| 5.4624 | 0.0046 | | |
| 5.4977 | 0.0046 | | |
| 5.5329 | 0.0046 | | |
| 5.5681 | 0.0046 | | |
| 5.6033 | 0.0046 | | |
| 5.6385 | 0.0039 | | |
| 5.6737 | 0.0039 | | |
| 5.7089 | 0.0039 | | |
| 5.7441 | 0.0039 | | |
| 5.7793 | 0.0039 | | |
| 5.8146 | 0.0039 | | |
| 5.8498 | 0.0039 | | |
| 5.8850 | 0.0039 | | |
| 5.9202 | 0.0039 | | |
| 5.9554 | 0.0039 | | |
| 5.9906 | 0.0039 | | |
| 6.0258 | 0.0039 | | |
| 6.0610 | 0.0039 | | |
| 6.0962 | 0.0039 | | |
| 6.1315 | 0.0039 | | |
| 6.1667 | 0.0039 | | |
| 6.2019 | 0.0039 | | |
| 6.2371 | 0.0039 | | |
| 6.2723 | 0.0039 | | |
| 6.3075 | 0.0039 | | |
| 6.3427 | 0.0039 | | |
| 6.3779 | 0.0039 | | |
| 6.4131 | 0.0039 | | |
| 6.4484 | 0.0033 | | |
| 6.4836 | 0.0033 | | |

Continued on next page...

Table A.4 – Dimensionless BTC data, Exp # 3, continued

| Time (PV) | Fluorescein C/Co | Time (PV) | Bromide C/Co |
|---|---|---|---|
| 6.5188 | 0.0033 | | |
| 6.5540 | 0.0033 | | |
| 6.5892 | 0.0033 | | |
| 6.6244 | 0.0033 | | |
| 6.6596 | 0.0033 | | |
| 6.6948 | 0.0033 | | |
| 6.7300 | 0.0033 | | |
| 6.7653 | 0.0033 | | |
| 6.8005 | 0.0033 | | |
| 6.8357 | 0.0026 | | |
| 6.8709 | 0.0033 | | |
| 6.9061 | 0.0026 | | |
| 6.9413 | 0.0026 | | |
| 6.9765 | 0.0026 | | |
| 7.0117 | 0.0033 | | |
| 7.0469 | 0.0026 | | |
| 7.0822 | 0.0033 | | |
| 7.1174 | 0.0026 | | |
| 7.1526 | 0.0026 | | |
| 7.1878 | 0.0026 | | |
| 7.2230 | 0.0026 | | |
| 7.2582 | 0.0026 | | |
| 7.2934 | 0.0026 | | |
| 7.3286 | 0.0026 | | |
| 7.3638 | 0.0026 | | |
| 7.3991 | 0.0026 | | |
| 7.4343 | 0.0026 | | |
| 7.4695 | 0.0026 | | |
| 7.5047 | 0.0026 | | |
| 7.5399 | 0.0026 | | |
| 7.5751 | 0.0026 | | |
| 7.6103 | 0.0026 | | |
| 7.6455 | 0.0026 | | |
| 7.6808 | 0.0026 | | |

Continued on next page...

Table A.4 – Dimensionless BTC data, Exp # 3, continued

| Time (PV) | Fluorescein C/Co | Time (PV) | Bromide C/Co |
|---|---|---|---|
| 7.7160 | 0.0026 | | |
| 7.7512 | 0.0026 | | |
| 7.7864 | 0.0026 | | |
| 7.8216 | 0.0026 | | |
| 7.8568 | 0.0020 | | |
| 7.8920 | 0.0026 | | |
| 7.9272 | 0.0020 | | |
| 7.9624 | 0.0020 | | |
| 7.9977 | 0.0020 | | |
| 8.0329 | 0.0020 | | |
| 8.0681 | 0.0020 | | |
| 8.1033 | 0.0020 | | |
| 8.1385 | 0.0020 | | |
| 8.1737 | 0.0020 | | |
| 8.2089 | 0.0020 | | |
| 8.2441 | 0.0020 | | |
| 8.2793 | 0.0020 | | |
| 8.3146 | 0.0020 | | |
| 8.3498 | 0.0020 | | |
| 8.3850 | 0.0020 | | |
| 8.4202 | 0.0020 | | |
| 8.4554 | 0.0020 | | |
| 8.4906 | 0.0020 | | |
| 8.5258 | 0.0020 | | |
| 8.5610 | 0.0020 | | |
| 8.5962 | 0.0020 | | |
| 8.6315 | 0.0020 | | |
| 8.6667 | 0.0020 | | |
| 8.7019 | 0.0020 | | |
| 8.7371 | 0.0020 | | |
| 8.7723 | 0.0020 | | |
| 8.8075 | 0.0020 | | |
| 8.8427 | 0.0020 | | |
| 8.8779 | 0.0020 | | |

Continued on next page...

Table A.4 – Dimensionless BTC data, Exp # 3, continued

| Time (PV) | Fluorescein C/Co | Time (PV) | Bromide C/Co |
|---|---|---|---|
| 8.9131 | 0.0020 | | |
| 8.9484 | 0.0020 | | |
| 8.9836 | 0.0020 | | |
| 9.0188 | 0.0020 | | |
| 9.0540 | 0.0020 | | |
| 9.0892 | 0.0020 | | |
| 9.1244 | 0.0020 | | |
| 9.1596 | 0.0013 | | |
| 9.1948 | 0.0013 | | |
| 9.2300 | 0.0013 | | |
| 9.2653 | 0.0013 | | |
| 9.3005 | 0.0013 | | |
| 9.3357 | 0.0013 | | |
| 9.3709 | 0.0013 | | |
| 9.4061 | 0.0013 | | |
| 9.4413 | 0.0013 | | |
| 9.4765 | 0.0013 | | |
| 9.5117 | 0.0013 | | |
| 9.5469 | 0.0013 | | |
| 9.5822 | 0.0013 | | |
| 9.6174 | 0.0013 | | |
| 9.6526 | 0.0013 | | |
| 9.6878 | 0.0013 | | |
| 9.7230 | 0.0013 | | |
| 9.7582 | 0.0013 | | |
| 9.7934 | 0.0013 | | |
| 9.8286 | 0.0013 | | |
| 9.8638 | 0.0013 | | |
| 9.8991 | 0.0013 | | |
| 9.9343 | 0.0013 | | |
| 9.9695 | 0.0013 | | |
| 10.0047 | 0.0013 | | |
| 10.0399 | 0.0013 | | |
| 10.0751 | 0.0013 | | |

Continued on next page...

Table A.4 – Dimensionless BTC data, Exp # 3, continued

| Time (PV) | Fluorescein C/Co | Time (PV) | Bromide C/Co |
|---|---|---|---|
| 10.1103 | 0.0013 | | |
| 10.1455 | 0.0013 | | |
| 10.1808 | 0.0013 | | |
| 10.2160 | 0.0013 | | |
| 10.2512 | 0.0013 | | |
| 10.2864 | 0.0013 | | |
| 10.3216 | 0.0013 | | |
| 10.3568 | 0.0013 | | |
| 10.3920 | 0.0013 | | |
| 10.4272 | 0.0013 | | |
| 10.4624 | 0.0013 | | |
| 10.4977 | 0.0013 | | |
| 10.5329 | 0.0013 | | |
| 10.5681 | 0.0013 | | |
| 10.6033 | 0.0013 | | |
| 10.6385 | 0.0013 | | |
| 10.6737 | 0.0013 | | |
| 10.7089 | 0.0013 | | |
| 10.7441 | 0.0013 | | |
| 10.7793 | 0.0007 | | |
| 10.8146 | 0.0007 | | |
| 10.8498 | 0.0007 | | |
| 10.8850 | 0.0007 | | |
| 10.9202 | 0.0007 | | |
| 10.9554 | 0.0007 | | |
| 10.9906 | 0.0007 | | |
| 11.0258 | 0.0007 | | |
| 11.0610 | 0.0013 | | |
| 11.0962 | 0.0007 | | |
| 11.1315 | 0.0007 | | |
| 11.1667 | 0.0013 | | |
| 11.2019 | 0.0013 | | |
| 11.2371 | 0.0013 | | |
| 11.2723 | 0.0013 | | |

Continued on next page...

Table A.4 – Dimensionless BTC data, Exp # 3, continued

| Time (PV) | Fluorescein C/Co | Time (PV) | Bromide C/Co |
|---|---|---|---|
| 11.3075 | 0.0013 | | |
| 11.3427 | 0.0013 | | |
| 11.3779 | 0.0013 | | |
| 11.4131 | 0.0013 | | |
| 11.4484 | 0.0013 | | |
| 11.4836 | 0.0013 | | |
| 11.5188 | 0.0013 | | |
| 11.5540 | 0.0013 | | |
| 11.5892 | 0.0007 | | |
| 11.6244 | 0.0007 | | |
| 11.6596 | 0.0007 | | |
| 11.6948 | 0.0007 | | |
| 11.7300 | 0.0013 | | |
| 11.7653 | 0.0013 | | |
| 11.8005 | 0.0013 | | |
| 11.8357 | 0.0013 | | |
| 11.8709 | 0.0007 | | |
| 11.9061 | 0.0007 | | |
| 11.9413 | 0.0007 | | |
| 11.9765 | 0.0007 | | |
| 12.0117 | 0.0007 | | |
| 12.0469 | 0.0007 | | |
| 12.0822 | 0.0007 | | |
| 12.1174 | 0.0007 | | |
| 12.1526 | 0.0007 | | |
| 12.1878 | 0.0007 | | |
| 12.2230 | 0.0007 | | |
| 12.2582 | 0.0007 | | |
| 12.2934 | 0.0007 | | |
| 12.3286 | 0.0007 | | |
| 12.3638 | 0.0007 | | |

## A.3 3D Data Sets For Experiments #1 and #2

Coordinates for internal ports in (x,y,z), where x is the width, y is height, and z is depth into system in cm are: A(25,85,7.78); B(5,55,7.94); C(25,55,7.62); D(45,55,7.94); E(25,15,7.3). Concentration measurements were taken for Experiments #1 and #2, but due to the fast flow rate no samples were taken from the internal ports for Experiment #3. Samples were measured for Bromide, since it took the least amount of volume for each measurement (0.5 mL per measurement).

Table A.5: Average dimensionless concentration and time data for Internal ports for Experiment # 1 (Q = 5.62 ml/min; 1PV = 114.2 hr; Fluorescein Co = 1.50 mg/L; and Bromide Co = 30 mg/L).

| Time (PV) | Bromide C/Co | Time (PV) | Bromide C/Co | Time (PV) | Bromide C/Co |
|---|---|---|---|---|---|
| Port A | | Port B | | Port C | |
| 0.0082 | 0.9618 | 0.0085 | 1.0260 | 0.0088 | 1.0769 |
| 0.3650 | 0.7704 | 0.3651 | 0.3199 | 0.3656 | 0.7751 |
| 0.5987 | 0.3720 | 0.5991 | 0.1620 | 0.5994 | 0.4469 |
| 0.8760 | 0.5929 | 0.8764 | 0.0789 | 0.8766 | 0.4657 |
| 1.0451 | 0.5165 | 1.0461 | 0.0490 | 1.0467 | 0.3591 |
| 1.2565 | 0.4773 | 1.2572 | 0.0493 | 1.2578 | 0.1291 |
| 1.4747 | 0.4688 | 1.4753 | 0.0470 | 1.4759 | 0.2469 |
| 1.6753 | 0.3588 | 1.6757 | 0.0548 | 1.6761 | 0.0739 |
| 2.0719 | 0.1375 | 2.0728 | 0.0341 | 2.0734 | 0.0541 |
| 2.2423 | 0.0972 | 2.2433 | 0.0362 | 2.2439 | 0.0558 |
| 2.5475 | 0.0876 | 2.5476 | 0.0296 | 2.5478 | 0.1032 |
| 2.7459 | 0.0525 | 2.7460 | 0.0287 | 2.7462 | 0.0849 |
| 2.9046 | 0.0501 | 2.9053 | 0.0216 | 2.9061 | 0.0332 |
| 3.1832 | 0.0452 | 3.1834 | 0.0206 | 3.1835 | 0.0216 |
| 3.5385 | 0.0298 | 3.5392 | 0.0229 | 3.5398 | 0.0177 |
| 3.7412 | 0.0302 | 3.7418 | 0.0188 | 3.7427 | 0.0094 |
| 4.0067 | 0.0179 | 4.0069 | 0.0121 | 4.0070 | 0.0127 |
| 4.1676 | 0.0151 | 4.1691 | 0.0076 | 4.1705 | 0.0075 |
| 4.3741 | 0.0202 | 4.3753 | 0.0142 | 4.3777 | 0.0117 |
| 4.5993 | 0.0139 | 4.5994 | 0.0063 | 4.5996 | 0.0075 |
| 4.8639 | 0.0093 | 4.8642 | 0.0000 | 4.8646 | 0.0063 |
| 5.0170 | 0.0067 | | | 5.0187 | 0.0033 |
| 5.2095 | 0.0000 | | | 5.2105 | 0.0000 |

Continued on next page...

Table A.5 – Dimensionless BTC data for internal ports, Exp # 1, continued

| Time (PV) | Bromide C/Co | Time (PV) | Bromide C/Co | Time (PV) | Bromide C/Co |
|---|---|---|---|---|---|
| 5.4126 | 0.0033 | | | | |
| 5.6413 | 0.0000 | | | | |
| | | | | | |
| Port D | | Port E | | | |
| 0.0090 | 1.0340 | 0.0093 | 1.0042 | | |
| 0.3657 | 1.0508 | 0.3660 | 0.4939 | | |
| 0.5996 | 1.0263 | 0.6001 | 0.2593 | | |
| 0.8766 | 0.2802 | 0.8769 | 0.0608 | | |
| 1.0478 | 0.0917 | 1.0481 | 0.0468 | | |
| 1.2581 | 0.0621 | 1.2588 | 0.0644 | | |
| 1.4764 | 0.0742 | 1.4773 | 0.0356 | | |
| 1.6766 | 0.0816 | 1.6770 | 0.0534 | | |
| 2.0740 | 0.0611 | 2.0745 | 0.0562 | | |
| 2.2445 | 0.0603 | 2.2451 | 0.0510 | | |
| 2.5479 | 0.0530 | 2.5481 | 0.0960 | | |
| 2.7463 | 0.0378 | 2.7466 | 0.0266 | | |
| 2.9068 | 0.0298 | 2.9077 | 0.0324 | | |
| 3.1837 | 0.0280 | 3.1838 | 0.0087 | | |
| 3.5403 | 0.0252 | 3.5409 | 0.0163 | | |
| 3.7431 | 0.0200 | 3.7438 | 0.0132 | | |
| 4.0071 | 0.0142 | 4.0073 | 0.0034 | | |
| 4.1720 | 0.0106 | 4.1735 | 0.0101 | | |
| 4.3788 | 0.0076 | 4.3797 | 0.0036 | | |
| 4.5997 | 0.0077 | 4.5999 | 0.0064 | | |
| 4.8649 | 0.0087 | 4.8654 | 0.0000 | | |
| 5.0195 | 0.0059 | 5.0207 | 0.0062 | | |
| 5.2111 | 0.0060 | 5.2118 | 0.0037 | | |
| 5.4144 | 0.0078 | 5.4152 | 0.0000 | | |
| 5.6435 | 0.0000 | | | | |

Table A.6: Average dimensionless concentration and time data for Internal ports for Experiment # 2 (Q = 9.62 ml/min; 1PV = 66.73 hr; Fluorescein Co = 1.43 mg/L; and Bromide Co = 27 mg/L).

| Time (PV) | Bromide C/Co | Time (PV) | Bromide C/Co | Time (PV) | Bromide C/Co |
|---|---|---|---|---|---|
| Port A | | Port B | | Port C | |
| 0.0056 | 0.9282 | 0.0064 | 0.9379 | 0.0071 | 0.9253 |
| 0.1707 | 0.9183 | 0.1715 | 0.9336 | 0.1722 | 0.9467 |
| 0.3118 | 0.9312 | 0.3146 | 0.8870 | 0.3176 | 0.9365 |
| 0.5117 | 0.9041 | 0.5127 | 0.0595 | 0.5132 | 0.9144 |
| 0.6673 | 0.8736 | 0.6683 | 0.0732 | 0.6690 | 0.5305 |
| 0.8418 | 0.2759 | 0.8428 | 0.0456 | 0.8436 | 0.2868 |
| 1.0292 | 0.2333 | 1.0299 | 0.0694 | 1.0309 | 0.1357 |
| 1.1873 | 0.1779 | 1.1888 | 0.0119 | 1.1895 | 0.0387 |
| 1.4160 | 0.0388 | 1.4168 | 0.0048 | 1.4178 | 0.0299 |
| 1.5632 | 0.0213 | 1.5644 | 0.0053 | 1.5652 | 0.0082 |
| 1.7984 | 0.0058 | 1.7994 | 0.0075 | 1.8002 | 0.0166 |
| 1.9403 | 0.0098 | 1.9415 | 0.0055 | 1.9425 | 0.0133 |
| 2.1299 | 0.0138 | 2.1309 | 0.0061 | 2.1321 | 0.0134 |
| 2.3157 | 0.0081 | 2.3164 | 0.0039 | 2.3174 | 0.0046 |
| 2.5120 | 0.0063 | 2.5130 | 0.0036 | 2.5145 | 0.0111 |
| 2.6354 | 0.0176 | 2.6364 | 0.0073 | 2.6371 | 0.0198 |
| 2.8339 | 0.0248 | 2.8347 | 0.0071 | 2.8354 | 0.0209 |
| 2.9856 | 0.0544 | | | 2.9876 | 0.0069 |
| 3.1944 | 0.0097 | | | 3.1966 | 0.0076 |
| 3.3724 | 0.0114 | | | 3.3739 | 0.0047 |
| 3.7094 | 0.0101 | | | 3.7131 | 0.0056 |
| 4.0828 | 0.0055 | | | | |
| 4.3962 | 0.0054 | | | | |
| | | | | | |
| Port D | | Port E | | | |
| 0.0079 | 0.9455 | 0.0086 | 0.9799 | | |
| 0.1730 | 0.9684 | 0.1737 | 0.2408 | | |
| 0.3206 | 0.9684 | 0.3236 | 0.0245 | | |
| 0.5137 | 0.7178 | 0.5142 | 0.2240 | | |
| 0.6700 | 0.3512 | 0.6710 | 0.0319 | | |
| 0.8446 | 0.1071 | 0.8456 | 0.2053 | | |

Continued on next page...

Table A.6 – Dimensionless BTC data for internal ports, Exp # 2, continued

| Time (PV) | Bromide C/Co | Time (PV) | Bromide C/Co | Time (PV) | Bromide C/Co |
|---|---|---|---|---|---|
| 1.0317 | 0.1073 | 1.0327 | 0.0199 | | |
| 1.1908 | 0.1231 | 1.1920 | 0.0089 | | |
| 1.4185 | 0.1062 | 1.4198 | 0.0044 | | |
| 1.5659 | 0.1045 | 1.5667 | 0.0286 | | |
| 1.8012 | 0.1033 | 1.8027 | 0.0048 | | |
| 1.9435 | 0.0639 | 1.9445 | 0.0000 | | |
| 2.1361 | 0.0818 | 2.1374 | 0.0000 | | |
| 2.3184 | 0.0814 | 2.3194 | 0.0129 | | |
| 2.5158 | 0.0708 | 2.5170 | 0.0143 | | |
| 2.6381 | 0.0506 | 2.6391 | 0.0123 | | |
| 2.8364 | 0.0078 | 2.8372 | 0.0000 | | |
| 2.9886 | 0.0051 | 2.9901 | 0.0086 | | |
| | | 3.1986 | 0.0052 | | |

## A.4 Flow Rate Measurements

Table A.7: Measured average flow rates for Experiments #1, #2, and #3. Flow rates were measured gravimetrically and averaged over 5 minutes.

| Experiment #1 | | Experiment #2 | | Experiment #3 | |
|---|---|---|---|---|---|
| Time (hr) | Flow Rate (g/min) | Time (hr) | Flow Rate (g/min) | Time (hr) | Flow Rate (g/min) |
| 0.60 | 5.50 | 0.00 | 9.83 | 0.05 | 32.62 |
| 1.47 | 4.00 | 11.62 | 7.92 | 0.50 | 52.80 |
| 17.85 | 4.99 | 20.78 | 9.23 | 1.00 | 49.13 |
| 40.85 | 4.75 | 22.90 | 9.90 | 2.00 | 49.20 |
| 66.50 | 5.17 | 28.25 | 10.11 | 4.00 | 49.32 |
| 99.05 | 5.37 | 34.12 | 9.38 | 6.00 | 49.84 |
| 113.12 | 5.34 | 44.28 | 9.12 | 10.00 | 44.22 |
| 135.97 | 6.05 | 48.87 | 9.19 | 22.00 | 44.04 |
| 161.45 | 5.66 | 56.12 | 8.90 | 23.00 | 45.02 |
| 186.30 | 6.06 | 69.12 | 8.63 | 25.50 | 44.60 |
| 235.00 | 5.43 | 79.12 | 8.53 | 28.50 | 45.54 |
| 255.17 | 5.38 | 94.37 | 8.40 | 30.00 | 45.98 |
| 290.18 | 5.00 | 104.25 | 9.18 | 45.17 | 44.48 |
| 312.70 | 5.14 | 119.50 | 9.14 | 48.17 | 44.80 |
| 330.73 | 5.52 | 140.40 | 9.09 | 49.50 | 44.76 |
| 362.82 | 4.78 | 153.00 | 8.91 | 53.50 | 45.32 |
| 401.33 | 5.56 | 165.47 | 9.62 | 69.15 | 44.18 |
| 425.42 | 5.59 | 165.97 | 9.61 | 73.15 | 44.78 |
| 449.47 | 5.74 | 178.38 | 10.03 | 74.65 | 44.74 |
| 474.13 | 5.00 | 187.30 | 9.90 | 95.15 | 44.32 |
| 497.73 | 5.14 | 199.52 | 9.88 | 103.65 | 44.48 |
| 523.60 | 4.90 | 209.15 | 9.89 | 122.65 | 43.86 |
| 553.82 | 4.88 | 221.08 | 9.73 | 142.65 | 44.08 |
| 570.85 | 5.91 | 233.00 | 10.46 | 166.15 | 44.24 |
| 593.00 | 5.84 | 254.28 | 10.38 | 189.65 | 43.92 |
| 616.30 | 5.34 | 279.28 | 10.38 | | |
| 638.40 | 5.83 | 300.23 | 10.65 | | |
| 665.03 | 5.94 | 316.50 | 9.96 | | |
| 690.80 | 5.94 | 327.05 | 10.10 | | |
| 716.85 | 5.30 | 346.83 | 10.34 | | |

Continued on next page...

Table A.7 – Average measured flow rates, continued

| Experiment #1 | | Experiment #2 | | Experiment #3 | |
|---|---|---|---|---|---|
| Time (hr) | Flow Rate (g/min) | Time (hr) | Flow Rate (g/min) | Time (hr) | Flow Rate (g/min) |
| 737.53 | 4.97 | 377.15 | 10.24 | | |
| 764.50 | 5.53 | 393.60 | 10.37 | | |
| 785.12 | 6.12 | 440.12 | 10.36 | | |
| 809.18 | 6.12 | | | | |